



Université de Caen
Basse-Normandie

GANIL R XX 16



UNIVERSITÉ DE CAEN BASSE NORMANDIE
U.F.R. de Sciences

Habilitation à Diriger des Recherches

Présentée par

M. François DE OLIVEIRA SANTOS

soutenue le

9 janvier 2017

Titre :

Contributions to Nuclear Astrophysics

MEMBRES du JURY :

| | | | |
|---------------------|------------------------|----------------------|---------------------|
| M. Bertram BLANK | Directeur de Recherche | CNRS | <i>(Rapporteur)</i> |
| M. Jürgen KIENER | Directeur de Recherche | CNRS | <i>(Rapporteur)</i> |
| M. Daniel BEMMERER | PD Dr. | HZDR | <i>(Rapporteur)</i> |
| Mme Emily LAMOUR | Professeure | UPMC | |
| M. Carlos BERTULANI | Professeur | Texas A&M University | |
| M. Marek LEWITOWICZ | Directeur de Recherche | CNRS | |

Contents

| | | |
|----------|--|-----------|
| 1 | Introduction | 1 |
| 1.1 | Introduction | 1 |
| 1.2 | My scientific path | 2 |
| 1.3 | The most Important Questions in Nuclear Astrophysics | 2 |
| 1.4 | Theoretical Predictions | 5 |
| 1.4.1 | The astrophysical factor | 5 |
| 1.4.2 | Nuclear statistical model | 7 |
| 1.4.3 | Predicting resonances properties | 9 |
| 1.4.4 | Direct-radiative-capture | 10 |
| 1.5 | Reaction rates | 10 |
| 1.6 | Experimental Techniques | 11 |
| 1.6.1 | Direct versus Indirect Measurements | 11 |
| 1.6.2 | Stable versus Radioactive Beams | 11 |
| 1.7 | Organisation of this document | 11 |
| 2 | Electron Screening Effect | 13 |
| 2.1 | Introduction: The electron-screening problem | 13 |
| 2.2 | β -decay in a superconductor (E578S) | 15 |
| 2.2.1 | Experiment at SPIRAL1 with Niobium | 16 |
| 2.2.2 | Analysis | 20 |
| 2.3 | Conclusion and Outlook | 22 |
| 2.3.1 | Summary | 22 |
| 2.3.2 | A new High-precision experiment (E558S) | 22 |
| 2.3.3 | Outlook | 23 |
| 3 | Origin of Fluorine | 25 |
| 3.1 | Introduction: The origin-of-fluorine problem | 25 |
| 3.2 | Determination of the $^{15}\text{N}(\alpha,\gamma)^{19}\text{F}$ reaction rate | 26 |
| 3.2.1 | The measurement of $^{15}\text{N}(^7\text{Li,t})^{19}\text{F}$ at Orsay | 26 |
| 3.2.2 | DWBA Analysis | 26 |
| 3.2.3 | Calculation of the direct-radiative-capture cross section | 31 |
| 3.2.4 | The new rate of $^{15}\text{N}(\alpha,\gamma)^{19}\text{F}$ | 32 |
| 3.2.5 | Astrophysical impact | 32 |
| 3.3 | Conclusion and Outlook | 33 |
| 4 | Nova γ-ray emission | 37 |
| 4.1 | Introduction: The ^{19}Ne -spins problem | 37 |
| 4.2 | The inelastic scattering reaction $^{19}\text{Ne}(p,p')^{19}\text{Ne}^*$ (PH221) | 41 |
| 4.2.1 | Experimental measurement | 42 |
| 4.2.2 | Inelastic scattering spectrum | 42 |

| | | |
|----------|---|-----------|
| 4.2.3 | Spin Assignment | 44 |
| 4.2.4 | Discussion | 46 |
| 4.2.5 | Impact on novae | 46 |
| 4.3 | First direct measurement at GANIL (E561S) | 47 |
| 4.3.1 | The experiment | 47 |
| 4.3.2 | Results | 48 |
| 4.4 | Conclusion and Outlook | 50 |
| 4.4.1 | The VAMOS experiment (E641S) | 51 |
| 4.4.2 | The $^{15}\text{O}(\alpha, \alpha)^{15}\text{O}$ experiment (E442S) | 53 |
| 4.4.3 | Study of another γ -ray emitter: ^{22}Na (E710) | 55 |
| 4.4.4 | Related developments | 56 |
| 5 | Light curve of X-ray bursts | 57 |
| 5.1 | Introduction: The XRB-LCP problem | 57 |
| 5.2 | Predicting the rate of $^{15}\text{O}(\alpha, \gamma)^{19}\text{Ne}$ reaction | 59 |
| 5.3 | Conclusion and Outlook | 60 |
| 6 | Unbound Nuclei and Astrophysics | 63 |
| 6.1 | Introduction - Motivations | 64 |
| 6.2 | ^2He in the Sun | 65 |
| 6.3 | ^{19}Na : The first SPIRAL1 experiment (E400S) | 68 |
| 6.3.1 | Astrophysical motivation | 68 |
| 6.3.2 | Principle of the resonant elastic scattering | 69 |
| 6.3.3 | Experiment | 69 |
| 6.3.4 | Results | 71 |
| 6.3.5 | Astrophysical applications | 74 |
| 6.3.6 | Conclusion | 77 |
| 6.4 | ^{18}Na : A masterpiece in the two-proton radioactivity (E521aS) | 78 |
| 6.4.1 | Astrophysical motivation | 78 |
| 6.4.2 | Experiment | 78 |
| 6.4.3 | Results | 81 |
| 6.4.4 | Conclusion | 82 |
| 6.5 | ^{16}F : New pathway to bypass the ^{15}O waiting point (E442S) | |
| | Probing Nuclear forces beyond the drip-line | 83 |
| 6.5.1 | Motivations | 83 |
| 6.5.2 | Experiment | 84 |
| 6.5.3 | Results | 85 |
| 6.5.4 | Interpretation | 85 |
| 6.5.5 | Conclusion and Outlook | 94 |
| 6.6 | ^{15}F : Reefs in the Sea of Instability (E521S) | 95 |
| 6.6.1 | Astrophysical motivation | 95 |
| 6.6.2 | Experiment | 96 |
| 6.6.3 | Results | 97 |
| 6.6.4 | Conclusion and Outlook | 99 |

| | |
|--------------------------------|------------|
| 6.7 Final Conclusion | 100 |
| 7 Conclusion | 101 |

Introduction

Sommaire

| | |
|---|-----------|
| 1.1 Introduction | 1 |
| 1.2 My scientific path | 2 |
| 1.3 The most Important Questions in Nuclear Astrophysics | 2 |
| 1.4 Theoretical Predictions | 5 |
| 1.4.1 The astrophysical factor | 5 |
| 1.4.2 Nuclear statistical model | 7 |
| 1.4.3 Predicting resonances properties | 9 |
| 1.4.4 Direct-radiative-capture | 10 |
| 1.5 Reaction rates | 10 |
| 1.6 Experimental Techniques | 11 |
| 1.6.1 Direct versus Indirect Measurements | 11 |
| 1.6.2 Stable versus Radioactive Beams | 11 |
| 1.7 Organisation of this document | 11 |

La première chose qui s'offre à l'homme, quand il se regarde, c'est son corps, c'est-à-dire une certaine portion de matière qui lui est propre. Mais, pour comprendre ce qu'elle est, il faut qu'il la compare avec tout ce qui est au-dessus de lui, et tout ce qui est au-dessous, afin de reconnaître ses justes bornes.

Les pensées. B. Pascal

1.1 Introduction

It is a big privilege to work in scientific research, and in particular in fundamental research. At the beginning of this 21st century, new and much improved technical means have become available, including new and fast computers and very efficient communication network (when I started my scientific carrier, we used to spend many hours every week in the libraries trying to find and to copy interesting articles). This very favorable environment is a fantastic opportunity to solve some of the unresolved scientific problems, and to show up new natural phenomena.

Nuclear astrophysics makes elegantly the link between the infinitely small and infinitely large worlds. This scientific field has the objective to answer some of the most profound questions: What is the origin of the chemical elements? What is the origin of the stellar energies? How did the Universe evolve?

These questions, alone, clearly justify our researches. By definition, the nuclear astrophysics domain deals with both the Universe made of atomic nuclei and the atomic nucleus universe. The latter is also a fantastic playground for quantum mechanics theory. Solving some of the astrophysical problems means sometimes solving some of the nuclear and quantum mechanics problems. The coupling of nuclear discrete states with the continuum of states of the Universe, in the extreme case the physics beyond the drip lines, are extremely interesting aspects. These problems also fully justify our researches.

1.2 My scientific path

I made my Ph.D. thesis at Orsay in the C.S.N.S.M. laboratory within the group of Nuclear Astrophysics, with Dr. Jean-Pierre Thibaud as the group leader and Dr. Alain Coc as the thesis Director. I worked on the origin of fluorine in the Universe. It was followed by a post-doctoral study for one year at Caen in the GANIL laboratory with Dr. Wolfgang Mittig, where I studied several problems including the properties of several unbound nuclei by transfer reactions using the SPEG spectrometer. After the post-doctoral study, I obtained a CNRS tenure position. I worked at LISE with Dr. Marek Lewitowicz for several years as a scientific collaborator, and later as the LISE Scientific Coordinator. During these years I studied many different kinds of physics, mostly the nuclear structure of radioactive nuclei. I have been the spokesperson or collaborator of more than 100 experiments (more than 200 weeks of beam time). I used 9 different post-accelerated radioactive beams using SPIRAL1 and CYCLONE (Louvain La Neuve) as a spokesperson, including the very first beam of SPIRAL1 (in 2001 just after the terrible events of September 11th). I co-supervised 6 doctoral students and 5 post-doctoral collaborators (many of them being colleagues today). These studies, performed with the help of many students and collaborators, were related to many subjects: Nuclear astrophysics problems; The study of the β -decay, proton, α and two-proton emission mechanisms; Electron screening effects and Nuclear Structure. The present document aims to review some of these studies.

1.3 The most Important Questions in Nuclear Astrophysics

It is a challenge to list all the different questions and problems discussed in nuclear astrophysics, see for example the European Long Range Plan of NUPECC [1], and the plan of IN2P3/CNRS and IRFU/CEA [2] for a quite detailed list of questions. Let's try to summarize some of the main ideas and, at least, to highlight the most important problems in which I have tried to contribute.

The Universe has not always being what it is today. Universe is 13.817 ± 0.048 billion years old [3]. In its birth after the primordial nucleosynthesis, it consisted essentially of hydrogen, helium, and some rare remnants including lithium, ${}^7\text{Li}$ mostly. The measured abundance of ${}^7\text{Li}$ is about 3 times larger than the calculated one, that is much larger than the known uncertainties. This discrepancy constitutes the evidence for a missing brick in the edifice, or for a new physics. The primordial abundance of ${}^7\text{Li}$ is one of the biggest problem in nuclear astrophysics. I have contributed to this subject, see for example Ref. "On Be-9 production in the nonuniform density model of big bang nucleosynthesis" [4], "Big Bang nucleosynthesis with neutral nuclei" [5], and the collaboration work done with F. Hammache "Search for new resonant states in ${}^{10}\text{C}$ and ${}^{11}\text{C}$ and their impact on the cosmological lithium problem" [6].

In stars, regular combustion of the hydrogen occurs, transforming it into helium ($4\text{H} \implies {}^4\text{He}$). This com-

combustion produces energy which avoids the contraction of the stars under the influence of gravity. The stars are then in the main sequence phase, a relatively stable and hydrostatic combustion period. With time, the Universe has enriched itself with heavier chemical elements synthesised in stars. In astrophysics, all elements above helium are called metals. The metallicity of the Sun today is $Z_{\odot} \approx 2\%$. This enrichment continues to occur today. In the heart of these stars, in the hot plasma, the electrons make a screening around nuclei inducing a decrease of the strong Coulomb repulsion potential between nuclei. Thus, the electron screening has to be taken into account during these hydrostatic combustion phases since it modifies the nuclear fusion cross sections. However, the predicted effect of the electron screening is much lower than the measured one in laboratory! This discrepancy is at the origin of an important debate about the modelling of this effect, and about experimental uncertainties and the systematic errors in measuring cross sections at low energy. The electron-screening problem and my contribution to this subject are presented with more details in Chapter 2.

The hydrogen hydrostatic burning phase is then followed by the transformation of helium into carbon and oxygen. At this stage, the star becomes a red giant star. In the latest stage of the red giant phase, the star undergoes thermal instabilities during the Asymptotic Giant Branch (AGB) phase, which generate neutrons and induce a slow process of neutron captures. This nucleosynthesis process is called the s-process, and it is at the origin of half of the elements heavier than iron. It is also an important source of fluorine in the Universe, which origin is not yet well understood. The origin-of-fluorine problem and my contribution to this subject are presented in Chapter 3.

When the mass of the star is larger than ≈ 8 times the solar mass, the helium burning phase is followed by the combustion of carbon, oxygen, silicon into heavier elements up to ^{56}Fe . Beyond this element, the nuclear reactions are endothermic, the star collapses and the inner part of the core is compressed into neutrons until reaching a maximum density value connected to nuclear matter incompressibility. The falling material subsequently bounces and the outward matter flow competes with the downward flow from outer layer of the star to form a shock that forms a type II, core collapse supernova when the explosion is successful. The remaining central part of the star forms a compact neutron star or a black hole. Elements heavier than iron are probably produced by rapid neutrons captures during this explosion. This nucleosynthesis process, called the *r-process*, is at the origin of the other half of the heavier elements. Recently, a new promising site for the production of those nuclei was proposed. It resides in the spiral arms formed in the coalescence of two neutron stars. This scenario is still debated. However, neither the *r-process* nor the *s-process* can synthesis a short list of 35 stable nuclei heavier than iron, these nuclei are called the *p-nuclei*. Their origin is still debated. We started a scientific program to study the origin of these nuclei. Several test experiments were performed, including a recent measurement with a windowless gas target. This work was the subject of the Ph.D. thesis of Predrag Ulic and the post-doc of Giacomo Randisi. Our contribution to this subject is presented in Ref. [7, 8].

Nuclear γ -ray lines emission induced by interactions of energetic particles with the solar atmosphere or with interstellar clouds of gas and dusts are observed with space telescopes. Most of this emission is due to reactions of accelerated protons, ^3He and α -particles with the most abundant nuclei of the solar atmosphere or in the Universe. These spallation reactions constitute also a source of production of the light elements (lithium, beryllium, bore). The intensities of prominent narrow lines allow determination of ambient abundances, as well as composition and energy spectra of accelerated light particles. This study requires the knowledge of the most important nuclear cross sections. I have contributed to this subject

within the collaboration of J. Kiener *et al*, see for example Ref [9].

Astronomer Tycho Brahe observed in 1572 a new star in the constellation Cassiopeia. He described it in his book "De nova stella", giving rise to the name "nova". Although this was a "supernova" and not a "classical nova", the term "nova" has remained and it corresponds today to a peculiar type of astrophysical explosion. The novae are recurrent explosions happening in binary star systems where one of the stars is a compact star called a white dwarf (WD), and the companion is a normal star, see Fig 1.1. A classical nova occurs when a WD is accreting hydrogen-rich material from its companion star. During the nova explosive burning, nucleosynthesis takes place and the newly synthesized material is ejected in the interstellar medium. Multi-wavelength observations of classical novae are performed in order to understand these objects and their associated nucleosynthesis. Among these observations, γ -ray astronomy and the study of presolar grains are of specific interest since they are directly linked to the nucleosynthesis process. However, in order to interpret these observations and therefore to constrain the astrophysical modelling of classical novae, it is crucial to reduce the nuclear uncertainties involved in the production of the isotopes of interest. For classical novae almost all the reaction network is determined experimentally with a sufficient precision, with a few exceptions such as the $^{18}\text{F}(p,\alpha)^{15}\text{O}$ and $^{22}\text{Na}(p,\gamma)^{23}\text{Mg}$ reactions. The rate of these reactions can be determined indirectly from the spectroscopic properties of states located above particle emission threshold of the compound nucleus. In this context, the ^{19}Ne -spins problem and my contribution to this subject are presented in Chapter 4.

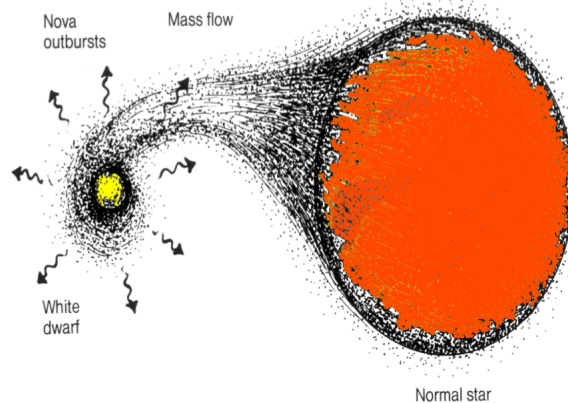


Figure 1.1: Schematic drawing of a nova outburst (internet, unknown origin).

Recurrent explosions also occur in other type of binary systems, where the WD star is replaced by a neutron star. These explosions are called Type I X-ray bursts. With a neutron star as the underlying compact object, temperatures and densities in the accreted envelope reach extreme values ($T_{peak} > 10^9$ K and $\rho \approx 10^6$ g.cm⁻³) leading to a thermonuclear runaway and a sharp increase of the X-ray emission. The thermonuclear explosion is triggered by the triple α -process and the $^{15}\text{O}(\alpha,\gamma)^{19}\text{Ne}$ reaction, this is discussed in Chapter 5, and is driven by the α p-process (a sequence of (α,p) and (p,γ) reactions) and the rp-process (rapid proton-captures and β^+ -decays) towards the proton drip line. These extremely neutron deficient nuclei, including some unbound nuclei, are interesting to study since they could influence the light curve profile, and also because unbound nuclei are perfect cases to study the coupling of discrete states with continuum. Several studies of unbound nuclei are presented in Chapter 6.

Many nuclear input parameters, such as the nuclear masses or the incompressibility of the nuclear matter, have also an important impact in astrophysics models. I do not intend to discuss in this document all the important parameters, but only some I have studied. In many astrophysical codes, reactions rates are the most important nuclear ingredients. These are defined as the product of the nuclear reaction cross sections with the Maxwell-Boltzmann energy distribution at a given temperature T of the stellar environment. Reaction rates can be calculated easily if the nuclear cross sections are measured experimentally or if they can be predicted.

1.4 Theoretical Predictions

Some of the astrophysical problems listed above could be fixed if the cross sections of some nuclear reactions were known at very low incident energies (for example, in the Sun $E_{inc}^{mean} \approx 5.9$ keV). The most important cross sections are those located in the range of energies called the Gamow window, that is the energy range where the probability of reaction is the highest at a given temperature of the stellar environment. The Gamow window can be calculated approximatively using the following formula [10]:

$$E_0 = 1.22(Z_1^2 Z_2^2 \mu T_6^2)^{1/3} keV,$$

$$\Delta = 0.749(Z_1^2 Z_2^2 \mu T_6^5)^{1/6} keV.$$

The quantity E_0 and Δ are the effective mean energy and energy width of the Gamow window, Z_1 and Z_2 are the charges of the interacting nuclei, μ is the reduced mass in amu, T_6 is the temperature in million Kelvins.

In nuclear astrophysics, the main problem is that the fusion cross sections decrease considerably when going low with the energy, see Figure 1.2 (top). In most of the cases, the cross section are so low that it is very difficult or impossible to measure them. Can we predict these cross sections at low energy?

1.4.1 The astrophysical factor

Astrophysical energies correspond to incident energies well below the Coulomb barrier. Fusion reactions are possible only through the quantum tunnel effect. It is very convenient to write the astrophysical cross sections as

$$\sigma(E) \equiv \frac{S(E)}{E} e^{-2\pi\eta} \quad (1.1)$$

where

- The Coulomb effect is set apart from the total cross section using the factor $e^{-2\pi\eta}$, i.e. the penetrability of the charged particle by tunnel effect through the Coulomb barrier. The factor $-2\pi\eta$ can be calculated as

$$2\pi\eta = 31.29 Z_1 Z_2 \left\{ \frac{\mu (amu)}{E (keV)} \right\}^{1/2} \quad (1.2)$$

- The factor E^{-1} is a non-nuclear energy-dependant term corresponding to the de Broglie wavelength dependence, another quantum effect.

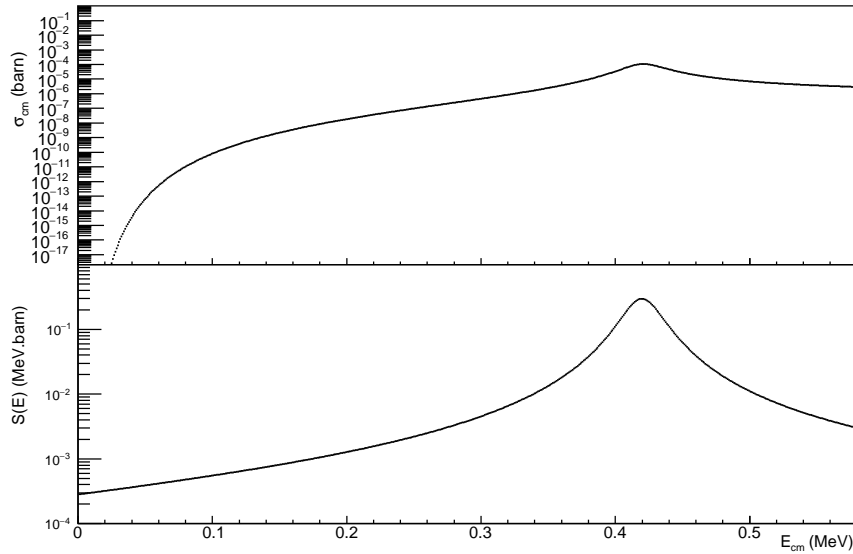


Figure 1.2: The calculated $^{12}\text{C}(p,\gamma)^{13}\text{N}$ cross section (top) and astrophysical factor $S(E)$ (bottom) as a function of the c.m. energy. A resonance is observed at the energy of 421.9 keV which corresponds to the presence of an excited state at the energy of $E_x = 2365$ keV in the compound nucleus ^{13}N . The nuclear dependance of the cross section, i.e. $S(E)$, varies slowly with the energy when going down to the Gamow window ($E_0 \approx 30$ keV in the case of the sun).

- The nuclear dependance of the cross section is summarized in the function $S(E)$ called **the astrophysical factor**. Compared to the cross section, it is a function depending slowly on the energy, see Figure 1.2 (bottom).

One can classify the different nuclear reactions in different groups depending on their $S(E_0)$ [11]. In general, the reactions involving only nuclear processes, like the (α,n) reaction, have the highest $S(E_0)$, the reactions involving electromagnetic processes are lower, and weak interaction even lower. The Figure 1.3 is useful when trying to predict an unknown cross section. From the figure, one can see that the precision of the "prediction" is not good. There might be an uncertainty reaching a factor of 10^8 . In many cases, including the cases discussed in the previous sections, this precision is not sufficient at all.

When dealing with heavier nuclei, the impact of the Coulomb repulsion on the cross section is considerably higher since the penetrability decreases exponentially with the charge of the nuclei. Surprisingly, it is observed that the nuclear part of the cross section $S(E)$ also increases considerably, to such values that it compensates the strong reduction of the penetrability! For example, $S(E)=5 \times 10^{26}$ MeVb in the case of $^{141}_{59}\text{Pr}(\alpha,n)^{144}\text{Pm}$ [12] at the Gamow window, resulting into a cross section of $\sigma=8 \mu\text{b}$ at $E_\alpha=11.047$ MeV (Coulomb barrier being $B_C=17.3$ MeV). This striking coincidence is due to two effects:

- Firstly, the penetrability is poorly described by the term $e^{-2\pi\eta}$. For example, in the case of the reaction $^{141}\text{Pr}(\alpha,n)^{144}\text{Pm}$, this term gives 7×10^{-31} whereas a numerical calculation using regular and irregular Coulomb functions [10] gives $\simeq 10^{-4}$. In other words, the nuclear $S(E)$ factor has to compensate the too low value of the Coulomb penetrability calculated with the term $e^{-2\pi\eta}$.

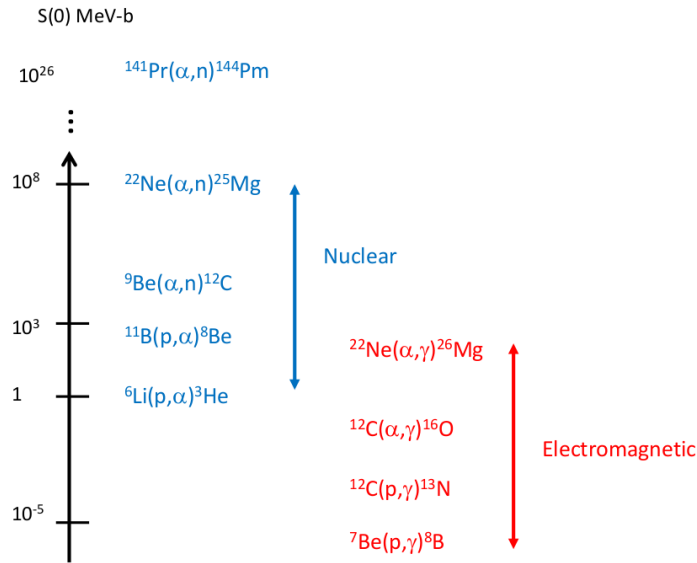


Figure 1.3: Calculated or measured astrophysical factors $S(E_0)$ for different nuclear reactions, from Ref. [11]. The reactions can be classified in two different groups.

If the following relation

$$\sigma(E) \equiv \frac{S_N(E)}{E} P_\ell(E) \quad (1.3)$$

is used, where $P_\ell(E)$ is the penetrability calculated numerically using the incident angular momentum $\ell = 0$, a better picture is obtained, see Fig. 1.4. To my knowledge, it is the first time this much better picture is shown. One can see that the precision of the "prediction" on $S_N(E_0)$ is much better. Whatever may be the mass of the nuclei, the uncertainty is "only" a factor 10^2 . This uncertainty is irreducible since it comes from the presence or not of resonances in the Gamow window, or interferences between different resonances. One example of uncertainties due to possibility of interferences between different resonances is discussed in Chapter 3 in the case of the reaction $^{18}\text{F}(p,\alpha)^{15}\text{O}$.

- Secondly, the density of states increases considerably when going to heavier nuclei, inducing a real increase of the nuclear contribution $S(E)$. In the case of ^{141}Pr at $E_x=8.7$ MeV, the levels density is $\rho \approx 10^8 \text{ MeV}^{-1}$ [13]. To take into account the increase of the level density, it is possible to use the nuclear statistical model.

1.4.2 Nuclear statistical model

The partial waves expansion model [14] shows that the cross section σ_i for the formation of the compound nucleus, from a pair of interacting particles with a given value of the orbital angular momentum ℓ , can be calculated with the following formula:

$$\sigma_i = \frac{\pi}{k^2} (2\ell + 1) T_i \quad (1.4)$$

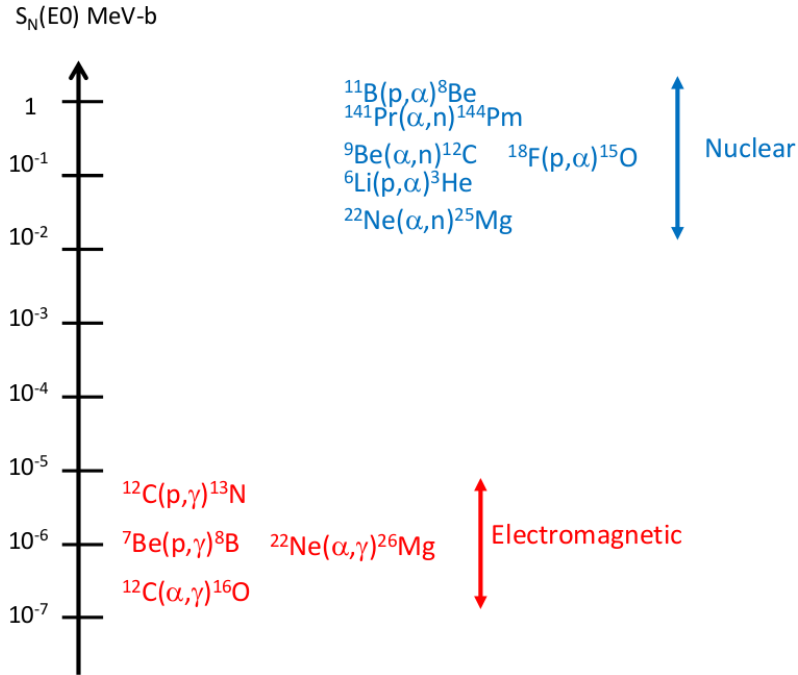


Figure 1.4: Astrophysical factors $S_N(E_0)$ using a corrected penetrability. To my knowledge, this is the first time this plot is shown. It has the advantage to split the nuclear reactions clearly into two groups. Within one group, the spread of values is much reduced compared to the spread shown in Fig. 1.3.

where T_i is the transmission coefficient. At the most, $T_i=1$. In the compound-nucleus model, the nuclear reactions are described as a two-stage process comprising the formation of a long-lived intermediate nucleus and its subsequent decay. The probability of forming an excited state in the compound nucleus in channel i is independent of the probability of decay in channel f . It follows that the cross section to go from the initial channel i to the final channel f can be expressed as

$$\sigma_{i,f} = \frac{\pi}{k^2} (2\ell + 1) \frac{T_i T_f}{\sum_{\gamma} T_{\gamma}}. \quad (1.5)$$

The cross section should be averaged over all overlapping resonances of the compound nucleus:

$$\sigma_{i,f}(E) = \frac{\pi}{k^2} \sum_{J, \pi} \frac{2J + 1}{(2J_1 + 1)(2J_2 + 1)} \frac{T_i(E, J, \pi) T_f(E, J, \pi)}{\sum_{\gamma} T_{\gamma}(E, J, \pi)} \quad (1.6)$$

where J_1 and J_2 are the intrinsic spins of the initial pair of particles, J, π, E the spin, parity and excitation energy of the compound nucleus excited states, T_i and T_f are respectively the transmission coefficient of the initial and final channels. The expression above corresponds to the **Hauser-Feshbach (HSFB)** cross section [15]. One example of HSFB calculations is shown in Chapter 3.

The transmission coefficient $T_f(E, J, \pi)$ is simply the sum over all excited states of the outgoing nucleus:

$$T_f(E, J, \pi) = \sum_{v=0}^{v_{max}} T_f(E, J, \pi, E_f^v, J_f^v, \pi_f^v). \quad (1.7)$$

where J_f , π_f , E_f are the spin, parity and excitation energy of the excited states of the outgoing nucleus and the summation is up to the highest experimentally known state v_{max} . When the density of states is so high that they can be considered as a continuum of states, the sum of the transmission coefficient is transformed into an integral on the density of nuclear levels ρ

$$\int_{E_{max}}^{E-S} \sum_{J_f, \pi_f} T_f(E, J, \pi, \varepsilon, J_f, \pi_f) \rho(\varepsilon, J_f, \pi_f) d\varepsilon \quad (1.8)$$

where S is the channel separation energy. The averaged transmission coefficient of charges particles can be calculated numerically from optical model potentials. Generally, γ -ray transmission coefficient, masses, level densities and the other parameters are taken from tables and semiempirical formula [16]. Several codes are available to predict the astrophysical cross sections (NON-SMOKER (<http://nucastro.org/websmoker.html>), TALYS (<http://www.astro.ulb.ac.be/pmwiki/Brusslib/Talys>), PACE...).

We observe generally a difference between the predicted cross sections using the nuclear statistical model and the measured ones that can be a factor 0.1 to 10 (see Ref. [17] for neutron capture cross sections). Uncertainties still remains on some parameters used in the models, specially for nuclei far from stability. One example of this problem is given in Ref [7].

1.4.3 Predicting resonances properties

The statistical model is not adapted to light nuclei, for nuclei close to magic numbers, and for low excitation energies. Isolated resonances are observed and should be taken into account with a more appropriate formalism. The Breit-Wigner formula for a single-level resonance is the most often used

$$\sigma_{i,f}(E) = \pi \tilde{\chi}^2 \frac{2J+1}{(2J_1+1)(2J_2+1)} \frac{\Gamma_i(E)\Gamma_f(E)}{(E-E_R)^2 + (\frac{\Gamma_{Tot}(E)}{2})^2}. \quad (1.9)$$

Nuclear models, e.g. the shell model, can be used to predict the properties (resonance energies E_R , widths Γ and spins J) of these important resonances for nuclear astrophysics. Despite important progresses the last years, for example in taking into account the coupling with the continuum, none of these models have achieved enough precision for direct application in astrophysics. Excitation energies are needed with, at least, a precision of 100 keV. None of the nuclear models has this precision. Sometimes, resonances of the same spin and parity interfere, inducing a large impact on nuclear cross sections. Some models can predict the sign of the interferences, but they have to include the coupling with the continuum and the states have to be described very well, this is due to the fact that the sign of interferences is sensitive to small components of the wave functions. Sometimes, the unknown properties of the states are taken from the measured ones in the mirror states. This technique was often used in the studies presented in this document, but these studies have also shown that great care should be taken (see Chapter 3 and 6). Some isospin "asymmetry" exist, and has to be taken into account. Several tests cases are discussed in Chapter 6, specially the case of ^{16}F and ^{16}N . If theory is of great help in extrapolating the cross sections to lower energies, or in predicting the existence of important states (see Chapter 4 for the predictions of important $\frac{1}{2}^+$ states in ^{19}Ne), many of these important state properties have to be measured.

1.4.4 Direct-radiative-capture

In contrast to the resonant reactions, the direct-radiative-capture reaction is an entirely electromagnetic process similar to the bremsstrahlung process. The cross section of the direct-radiative-capture reaction $A(x,\gamma)B$ is described by a single matrix element,

$$\sigma_{i,\gamma}(E) \propto |\langle B | H_\gamma | A + i \rangle|^2, \quad (1.10)$$

where H_γ is the electromagnetic operator. This direct-radiative-capture process is nonresonant because it can occur at all projectile energies with a cross section varying smoothly with energy. The main contribution comes from E1 capture reactions, since in general E1-transitions are the fastest electromagnetic transitions. It can be written

$$\sigma_{i,\gamma E1}(E) \propto \langle r \rangle^2$$

$$\langle r \rangle = \int_0^\infty u(r) r \phi_{scattering}(r) dr$$

where $u(r)$ is the radial wave function of the bound state $B=A+x$, which is proportional to the spectroscopic factor $\langle B | A + x \rangle$, and $\phi_{scattering}(r)$ is the scattering wave function in the entrance channel. This type of reaction mechanism could be the major part of the cross section at low energy and should also be taken into account. One example of direct-radiative-capture calculation is presented in Chapter 3 in the case of the $^{19}\text{F}(\alpha,\gamma)^{23}\text{Ne}$ reaction.

1.5 Reaction rates

Nuclear cross sections are not used directly into astrophysical models, because it is not convenient, reaction rates are used instead. Suppose an astrophysical environment with a plasma heated at high temperatures. In this plasma, two nuclei 1 and 2 are transformed into nuclei 3 and 4 through the nuclear reaction: $1 + 2 \rightarrow 3 + 4$. If the nuclei 1 and 2 have a relative velocity between v and $v + dv$, the number of reactions dr per unit of volume and per second is given by

$$dr = N_1 N_2 \Phi(v) v \sigma(v) dv \quad (1.11)$$

where $\Phi(v)dv$ is the probability to get the relative velocity between v and $v + dv$, N_1 and N_2 the density of nuclei 1 and 2, and $\sigma(v)$ the cross section of the nuclear reaction.

The reaction rate r is defined as:

$$r = N_1 N_2 \langle \sigma v \rangle = N_1 N_2 \int_0^\infty \Phi(v) v \sigma(v) dv. \quad (1.12)$$

Generally, the density of probability $\Phi(v)$ used is the Maxwell-Boltzmann velocity distribution formula. This gives:

$$\langle \sigma v \rangle = \sqrt{\frac{8}{\pi m}} (kT)^{-\frac{3}{2}} \int_0^\infty \sigma(E) E e^{-\frac{E}{kT}} dE \quad (1.13)$$

Reaction rates are usually fitted into analytic expressions of the temperature.

1.6 Experimental Techniques

1.6.1 Direct versus Indirect Measurements

Direct measurement of the nuclear reactions cross sections at low energy is very difficult because of their extremely low values. In this document, two cases of direct measurements are discussed: in Chapter 4 for the reaction $^{18}\text{F}(p,\alpha)^{15}\text{O}$ and in Chapter 6 for the reaction $^{14}\text{O}(\alpha,p)^{17}\text{F}$. In many other cases, many different techniques of indirect measurements, i.e. transfer reactions, Coulomb excitation and breakup reactions, Trojan horse method, resonant elastic scattering reactions, doppler shifts attenuation method, β -decays studies, were performed in order to determine the parameters needed in the nuclear models (e.g. in the Breit-Wigner formula) in order to calculate accurately the nuclear cross sections. Indirect measurements are very often used, see examples in Chapters 3, 4 and 6. But, there is one important parameter that cannot be determined indirectly, this is the sign of the interferences between resonances of the same spin and parity involved in the reaction. In this case, the only way to determine the sign is to measure directly the cross section, at least at one energy. Thus, direct and indirect measurements are complementary.

1.6.2 Stable versus Radioactive Beams

Stable beams are often used to perform indirect measurements for nuclear astrophysics (see one example in Chapter 3). Sometimes, for some properties such as spectroscopic factors, stable beams cannot be used. In that case, radioactive beams are the only solution. Radioactive beams can be very challenging for several reasons. They are less intense. Typically, one week of radioactive beam is equivalent to one second of stable beam in terms of incident particles. Generally, radioactive beams have also poorer beam quality, in terms of emittance and purity. In general, post-accelerated beams (SPIRAL1) have much better beam quality than in-flight fragmented beams (LISE). The GANIL Facility can produce in-flight and post-accelerated radioactive beams in the range of energies between 1.2 MeV/u and ~ 50 MeV/u depending on the element. Light and medium mass radioactive beams can be produced at the LISE fragment separator in the energy range 10-50 MeV/u by the fragmentation of primary stable beams, e.g. ^{60}Fe was produced at 27 MeV/u with 10^5 pps and 70% purity. At GANIL, the ISOL technique is also employed in the SPIRAL1 facility to produce and then to post-accelerate radioactive beams (He, N, O, F, Ne, Ar, Kr) from 1.2 MeV/u up to 25 MeV/u, e.g. ^{18}F was produced with 2×10^4 pps and 97% purity, ^{19}Ne with 5×10^7 pps and 100% purity. With the advent of intense radioactive beams, new opportunities have opened in nuclear astrophysics.

1.7 Organisation of this document

This manuscript is organised in different chapters. Each chapter can be read independently and presents one problem in astrophysics studied through one or several experiments (using sometimes different approaches). These studies allowed to improve our understanding of the astrophysical problem addressed. These chapters correspond to a selection of studies I have worked in, and that have been published in refereed journals. Table 1.1 summarizes the list of the different experiments discussed in this document. Each chapter ends with a "conclusion and outlook" section, summarizing the study and giving new ideas and several possible new experiments to go further in our understanding.

Table 1.1: List of the experiments discussed in this document.

| Chapters | Astrophysical problems | Experimental Method | | Beams | |
|----------|--|----------------------------------|--|------------------|---|
| | | Direct | Indirect | Stable | Radioactive |
| 2 | Electron screening effect | - | β -decay | - | ^{19}Ne and ^{19}O |
| 3 | Origin of ^{19}F | - | $^{15}\text{N}(^7\text{Li},\text{t})$ | ^7Li | - |
| 4 | γ -rays from Novae | $^{18}\text{F}(\text{p},\alpha)$ | $^{19}\text{Ne}(\text{p},\text{p}')$ $^{15}\text{O}(\alpha,\alpha)$ $^{24}\text{Mg}(^3\text{He},\alpha)$ | ^{24}Mg | ^{19}Ne , ^{18}F , ^{15}O |
| 5 | Light curve of X-ray bursts | - | Yes | - | - |
| 6 | Two-proton captures and unbound nuclei | - | (p,p) | - | ^{18}Ne , ^{17}Ne , ^{14}O , ^{15}O |

Electron Screening Effect

Sommaire

| | | |
|------------|---|-----------|
| 2.1 | Introduction: The electron-screening problem | 13 |
| 2.2 | β-decay in a superconductor (E578S) | 15 |
| 2.2.1 | Experiment at SPIRAL1 with Niobium | 16 |
| 2.2.2 | Analysis | 20 |
| 2.3 | Conclusion and Outlook | 22 |
| 2.3.1 | Summary | 22 |
| 2.3.2 | A new High-precision experiment (E558S) | 22 |
| 2.3.3 | Outlook | 23 |

Quand bien nous pourrions être savants du savoir d'autrui, au moins sages ne pouvons-nous être que de notre propre sagesse.

Essais. Montaigne

2.1 Introduction: The electron-screening problem

The cloud of electrons surrounding the atomic nucleus is known to act as a screening potential [18]. The effect of this screening potential is to reduce the Coulomb barrier, see Fig. 2.1. The electrostatic potential of the electrons cloud at distances less than the atomic radius R_a is constant, approximately equal to $\frac{Z_1 e}{R_a}$. The effective height of the Coulomb barrier seen by an incoming projectile is $\frac{Z_1 Z_2 e^2}{R_n} - \frac{Z_1 Z_2 e^2}{R_a}$. The penetration through this shielded Coulomb potential at projectile energy E_s is equivalent to the penetration of a bare nucleus at projectile energy $E = E_s + U_e$, where $U_e = \frac{Z_1 Z_2 e^2}{R_a}$ is called the electron screening energy. When calculating the astrophysical cross section $\sigma(E) \equiv \frac{S(E)}{E} e^{-2\pi\eta}$ (Equ. 1.1) for shielded nuclei, the energy E for the bare nuclei must be replaced by the energy $E_s = E - U_e$. The induced enhancement of the nuclear cross sections goes exponentially with decreasing energy of the projectile [10, 14], $\sigma(E)_{shielded} = \sigma(E)_{bare} e^{\pi\eta \frac{U_e}{E}}$. It was first pointed out by H.J. Assenbaum *et al* in 1987 [19] that electron screening could play an important role in astrophysics during the quiescent burning phases in stars, since it modifies the nuclear cross sections at low energies in the Gamow region. It is also important to note that the electron screening must be taken into account in laboratory since the measured cross sections at very low energies are modified from the presence of electrons in the target atoms.

This increase of the nuclear cross section at low energies was observed in several cases and the measured electron screening energy U_e is typically of the order of 100 eV. It is possible to predict the electron

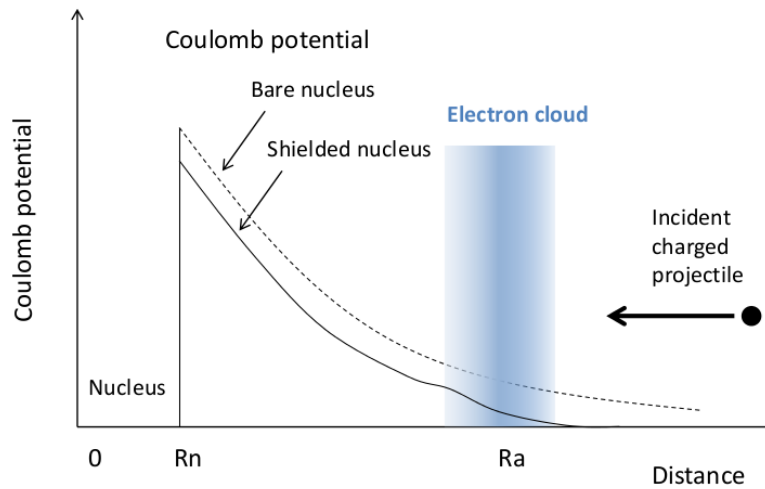


Figure 2.1: The effect of the atomic electron cloud on the Coulomb potential of a bare nucleus is shown very schematically (from ref. [19]). This potential is reduced from the nucleus radius R_n to the atomic radius R_a , and cancelled outside R_a .)

screening energy, in general it is a function of energy, but it is a good approximation to express the enhancement of measured cross sections in terms of a constant value. When the orbital speed of electrons is much higher than the speed of the incident nuclei, this is the case for the astrophysical energies, electrons can adjust "immediately" their configurations following the configuration of atomic nuclei (Born-Oppenheimer approximation). The maximal theoretical screening energy produced by the atomic electrons can be calculated as the difference between the sums of the binding energies of all the electrons of the entrance channel and the exit channel [19, 20]. The binding energy gained or lost by electrons is given to the incident nuclei. This case is called the "adiabatic limit" and it should constitute the maximum screening energy possible. In many cases, direct measurements of nuclear reactions at low energies have shown that the measured electron screening energy is significantly larger than the adiabatic limit. This problem was confirmed later by indirect measurements using the Trojan Horse method. This problem is called the electron screening problem, and it has become one of the major problems in nuclear astrophysics.

Many studies have been performed in order to solve the electron screening problem and the problem is still not solved, see Ref. [21]. One of the main ideas was that the environment could be at the origin of some unknown effects. Logically, nuclear reactions were measured in different environments (gas, metallic, insulators, alloys, semiconductors) in order to compare the electron screening energies measured for the same reaction but induced in different materials. Surprisingly, extreme values of U_e , larger than 500 eV and sometimes several keV, were measured in metallic materials, see Ref [22, 23] and references therein. Various aspects of the metals were discussed to explain the data, stopping power, thermal motion, channeling, diffusion, conductivity, crystal structure, electron configuration; however, none of these aspects led to a solution. The question remained: what is the acceleration mechanism leading to the high observed U_e values? F. Raiola *et al* pointed out in 2004 [23] that the large effects measured in metals are in agreement with the classical plasma screening of Debye applied to the quasi-

free metallic electrons.

It was pointed out in 2006 by K.U. Kettner *et al* [24] that, if this simple Debye model is the correct explanation of the electron screening problem, it should also modify significantly the lifetime of radioactive nuclei implanted in these materials. As an example, it was calculated that the α -decay of the biologically dangerous transuranic waste ^{226}Ra ($T_{1/2}=1600$ years) could be reduced to $T_{1/2}=1.3$ years. After the publication of K.U. Kettner *et al* [24], many experimental studies were undertaken to check if lifetimes are changed in metallic environments.

Electron screening can modify lifetime of radioactive nuclei, this was first pointed out by M.E. Rose in 1936 [25]. From the theoretical point of view, since these environmental effects do not modify the nuclear matrix elements M_{fi}^2 , the product of the β -decay Fermi function $f(Z, Q)$ and the half-life t should remain constant, $ft = \frac{cte}{M_{fi}^2} = cte$. Hence, the change of the β -decay rate can be calculated as $f(Z, Q') \cdot t' = f(Z, Q) \cdot t$, where $Q' = Q_\beta + U_e$ is the modified Q_β value and t' is the new half-life [25]. For example, in the Nuclear Data Tables of Ref. [26], in the case of the β^+ -decay with $Z = 10$, $A = 20$ and $E(\beta^+) = 50$ keV, it is calculated $\text{Log}f = -4.643$ with screening and $\text{Log}f = -4.671$ without screening. The screening results in a shorter half-life for the β^+ emission whereas it is longer in the β^- case (U_e positive or negative).

The first two experimental results concerning this question were published in 2006 by B. Wang *et al* [27] and by B. Limata *et al* [28]. In the first case, a 0.9(2) % change of the lifetime of ^7Be implanted in Pd was observed at 12K, and in the second case the β^+ -decay lifetime of ^{22}Na implanted in the metallic environment Pd cooled to $T = 12$ K was observed to be shorter by 1.2(2) %. This was a big surprise and the impact of this new explanation was the subject of important debates in conferences (FINUSTAR in 2005 for example). These results were followed by many other experimental studies confirming or rejecting the high effect and the Debye model for the explanation of the electron screening problem in metals.

2.2 β -decay in a superconductor (E578S)

In 2009, in the context described in the previous section, we proposed to perform a new experiment (E578S) in order to test this Debye modeling of the electron screening in metals. Three new ideas were presented in this new study:

- In the β -decay, when several decay branches are open, the relation $f(Z, Q - E_x) \cdot t^{(i)} = f(Z, Q' - E_x) \cdot t'^{(i)}$ should be used for each individual branch i in order to calculate the new partial half-lives $t'^{(i)}$. It results in a new half-life $1/t' = \sum_i 1/t'^{(i)}$ and new branching ratios $BR'^{(i)} = t'/t'^{(i)}$. Hence, we predicted that the environment can modify the half-life of the nucleus and also the β -decay branching ratios (BR). This last effect had not been previously discussed nor observed. It could be used to demonstrate that the observed differences are due to the electron screening and not from another effect.
- The Debye model is based on classical physics, it is not appropriate to describe fermions in metals. We should be surprised that the measured electron screening energies are in agreement with the predictions of the Debye model (several keV effect) and not with the Thomas-Fermi model (≈ 100 eV effect). In opposite, electrons are organized in Cooper pairs in superconductors. If the electron pairs behave as Bose particles and are subject to only elastic interactions with the ions, then each of the paired electrons follows a Bose-Einstein distribution, which is in better agreement

Table 2.1: Predicted changes of the half-life and BR of ions implanted in a Niobium host in its superconductor phase (4K) relatively to their values in the metallic phase (16K). These values were calculated using differences in screening potential energy of $U_e(^{19}\text{O}) = -20.9$ keV and $U_e(^{19}\text{Ne}) = +25.8$ keV.

| | Expected change |
|---|-----------------|
| ^{19}O half-life | +2.5% |
| ^{19}O BR to the state at 197 keV | +0.55% |
| ^{19}O BR to the state at 1554 keV | -0.24% |
| ^{19}O BR to the state at 4377 keV | -14.3% |
| ^{19}Ne half-life | -5.0% |

with the Debye predictions. Stoppini [29] predicted that the local density of electrons around the nuclei could be higher than in the normal phase, a strong electron screening ($U_e > 10$ keV) effect, called “superscreening”, could happen in these materials. We proposed to study, for the first time, the β -decay of ions implanted in a superconductor material, and to observe this predicted superscreening effect. This idea was later called one of the best ideas by Claus Rolfs [30].

- This study was undertaken using intense radioactive beams, high statistics and efficient detectors. In general, high precision half-life measurements are challenging because of the many possible sources of systematic errors, like contamination of the beam, acquisition dead time, diffusion of the nuclei inside the host-material, pile-up effect and beam or electronic instabilities. A new and very optimized experimental setup was proposed in order to minimize the influence of all these uncertainties on the results.

2.2.1 Experiment at SPIRAL1 with Niobium

Two nuclei: ^{19}O and ^{19}Ne , were investigated. These nuclei decay by β^- and β^+ with half-lives of 26.464(9) s [31] and 17.262(7) s [32], respectively. The isotope ^{19}O has 3 main decay branches: to the 197 keV level in ^{19}F with BR of 45.4(15) %, to 1554 keV with 54.4(12) % and to 4377 keV with 0.098(3) % [33]. The isotope ^{19}Ne decays mainly to the ground state of ^{19}F . An accurate measurement of these properties for nuclei implanted in a superconductor can be used to determine the screening potential energy U_e in this material. Conversely, it is possible to predict the effects on half-life and BR if U_e is known. One can suppose that U_e is negligible in metal and that U_e is equal to the Debye energy in superconductor [29]. In the case of the Debye plasma model [24], $U_e = 2.09 \times 10^{-11} (Z_t(Z_t + 1))^{1/2} (n_{eff} \rho_a / T)^{1/2}$ (eV), with Z_t the charge of the parent nucleus, $n_{eff} \sim 1$ the number of free-electrons per atom of Niobium, ρ_a the atomic density in units of atoms m^{-3} , in Niobium it is $\rho_a = 5.56 \times 10^{28}$ atoms m^{-3} . Using this formula, one calculates at temperature of 4 K: $U_e(^{19}\text{O}(\beta^-)) = -20.9$ keV and $U_e(^{19}\text{Ne}(\beta^+)) = +25.8$ keV. The Fermi function $f(Z, Q + U_e)$ cannot be calculated analytically, although it could be estimated very precisely by numerical methods [34]. Using the previous values of U_e , one obtains the results presented on Table 2.1. The predicted changes are relatively small but these are measurable and the effect is unambiguous.

The radioactive nuclei were produced by the SPIRAL1 facility at GANIL, accelerated to 6 MeV/u and

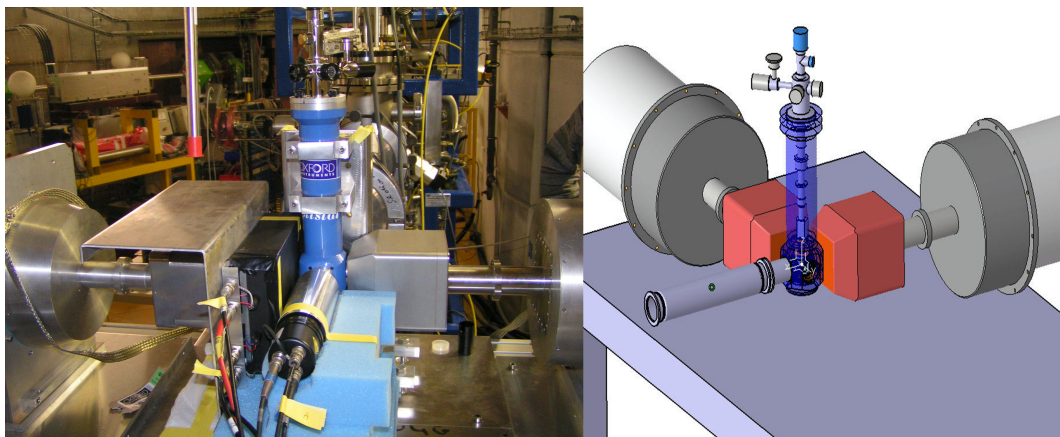


Figure 2.2: The experimental setup used in this experiment including a cryostat based on liquid helium (the blue cylinder), two EXOGAM clover detectors, a LaBr₃ detector and a plastic scintillator detector (the black box).

purified using a stripper foil. The purity was checked periodically with a silicon detector. In the case of the ^{19}Ne beam, the purity was measured to be 99.9(1) %. In contrast, the ^{19}O beam had a contamination by 1.23(10) % of ^{19}Ne and 45(1) % of ^{19}F . The presence of the first contaminant was taken into account in the analysis, whereas the second has no effect on all measurements since it is a stable nucleus. The ions were implanted into a 100 μm thick niobium foil. Since the ions are implanted deep into the target, diffusion and leakage of the ions can be neglected (this was checked using standard diffusion coefficients). Niobium is a superconducting metal with a critical temperature of 9.2 K. The OptistatCF-VTM cryostat of Oxford Instruments (see Fig. 2.2) was used for the cooling of the niobium foil. The temperature stability was monitored for several minutes after each change (see later). No fluctuation larger than 0.5 K was observed.

The detection system consisted of two EXOGAM germanium clover detectors [35], a BaF₃ scintillator detector and one plastic scintillator detector. The detectors were located between 6 and 10 cm around the target. The γ -ray detectors were used for the BR measurements. The β -particles were detected with the plastic scintillator and used to determine the half-life. The plastic detector had a thickness of 500 μm , an area of 5cm \times 5cm and an absolute efficiency of 3(1) % to detect the beta particles. A relatively thin detector was used in order to reduce its efficiency to detect gamma rays. The plastic scintillator was connected to two Hamamatsu R2102 photomultipliers (see Fig. 2.3).

The plastic scintillator, photomultiplier and electronic were optimized in order to obtain ultra fast signals (< 4 ns) and to reduce the dead time (see Fig. 2.4).

To reduce the systematic effect called "afterpulsing" [32], the two plastic signals were used in a coincidence mode. The background counting was of ~ 3 counts per second. To limit the "gain shift" and "baseline" systematic effects [32], the beam intensity was limited to measure a maximum counting rate of 3×10^3 Hz. In doing so, no significant rate dependence of the half-life was observed. The plastic detector signal was connected to a scaler module through a gate generator with a constant width of 10 ns. Since the scaler module can sustain a frequency of 100 MHz, the dead time of the half-life measurement was practically negligible, at the maximum of the counting rate the correction was of 0.01 %. The beam implantation time was chosen to last for two half-lives. It was followed by a measurement during

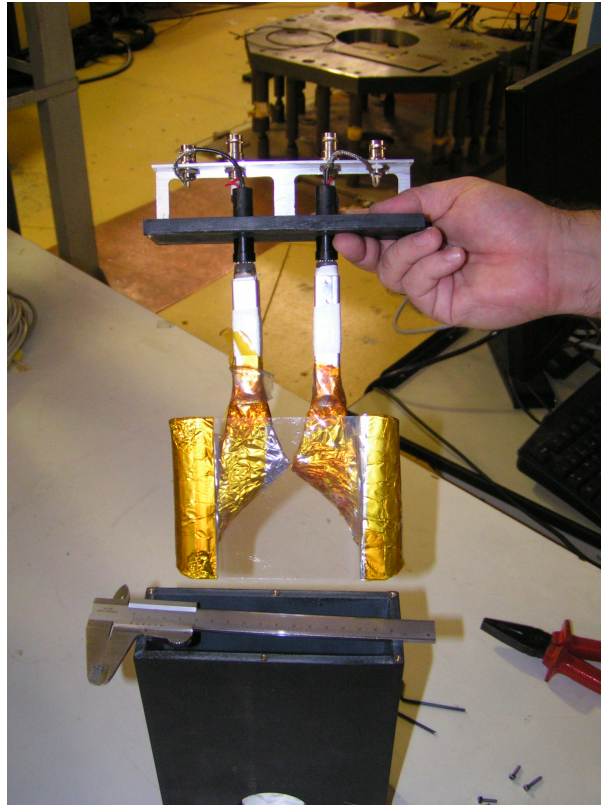


Figure 2.3: The plastic scintillator with two photomultipliers.

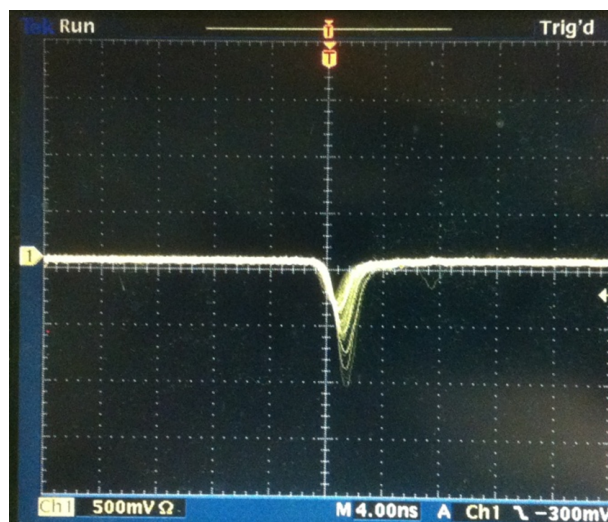


Figure 2.4: Output signals measured with an oscilloscope. The plastic scintillator, photomultiplier and electronic were optimized in order to obtain ultra fast signals (< 4 ns) and to reduce the dead time.

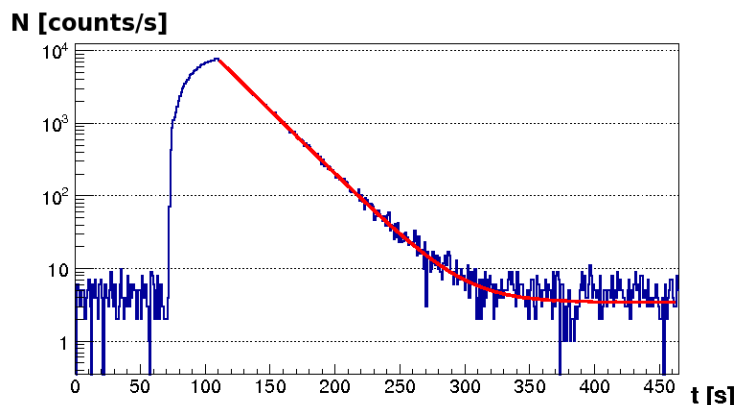


Figure 2.5: An example of implantation-decay curve of ^{19}Ne measured at 4K. The fit of the decay curve was performed using an exponential function plus a constant background. In this example, $t_{1/2} = 17.22 \pm 0.04$ s and $\chi^2/\nu = 1.01$.

which the beam was cut off and the β -decay measured. The measurement time was chosen to last 20 half-lives in order to search for a temporal variation of the background after implantation. In order to reduce possible systematic effects, the measurement was performed in one-hour cycles. During one hour, several implantation-measurement cycles were performed at low temperature (4K) in the superconducting phase, then the temperature was raised to 16K and several implantation-measurement cycles were performed in the metallic phase, which was followed by a new one-hour measurement at 4K, and so on. This gave a first set of runs (I) with temperatures 4K and 16K. This experimental approach allowed us to reduce strongly several systematic effects. If, for example, one parameter of the experiment were to change slowly over time, the change would affect equally the two measurements made almost simultaneously and with the same experimental setup. When sufficient statistics was achieved, new cycles were performed with a higher difference in temperature (4K-90K) in order to examine possible temperature dependence of the effect as predicted by the Debye screening model [24]. This gave the second set of runs (II) with temperatures 4K and 90K.

The influence of the beam manifests in two ways: a heating of the target which could induce a phase transition from superconducting to normal state, and a lattice damage which changes the critical temperature of the target. The beam power deposited into the target was $10 \mu\text{W}$. In the extreme case, if one supposes the heating is deposited only in the Bragg peak, i.e. inside a target layer of $2 \mu\text{m}$, the specific heat capacity of niobium is $24.6 \text{ J mol}^{-1} \text{ K}^{-1}$, one calculates that the maximal increase of the local temperature is $\approx 1.9\text{K}$. This is not sufficient to induce a transition between the superconducting phase at 4K to the metallic phase at 9.2K. The beam irradiation induces a deterioration of the target lattice which results into a change of the critical temperature of the material. Each incident ion induces thousands of vacancies and interstitials. Neumüller et al. [36] examined the dependence of the critical temperature of niobium on the irradiation induced by an oxygen beam of 25 MeV, whereby the beam was not stopped inside the target. They found that the critical temperature was decreased by 1% for irradiation of $1,3 \times 10^{16}$ ions of oxygen per cm^2 . In the present experiment, the beam intensity was around 10^5 pps and the total effective irradiation did not exceed 10^{12} ions per cm^2 per target. This is much lower than in ref. [36], and thus change of the critical temperature can be neglected.

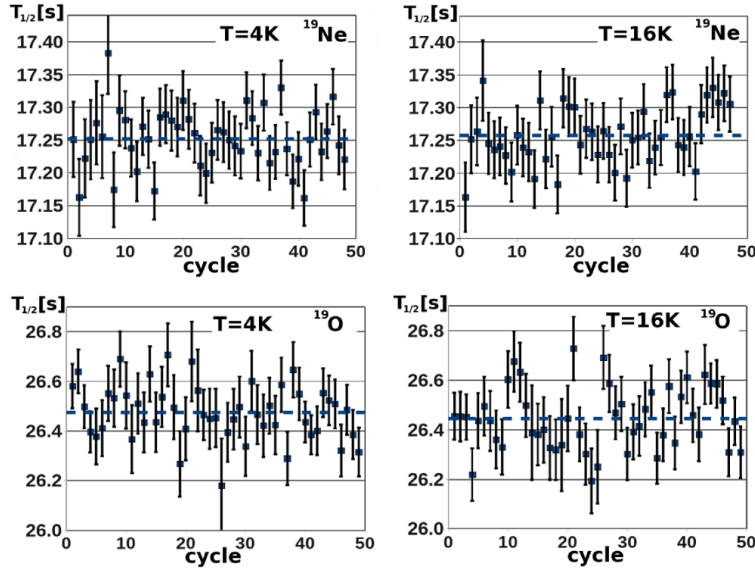


Figure 2.6: Upper two figures: measured ^{19}Ne half-life values for all cycles of measurements of the set of runs (I) (4K -16K). Lower two figures: the same for ^{19}O . The dashed lines correspond to the mean value.

2.2.2 Analysis

An example of implantation-decay curve is presented in Fig. 2.5. After each implantation, the decay curve was fitted with an exponential function of time plus a constant. For the fitting procedure, the standard Levenberg-Marquardt method [37] was used. The fitting was performed on the full decay curve. On the contrary, only a part of the decay curve was used for the measurement of BR with the Germanium detectors. In this case, the analysis started each time on the same counting rate in order to respect the same experimental conditions, especially regarding the pile-up probability. A half-life value was extracted after each implantation and the mean value of the all measured half-lives was obtained by the weighted mean method, see Fig. 2.6. This procedure was performed for each temperature and for each beam. The systematic effect due to the choice of the bin width was taken into account in the calculation of the error. Unambiguously, 11 cycles out of a total of 331 were rejected because they had $\chi^2/\nu > 1.3$. The problem was identified, it was noticed that these runs correspond to “time-out” occurrences when the acquisition was stalled for short period of time because of network congestion, with a loss of time consistency. For the other cycles, a $\chi^2/\nu = 1.04 \pm 0.10$ was obtained for ^{19}O and $\chi^2/\nu = 1.01 \pm 0.10$ for ^{19}Ne . These values are indicative of statistical consistency among the runs since the theoretically expected variation of χ^2/ν is 0.07 for ^{19}O and 0.08 for ^{19}Ne . The results for half-lives are presented in Fig. 2.7 and the results of the relative branching ratios are given in Table 2.2.

All measured half-lives and BRs are consistent within one-sigma error bar. Many checks of systematic errors were performed, including dead time effect, contamination of the beam, variation of the χ^2/ν values, average value and weighted average value consistency, change of the normalized residuals of the fits, change of the background. No systematic effect could be observed except the one produced by the binning of the spectra, which was of 0.011 %. The mean value of the measured half-lives is 26.476(9) s for ^{19}O and 17.254(5) s for ^{19}Ne . These results are in excellent agreement with previously measured

Table 2.2: Measured values of the relative branching ratios (BR) of ^{19}O in superconducting (SC) and metallic (M) phases of niobium for two sets of runs: (I) 4K and 16K, and (II) 4K and 90K.

| Phase | BR of 197/1554 | BR of 197/4377 |
|------------|-------------------|-------------------|
| SC-4K (I) | 3.611 ± 0.015 | 3000 ± 200 |
| M-16K (I) | 3.607 ± 0.015 | 2700 ± 170 |
| SC-4K (II) | 3.595 ± 0.017 | 3100 ± 200 |
| M-90K (II) | 3.582 ± 0.017 | 2800 ± 200 |

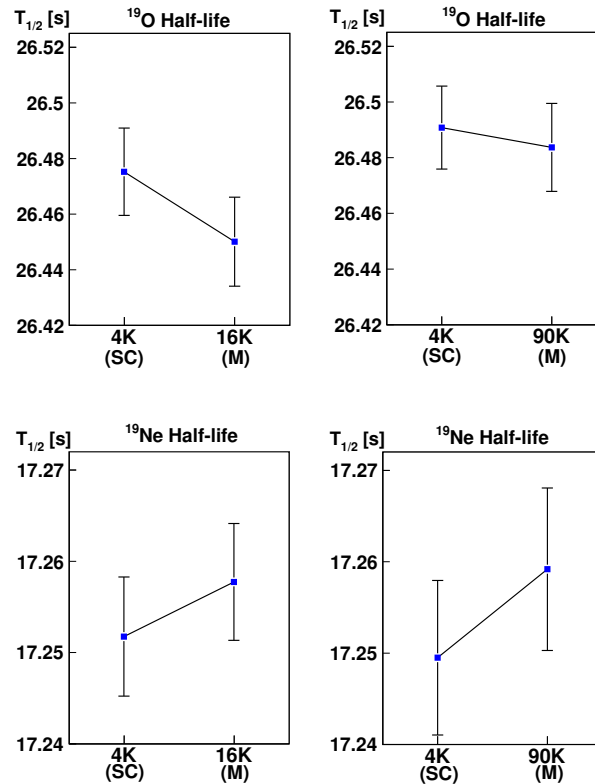


Figure 2.7: Measured half-lives of ^{19}O and ^{19}Ne implanted in niobium at different temperatures.

values of 26.464(9) s [31] and 17.262(7) s [32] respectively.

These results show that the difference in the screening effects between superconductor phase and the metallic phase is very small. It is possible to combine all these measured results in order to obtain a more sensible and statistically more accurate evaluation of the screening effect. In order to do so, these results have to be normalized. Table 2.1 was used for this purpose. For example, the measured BR 197/1554 was 3.607 at 16K and 3.611 at 4K. Thus, the measured relative change is +0.11%. According to Table 2.1, the predicted change is +0.79%. This means that $0.11/0.79=+13.9\%$ of the predicted change was measured. All the measured BRs and half-lives, both for neon and oxygen, can be combined in this manner. The average of these normalized values is $0.95 \pm 0.78\%$.

It is possible to try iteratively different values of U_e in order to match this 0.95 % effect. One obtains that

the difference in U_e between the two phases which would induce this change is 110(90) eV for ^{19}Ne and 400(320) eV for ^{19}O . These values are close to the values measured in different kinds of materials with nuclear reactions [22].

These results were mostly obtained by Dr. Predrag Ujic during his Ph. D. thesis [7] (a former student of mine) and they were presented in conferences and in the publication of Ref. [38].

2.3 Conclusion and Outlook

2.3.1 Summary

A high-precision experiment was performed in order to measure half-life and branching ratios of $^{19}\text{O}(\beta^-)$ and $^{19}\text{Ne}(\beta^+)$ implanted in a niobium foil in its superconducting and metallic phases. No difference was observed between the two phases within the limits of experimental accuracy: 0.04% for the half-life, 0.5% and 7% for the 197/1554 and 197/4377 relative branching ratios of ^{19}O . We deduced from these results that the effect of the electron screening for both nuclei in a superconductor is well below the predicted effects (see Table 2.1), so well below the predicted screening energy of ~ 20 keV in the superscreening model (Debye model), and well below the observed screening energy of ~ 1000 eV measured in some metals. The mean value of the measured half-lives is 26.476(9) s for ^{19}O and 17.254(5) s for ^{19}Ne . These are the most precise ever measured results for these nuclei, with a precision better than 0.4 per mil. An indication for a positive screening potential energy, with a mean value of $U_e=131(90)$ eV was obtained after combining all measured results. The obtained precision was not high enough allowing us to determine if this value is above the adiabatic limit or not.

The success of the Debye model explaining the first results of half-lives measured in metals was very surprising. The Debye model is correct in classical physics only, it cannot be applied to the sea of free electrons in metals. The Thomas-Fermi model predicts much lower values ($U_e \lesssim 100$ eV). After the first publications of B. Wang *et al* [27], B. Limata *et al* [28] and several others others, most of the new publications have countered the first results obtained in metals, no change of the β -decay half-life was measured.

We can summarize the situation as following:

1. The high electron-screening effect observed in metals, both in nuclear reaction cross sections at low energy and in β -decay half-life measurements, was probably an experimental artefact.
2. The electron-screening effect is not yet confirmed in the β -decay experiments. In other words, a clear measurement of different half-lives of the same nucleus in different materials is predicted but is not yet measured.
3. The electron-screening problem, measured in nuclear astrophysics reactions, is not yet solved.

2.3.2 A new High-precision experiment (E558S)

Based on our experience, an improved experimental setup dedicated to half-life measurements, using scintillators with increased efficiency and fast scalers, can be used with a much more intense and purified radioactive beams. In principle, a factor 10 in accuracy is readily accessible. A new high-precision

experiment (E658S) was proposed to the GANIL Advisory Committee, was accepted, and was performed in 2013. It was based on the extremely fast digital acquisition FASTER [39]. We tried to measure up to 1 million counts per seconds. One of the objectives is to confirm or to rule out the electron screening problem in the β -decay. The analysis of the experiment is finished and a publication is expected for beginning of 2017.

2.3.3 Outlook

We close this Chapter with three important comments.

- Firstly, it is interesting to note that recently a new idea was proposed by Spitaleri *et al* [21] in order to explain the electron screening problem [21] without questioning the "well-known" atomic physics effects. Instead of an atomic physics solution of the electron screening problem, they proposed clusterization effects in nuclear reactions. It is an already well known effect that dramatic impact of clusterization can be imprinted on the quantum tunneling probability, particularly at low energies. Whereas the spectroscopic amplitudes of cluster-like structures can be very small, fusion reactions have an exponential enhancement for cluster-like structures. It is important to test this idea with new cases, in particular with reactions between highly clusterized nuclei.
- Secondly, there is another prediction of the electron screening, which was already observed at least once in Ref. [24] but with serious doubts. If it comes from atomic physics, the electron screening should lead to a shift of resonance energies compared to the case of bare nuclei. This effect could be used to confirm the atomic physics origin of the problem and rule out the cluster model, but the effect is predicted to be extremely small, the energy of the resonance is changed by U_e .
- Within the SPIRAL2 project, there is the FISIC project which aim at studying the atomic Fast Ion Slow Ion Collisions [40]. It is clear that a better understanding of the elementary atomic collision processes will help to calculate accurately the magnetically confined plasma reactions (Tokomak) and the stellar reactions.

Origin of Fluorine

Sommaire

| | |
|--|-----------|
| 3.1 Introduction: The origin-of-fluorine problem | 25 |
| 3.2 Determination of the $^{15}\text{N}(\alpha,\gamma)^{19}\text{F}$ reaction rate | 26 |
| 3.2.1 The measurement of $^{15}\text{N}(^7\text{Li,t})^{19}\text{F}$ at Orsay | 26 |
| 3.2.2 DWBA Analysis | 26 |
| 3.2.3 Calculation of the direct-radiative-capture cross section | 31 |
| 3.2.4 The new rate of $^{15}\text{N}(\alpha,\gamma)^{19}\text{F}$ | 32 |
| 3.2.5 Astrophysical impact | 32 |
| 3.3 Conclusion and Outlook | 33 |

N'est-il pas honteux que les fanatiques aient du zèle et que les sages n'en aient pas ?

Pensées détachées de M. l'abbé de Saint-Pierre. Voltaire

3.1 Introduction: The origin-of-fluorine problem

Fluorine is a relatively rare element in the solar system with an abundance of $\approx 3 \times 10^{-6}$ % [41] in number of atoms. This element has only one stable isotope, ^{19}F , fragile and easily destroyed in stellar interiors. Thus, any production mechanism has also to enable ^{19}F to escape from the hot stellar interiors after its production. This makes fluorine a useful tracer of the physical conditions prevailing in stellar interiors. Fluorine is thought to be produced in several astrophysical sites: (i) Core-collapse supernovae through the neutrino spallation process, mostly $^{20}\text{Ne}(\nu, \nu')^{20}\text{Ne}^*(p)^{19}\text{F}$, (ii) low and intermediate mass ($M \leq 7M_{\odot}$) Asymptotic Giant Branch (AGB) stars during the He-burning Thermal Pulses and the subsequent Third Dredge Up episodes (a dredge-up is a period in the evolution of a star where a surface convection zone extends down to the layers where material has undergone nuclear fusion, the third period happens in AGB stars). As a result, the fusion products are mixed into the outer layers of the stellar atmosphere where they can appear in the spectrum of the star., (iii) Wolf-Rayet (WR) stars in the hydrostatic He-burning phase and, even, (iv) during white dwarfs mergers [42]. The relative importance of these production sites has not been established, leading to uncertainties in stellar evolution models. Currently, only for low mass AGB stars there exist direct observations of an in-situ Fluorine production [43], where up to 30 times solar abundance has been measured from the observation of infrared rotation-vibration lines of the HF molecule. Galactic Chemical Evolution model predict that AGB stars contribution peaks during the early epochs of the Galaxy's evolution and that WR contribution is significant at solar and super-solar metallicities [44], but this picture is still debated [45]. The origin-of-fluorine problem is not yet solved.

Fundamental ingredients (necessary but not sufficient condition) for these models are the nuclear reaction rates involved in the fluorine production. Both WR and AGB astrophysical sites involve the chain of thermonuclear reactions: $^{14}\text{N}(\alpha, \gamma)^{18}\text{F}(\beta^+)^{18}\text{O}(p, \alpha)^{15}\text{N}(\alpha, \gamma)^{19}\text{F}$. The rate of the last reaction: $^{15}\text{N}(\alpha, \gamma)^{19}\text{F}$ ($Q=+4014$ keV) was badly known when I started my Ph.D. thesis. Direct measurement of this reaction using intense stable beam is very difficult, and it has not yet been performed up to now. One of the big challenges was to determine the rate of this important reaction $^{15}\text{N}(\alpha, \gamma)^{19}\text{F}$.

3.2 Determination of the $^{15}\text{N}(\alpha, \gamma)^{19}\text{F}$ reaction rate

From the knowledge of the ^{19}F structure, it is possible to determine the astrophysical rate of this reaction. This was done in the CF88 compilation [46], see Fig. 3.1. We can observe that the rate of this reaction is dominated at $T_9 < 0.5$ by one resonance contribution located at $E_r=364\text{keV}$ ($E_x=4.378$ MeV). The rate of the resonance was not known in that time but it was expected to have the highest contribution in the relevant temperature range. The value used for the resonance in the CF88 compilation came from the crude estimate of an α -width equals to 10% of the Wigner limit ($\theta_\alpha^2=0.1$). As the $E_r=364\text{keV}$ resonance is narrow, isolated and its γ -width is much higher than its α -width, the reaction rate is just proportional to the α -width.

The determination of an α transfer spectroscopic factor could allow a better estimate of the α -width. We proposed to measure it using the transfer reaction $^{15}\text{N}(^7\text{Li}, t)^{19}\text{F}$ at 28 MeV. We measured the angular distributions corresponding to the first 16 levels of ^{19}F , including the level of astrophysical importance at $E_x = 4.378$ MeV, and analysed them by FR-DWBA (Finite Range Distorted Wave Born Approximation) to extract α -widths.

3.2.1 The measurement of $^{15}\text{N}(^7\text{Li}, t)^{19}\text{F}$ at Orsay

We used for this experiment a ^{15}N confined gas target enriched to 99% with a pressure close to 100 mbar. The experiment was carried out with a 28 MeV $^7\text{Li}^{+++}$ beam from the Orsay Institut de Physique Nucléaire Tandem accelerator. The reaction products were analysed by a SPLIT POLE magnetic spectrometer and detected in the focal plane by a position-sensitive drift chamber. Clear identification of the particles, as shown in Fig. 3.2, was allowed by the measurement of energy loss in a proportional counter, and remaining energy (E) with a plastic scintillator.

The intensity of the ^7Li beam was kept around 30 nA. A Si-detector, 100 μm thick, situated within the reaction chamber was used for monitoring the intensity of the elastically scattered ^7Li particles. The peaks of interest were well identified in the experimental triton spectra, see an example in Fig. 3.3, the energy resolution was ≈ 100 keV.

The level of main interest at $E_x = 4.378$ MeV is weakly populated but can be easily resolved from the group of levels at 4.55 MeV at all angles (Fig. 3.4).

3.2.2 DWBA Analysis

Many studies have shown the interest of the α -cluster modelling for the stripping reaction ($^7\text{Li}, t$). So here we reduced the four-nucleon transfer to a three-body problem ($^{15}\text{N}, \alpha, t$) where both projectile and residual nuclei have a cluster structure ($^7\text{Li} = \alpha + t$, $^{19}\text{F} = \alpha + ^{15}\text{N}$). The calculations were done with the standard approximation of the interaction V_{eff} in the "post" form. The transferred orbital momentum (L_t) is

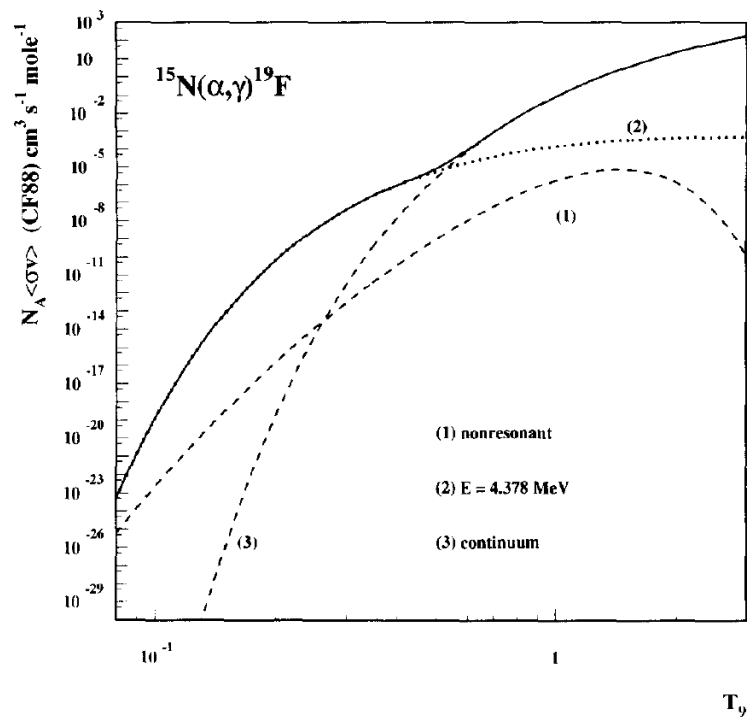


Figure 3.1: The rate of the $^{15}\text{N}(\alpha,\gamma)^{19}\text{F}$ reaction as calculated before this study in the CF88 compilation [46]. Three contributions were taken into account, including a resonance at $E_x=4.378 \text{ MeV}$. (T_9 is temperature in billion degrees)

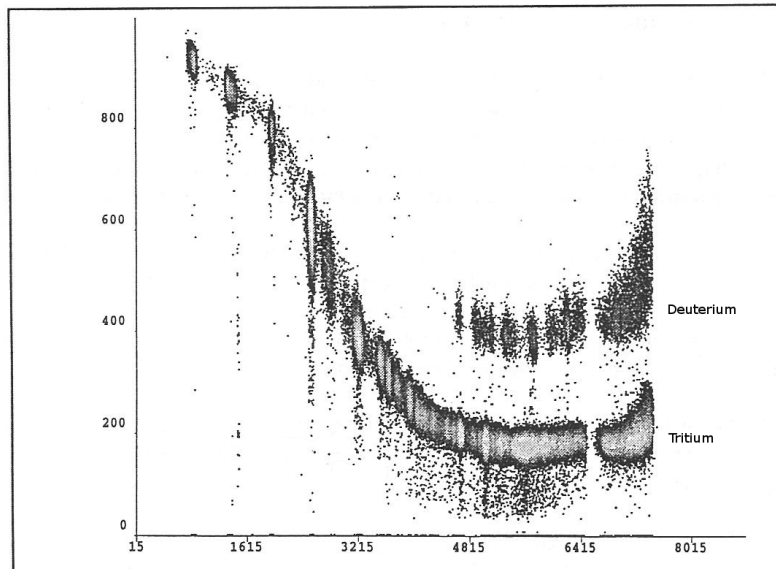


Figure 3.2: Identification plot: Position in the proportional counter versus energy E (arbitrary units). The tritium particles are well identified.

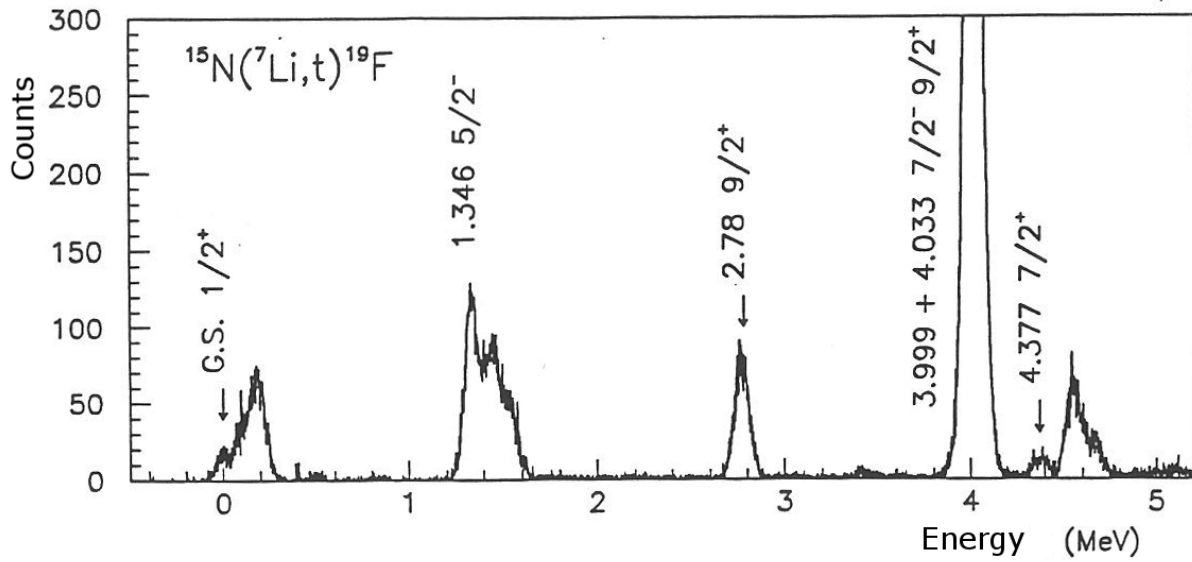


Figure 3.3: Experimental triton spectrum measured at 15° lab.

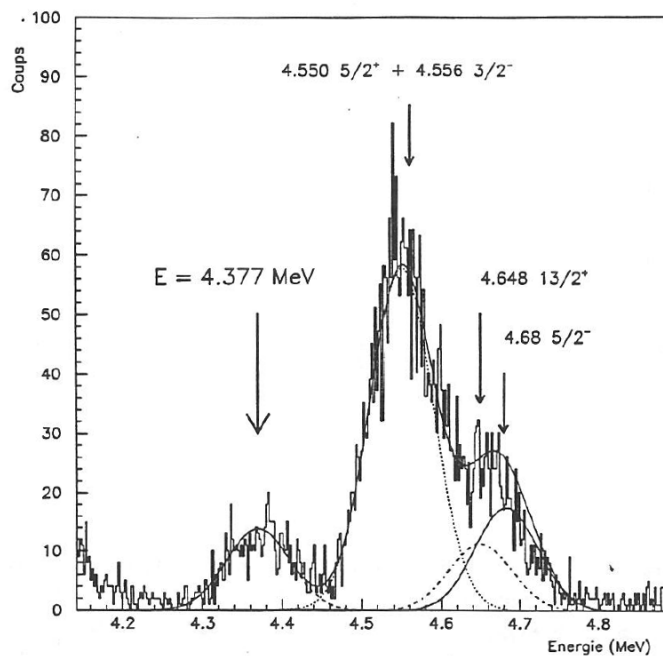


Figure 3.4: Part of the experimental spectrum measured at 15° lab. The peak of interest $E_x=4.377$ MeV is well isolated from the other peaks.

one of the parameters of the calculation. In order to calculate the wave functions in the α -cluster model, assuming a 0s motion for the four nucleons in the α ($n = l = 0$), we used the usual Talmi-Moshinsky relationship: the number N of radial nodes (origin excluded) of the α wave function for an orbital angular momentum L is fixed by the relation [47] $2N + L = Q = \sum_{i=1}^4 (2n_i + l_i)$ deduced from the harmonic oscillator shell model using the rule that the total number of oscillator quanta Q is conserved. Here n_i, l_i are the quantum numbers of the transferred particles in the shell-model levels which contribute to the cluster. It is uniquely defined once the distribution of the individual nucleons of the cluster in the orbitals of the shell model is specified. Finally, calculations of the DWBA transfer cross sections involve the combination of four elements:

- The bound-state wave function representing the composite projectile nucleus ${}^7\text{Li} = \alpha + t$ and the associated potential $V_{\alpha t}$,
- The bound-state wave function representing the composite nucleus ${}^{19}\text{F} = \alpha + {}^{15}\text{N}$ in the final state,
- The elastic scattering wave function in the incoming channel ${}^{15}\text{N}({}^7\text{Li}, {}^7\text{Li}){}^{15}\text{N}$ and
- The elastic scattering wave function in the outgoing channel ${}^{19}\text{F}(t, t){}^{19}\text{F}$

The analysis was done with the PTOLEMY code [48], but we also used the DWUCK 5 code [49] to check the consistency of the results. We also calculated the compound nuclear contribution to the cross section in the framework of the Hauser-Feshbach statistical model with a modified version of the program HSFB [50]. This HSFB contribution was added incoherently to the DWBA part of the cross section so that the calculated cross section (to be fitted to the experimental one) is given by:

$$\frac{d\sigma}{d\Omega} = SN \left(\frac{d\sigma}{d\Omega} \right)_{DWBA} + C \left(\frac{d\sigma}{d\Omega} \right)_{HSFB} \quad (3.1)$$

where C and N are normalization constants. The parameter N is the renormalization constant for the $({}^7\text{Li}, t)$ reaction. It was not known, we determined that it is in the range between 0.7 and 2.0. The parameter S is the spectroscopic factor related to the lithium and fluorine spectroscopic factor by:

$$S = S_{\alpha}({}^7\text{Li})S_{\alpha}({}^{19}\text{F}) = S_{\alpha}({}^{19}\text{F}) \quad (3.2)$$

since $S_{\alpha}({}^7\text{Li}) \approx 1$.

Experimental results are presented in Fig. 3.5 for the $E_x = 4.378$ MeV state, together with the results of our calculations. The angular distributions are rather structureless, due to the fact that several values of the transferred angular momenta L_t are mixed in the cross section. The solid line is the sum of the direct part (point-dashed line) and the HSFB contribution (dotted line). The value of the spectroscopic factor S , defined by the Equ. 3.1, is very low $S=0.012$. The calculated HSFB contribution has been renormalized by a factor $C = 0.3$ in order to obtain a compound-nucleus cross section similar to the data at large angles for the weakly populated levels. The same factor was then successfully applied to the HSFB contributions of the other levels. A very good overall agreement was observed with the data.

Stability of the results was carefully studied with respect to the various parameters entering into the calculations. The influence of the α -core potential in fluorine was found to be important for the spectroscopic

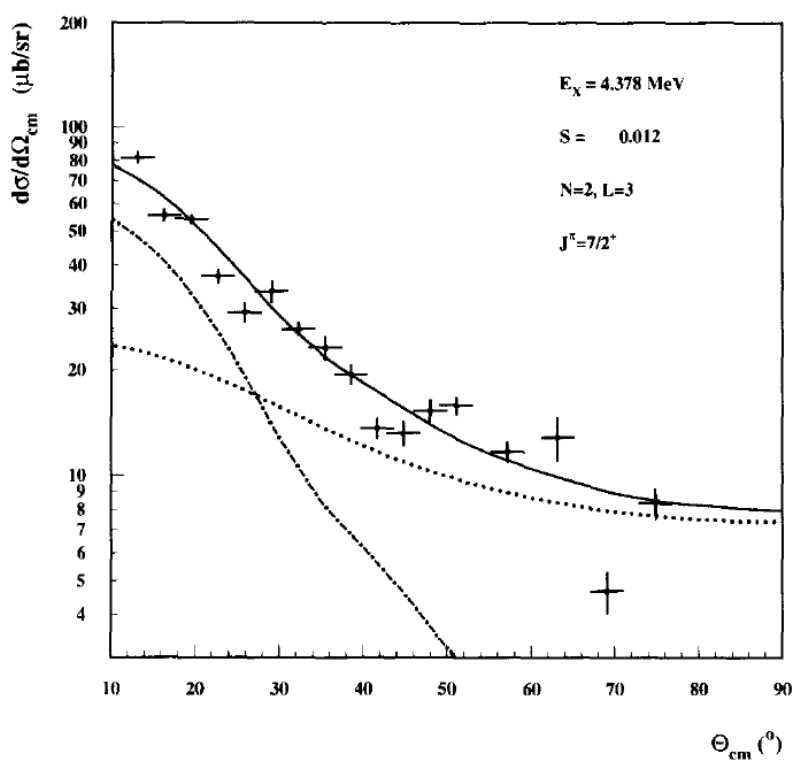


Figure 3.5: Angular distribution of the $E_x=4.378$ MeV state. The solid line is the sum of the direct part (point-dashed line) and the HSFB contribution (dotted line).

| E_x (MeV) | J^π | L | 2N+L | S_α (10^{-2}) | γ_α^2 (keV) | Θ_α^2 (10^{-2}) | Γ_α (MeV) |
|----------------|---------|---|------|-----------------------------|----------------------------|------------------------------------|--------------------------|
| 4.033 | 9/2- | 4 | 8 | 29 (5) | 109 | 13.5 | $1.2 \cdot 10^{-75}$ |
| 4.378 | 7/2+ | 3 | 7 | 1.2 ± 0.3 | 4.44 | 0.56 | $1.5 \cdot 10^{-15}$ |
| | | | 9 | 0.75 ± 0.25 | 3.73 | 0.47 | $1.25 \cdot 10^{-15}$ |
| 4.55 | 5/2+ | 3 | 7 | 9 ± 1 | 33 | 4.2 | $1.6 \cdot 10^{-11}$ |
| | | | 9 | 5.5 ± 0.5 | 27.5 | 3.5 | $1.3 \cdot 10^{-11}$ |
| 4.683 | 5/2- | 2 | 8 | 3.8 ± 0.5 | 18.7 | 2.36 | $3.0 \cdot 10^{-9}$ |
| 5.107 | 5/2+ | 3 | 7 | 0.7 ± 0.2 | 2.6 | 0.33 | $3.3 \cdot 10^{-8}$ |
| | | | 9 | 0.4 ± 0.2 | 1.98 | 0.25 | $2.5 \cdot 10^{-8}$ |

Figure 3.6: Part of the results obtained in this experiment. These correspond to the levels locate just above the α -emission threshold. The most important state is highlighted in yellow.

factors. We estimated that the corresponding overall error on the α -width is of a factor of 2. This estimated error was supported by the comparison between the present results and the α -widths obtained by direct measurements of higher lying states. Part of the results obtained in this experiment is shown in Fig. 3.6. These correspond to the levels locate just above the α -emission threshold.

The α -width of the level of astrophysical interest has been determined to be $\Gamma_\alpha = (1.5_{-0.8}^{+1.5}) \times 10^{-9}$ eV using the R-Matrix formalism. The error (a factor of two) has been estimated from the analysis of the stability of results and from the comparison between direct and indirect measurements.

3.2.3 Calculation of the direct-radiative-capture cross section

Non-resonant direct-radiative-capture reactions could be important at low temperatures (see Section 1.5). Our new experimental results were used to calculate this contribution precisely. The two γ -transitions E1 and E2 were taken into account since they are the fastest and most probable transitions. Cross-sections were calculated with the code RACAP ([51]) using the alpha cluster model and Woods-Saxon potentials where the deep of the well is fitted in order to reproduce the binding energies. Measured alpha spectroscopic factors were used to take into account the nuclear internal structures.

To illustrate this procedure, we give here the example of the ground state $^{19}\text{F}(J^\pi = \frac{1}{2}^+)$ populated by the entrance channel $^{15}\text{N}(\frac{1}{2}^-) + \alpha(0^+)$. From the angular momentum and parity conservation rules we get:

$$\frac{1}{2} + 0 + \ell = \frac{1}{2} + M \quad (3.3)$$

$$(-1)(+1)(-1)^\ell = (+1)(-1)^M \quad (3.4)$$

where ℓ is the incident orbital angular momentum and M is the order of the multipolarity of the γ -transition (limited here to 1 or 2).

If the orbital angular momentum of the entrance channel $^{15}\text{N} + \alpha$ is $\ell=0$, we get:

$$\frac{1}{2} = \frac{1}{2} + M \quad (3.5)$$

$$(-1) = (-1)^M \quad (3.6)$$

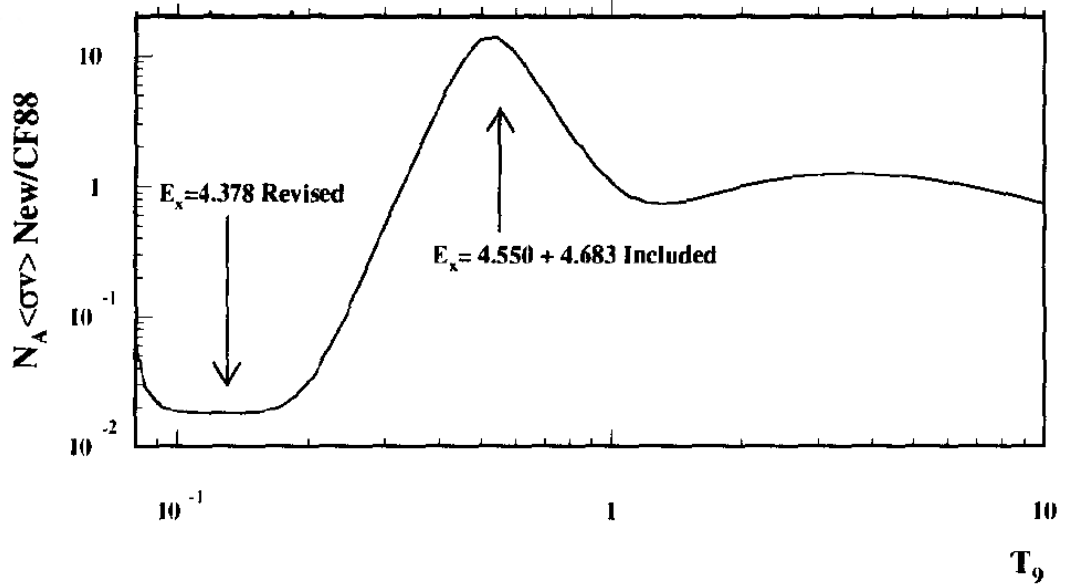


Figure 3.7: Ratio of the new reaction rate to the CF88 one. T_9 is temperature in billion degrees.

having the solution $M = 1$, it should be an E1 transition.

With the code RACAP we calculate the cross section for a E1 transition from an incident $\ell=0$ alpha particle to a final alpha cluster spinning around a ^{15}N core, and multiplied it with the measured alpha spectroscopic factor (20%). Finally we get:

$$\sigma(E)_{\rightarrow g.s.}^{(\ell=0)} \equiv \frac{0.24 \text{ MeV.barns}}{E} e^{-2\pi\eta} \quad (3.7)$$

We can do the same with $\ell=1$, we get an E2 transition and finally:

$$\sigma(E)_{\rightarrow g.s.}^{(\ell=1)} \equiv \frac{0.028 \text{ MeV.barns}}{E} e^{-2\pi\eta} \quad (3.8)$$

And so on...

3.2.4 The new rate of $^{15}\text{N}(\alpha, \gamma)^{19}\text{F}$

The measured α -widths were used to calculate the rate of the reaction $^{15}\text{N}(\alpha, \gamma)^{19}\text{F}$ (resonant contributions). The exact expression of the new total reaction rate, including resonant and non-resonant contributions, can be found in Ref. [52, 53]. The ratio of the new reaction rate to the CF88 one is presented in Fig. 3.7. The modification brought by our measurement is very important for temperatures lower than $T_9 = 0.2$, since the reaction rate is found lower by a factor of about 60.

3.2.5 Astrophysical impact

The impact of the new rate of the reaction $^{15}\text{N}(\alpha, \gamma)^{19}\text{F}$ was evaluated in two different astrophysical scenarios:

- Calculations were realized in Brussels (ULB) to estimate precisely the influence of the new rate on the production of fluorine in AGB stars, one of the main progenitors. The surface ^{19}F overabundance (roughly a factor 2 with respect to the solar system value) achieved after a given number of thermal pulses is smaller with the new reaction rate, as expected, than with the CF88 one. The difference in abundance, a factor only ≈ 0.77 , can be considered as a maximum since it is assumed that the dredge-up occurs from the first pulse on, when the difference between the new and CF88 intershell ^{19}F abundances is maximum. In fact, after some pulses all ^{15}N available in the intershell zone is converted into ^{19}F . If the dredge-up were to start occurring at a later pulse, the difference in the ^{19}F surface abundances resulting from the new and CF88 rates would be much smaller.
- Novae explosions were also considered. The simplified model of MacDonald [54] developed by A. Coc was used to calculate the fluorine production. Roughly, the calculated ^{19}F abundance could be as high as $X = 10^{-5}$ (mass fraction) for an ejected mass of $10^{-4} M_{\odot}$ and for a rate of 20 novae/year in the Galaxy during 10^{10} years, we obtain a galactic abundance of $X = 10^{-8}$, which is too low compared to the value of the solar system $X = 4.4 \times 10^{-7}$.

3.3 Conclusion and Outlook

These results about the fluorine origin were mostly obtained during my Ph.D. thesis [52]. These were presented in conferences and in the publications [53, 55]. Much more details can be found in these publications. Several comments can be formulated here about these results:

- The new rate of the reaction $^{15}\text{N}(\alpha, \gamma)^{19}\text{F}$ being lower than the former, this study has exacerbated the problem on the origin of fluorine in the Universe. This problem is not yet solved.
- There is a kind of contradiction in the study presented here. An alpha cluster model was used to describe the states in ^{19}F and to determine the alpha spectroscopic factors of the states. The state of interest, located at energy $E_x = 4.378$ MeV, is observed as a weak peak, resulting in a very low spectroscopic factor $S_{\alpha} = 0.012$. In other words, the measurement tell us that it is not an alpha cluster structure. The precision of the alpha spectroscopic factor measured in this work can be criticized, but the main message not: The state of interest has a very low alpha spectroscopic factor, lower than the value used before this study.
- Wilmes [56] presented a criticism of the results obtained in this study. They assumed the identity of the structure for the $E_x = 4.378$ MeV and the $E_x = 4.550$ MeV levels, both states being members of the same $K^{\pi} = \frac{3}{2}^{+}$ band, hence the equality of the reduced alpha widths of both states. With this assumption, they derived the value $\Gamma_{\alpha} = 2.4 \times 10^{-14}$ MeV for the state of interest, higher by one order of magnitude than our result.

The authors of both paper (Wilmes, myself and collaborators) analyzed together the reasons for these discrepancies and published their conclusions in Ref. [55]. These $K^{\pi} = \frac{3}{2}^{+}$ states are not alpha cluster states. It is too simplistic to assume equal alpha reduced widths when these are weak components of the wave functions. Furthermore, it was shown experimentally that the hypothesis of equal reduced widths within the K^{π} band agrees generally with the result only to within a factor of 10.

Wilmes presented new results in 2002 [57]. The reaction was investigated directly in the energy range between 0.6 MeV and 2.7 MeV. All the measured properties agreed very well with their known values (see Table I of this reference). The state of interest could not be measured, and our value of the alpha width was used. The astrophysical reaction rate remained unchanged.

In 2003, Fortune and Lacaze [58] discussed on the "Reliability of a strengths for weak states", analysing thoroughly four sets of α -transfer data leading to the state of interest $E_x = 4.378$ MeV. They obtained an α -width 2.4 ± 2.1 times our value. This is in reasonable agreement with ours. One of the point underlined in this study is the compound nucleus contribution to the α -transfer reaction, which cannot be neglected, resulting in some uncertainty. This contribution was taken into account in our study, and the total uncertainty, including this aspect, was evaluated to be a factor 2 on the α -width.

More general comments can be presented for the outlook:

- The present study suggests that the rate of the reaction $^{15}\text{N}(\alpha,\gamma)^{19}\text{F}$ is well known, but as it was presented hereinbefore, this is still subject of debates. Recently, a new experimental method has been proposed to determine nuclear cross sections at low energy. A paper was written about the $^{15}\text{N}(\alpha,\gamma)^{19}\text{F}$ reaction [59]: "First determination of an astrophysical cross section with a bubble chamber: The $^{15}\text{N}(\alpha,\gamma)^{19}\text{F}$ reaction". They proposed to use photodisintegration reactions and the detection of the recoils with a superheated liquid. Intense γ -ray beams, like the one at ELI-NP (Romania) [60] could be used. The new method is based on two principles: the reciprocity theorem for nuclear reactions, which relates the cross sections of forward and time-inverse nuclear processes; and the ability of a superheated liquid to induce nucleation when exposed to radiation. The main advantage of the new target-detector system is a gain in yield of six orders of magnitude over conventional gas targets due to the higher mass density of liquids. Also, the detector is practically insensitive to the γ -ray beam itself, thus allowing it to detect only the products of the nuclear reaction of interest.

Although very interesting in general, the method cannot be used for the determination of the $^{15}\text{N}(\alpha,\gamma)^{19}\text{F}$ reaction cross section! The $^{15}\text{N}(\alpha,\gamma)^{19}\text{F}$ reaction proceeds mainly through a γ -transition linking the state at $E_x = 4.378$ MeV to the excited state at $E_x = 0.197$ MeV in ^{19}F (BR=80%). The branching to the ground state is not known and is small (< 5%). Starting from the ground state of ^{19}F , the time-inverse reaction $^{19}\text{F}_{g.s.}(\gamma,\alpha)^{15}\text{N}$ is insensitive to the main component of the time-forward cross section, and cannot be used to deduce the reaction rate.

- Despite the very weak cross section, direct measurement of the $^{15}\text{N}(\alpha,\gamma)^{19}\text{F}$ reaction at low energy is reachable using several μA of stable beam. According to the counting rate calculations, the strength of the 364 keV resonance could be measured with 1 recoil/day/ μA [61]. This kind of measurement is possible at the upgraded LUNA-MV underground laboratory or, as it is scheduled, at the European Recoil Separator for Nuclear Astrophysics (ERNA) installed at the CIRCE laboratory of Caserta in Italy.
- The results obtained for $^{15}\text{N}(\alpha,\gamma)^{19}\text{F}$ were used to deduce the properties of the mirror reaction $^{15}\text{O}(\alpha,\gamma)^{19}\text{Ne}$. This is discussed in Ref. [55] and Chapter 5.

- Transfer reactions are powerful tools in nuclear astrophysics [62]. I collaborated in several studies using transfer reactions to determine the important nuclear properties. A recent example in nuclear astrophysics is the spectroscopy of ^{61}Fe via the neutron transfer reaction $^2\text{H}(^{60}\text{Fe},\text{p})^{61}\text{Fe}^*$ [63]. Three important techniques have been developed for astrophysical applications: The ADWA (Adiabatic Distorted Wave Approximation) mainly for the (d,p) transfer reaction. The ANC (Asymptotic Normalization Coefficients) method mainly for sub-Coulomb transfer reactions, and the THM (Trojan Horse Method) method for (particle,particle) (like (α ,p)) astrophysical reactions.

Nova γ -ray emission

Sommaire

| | | |
|------------|--|-----------|
| 4.1 | Introduction: The ^{19}Ne-spins problem | 37 |
| 4.2 | The inelastic scattering reaction $^{19}\text{Ne}(p,p')^{19}\text{Ne}^*$ (PH221) | 41 |
| 4.2.1 | Experimental measurement | 42 |
| 4.2.2 | Inelastic scattering spectrum | 42 |
| 4.2.3 | Spin Assignment | 44 |
| 4.2.4 | Discussion | 46 |
| 4.2.5 | Impact on novae | 46 |
| 4.3 | First direct measurement at GANIL (E561S) | 47 |
| 4.3.1 | The experiment | 47 |
| 4.3.2 | Results | 48 |
| 4.4 | Conclusion and Outlook | 50 |
| 4.4.1 | The VAMOS experiment (E641S) | 51 |
| 4.4.2 | The $^{15}\text{O}(\alpha,\alpha)^{15}\text{O}$ experiment (E442S) | 53 |
| 4.4.3 | Study of another γ -ray emitter: ^{22}Na (E710) | 55 |
| 4.4.4 | Related developments | 56 |

I am, somehow, less interested in the weight and convolutions of Einstein's brain than in the near certainty that people of equal talent have lived and died in cotton fields and sweatshops.

The Panda's Thumb. Stephen Jay Gould

4.1 Introduction: The ^{19}Ne -spins problem

Novae are quite frequent events (I observed myself one of them, see Fig. 4.1). They are nuclear explosions caused by the accretion of hydrogen onto the surface of a white dwarf star. In these events, temperatures can reach 3.5×10^8 K, allowing fast synthesis of stable and radioactive nuclei [64]. The observation of γ -rays from nova ejecta should provide a rather direct way to investigate the nucleosynthesis and matter ejection mechanism [65]. Between 2010 and 2013, high energy γ -rays (> 100 MeV) were detected in four novae with the Fermi space telescope [66], see Fig. 4.2, pointing to unexpected high-energy particle acceleration processes linked to the mass ejection. However, the detection of γ -rays in the MeV range, from nova radioactivities, has not been achieved yet. The predictions for the current

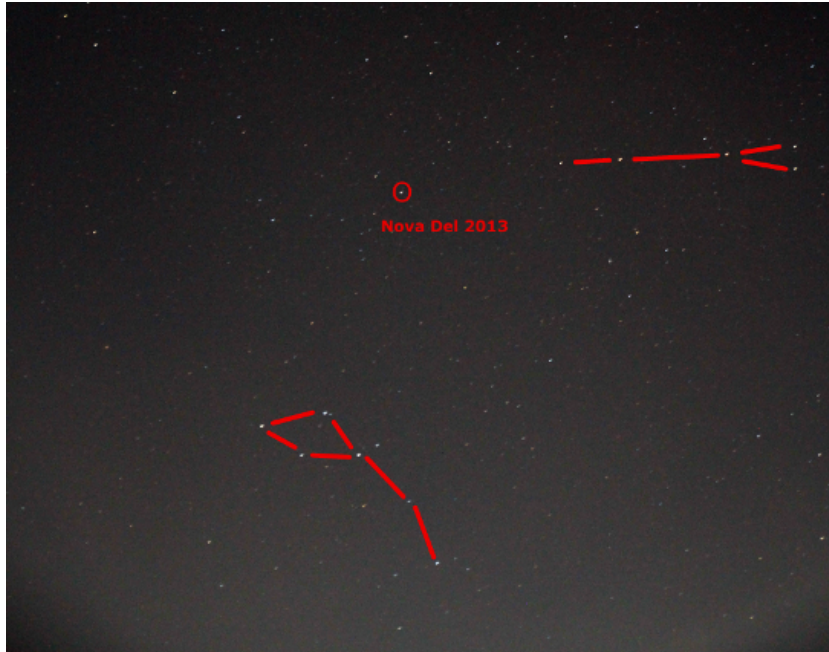


Figure 4.1: Picture of the nova Del 2013 (visible light) taken by myself in August 2013. This illustrates the fact that novae can be used for public outreach. The nova appeared close to the Dolphin and the Arrow constellations.

INTEGRAL/SPI space instrument are not very optimistic, but these depends on quite uncertain nuclear reaction rates. The most powerful γ -ray emission coming from novae is predicted to be at energies of 511 keV and below, originating from positron annihilations, see Fig. 4.3. When the nova envelope becomes transparent enough for γ -rays to escape, the main contribution to positron production is the long-lived ^{18}F radioactive nucleus (half-life 109.77 min). Therefore, the amount of radiation emitted scales with the ^{18}F content of the nova ejecta, which in turn depends strongly on its production and destruction rates.

The $^{18}\text{F}(p,\alpha)^{15}\text{O}$ reaction is the less known and the most sensitive reaction for the abundance of ^{18}F [68]. Despite a lot of experimental efforts [69, 70, 71, 72, 73, 74, 75], uncertainties remain in the determination of the rate of this reaction at novae temperatures. Direct measurement of the cross section at low energy has been made several times. Figure 4.4 shows the cross sections measured at the lowest energies, and a fit of the data. The last points measured at the lowest energies are located in the right side of the Gamow window. To measure the full range of the Gamow window, more intense ^{18}F radioactive beams are needed, as shown in the Fig. 4.5, but these intensities are not yet available [76].

In principle it is possible to calculate the cross section of the $^{18}\text{F}(p,\alpha)^{15}\text{O}$ reaction at low energy from the known properties of the compound nucleus ^{19}Ne . Several reviews of the ^{19}Ne level properties have been achieved, see for example Ref. [70, 77], but one of the main problems is that most of the spins have not been firmly assigned. From the fact that mirror nuclei have identical levels schemes, most of the spins of the states above the proton emission threshold were deduced from the mirror nucleus. This procedure is not always sure, there could be some energy shifts up or down between the mirror partners, making the spin assignment uncertain when the density of states is relatively high. That is the case of the states above the proton threshold in ^{19}Ne . A piece of evidence for a problem in the spin assignment

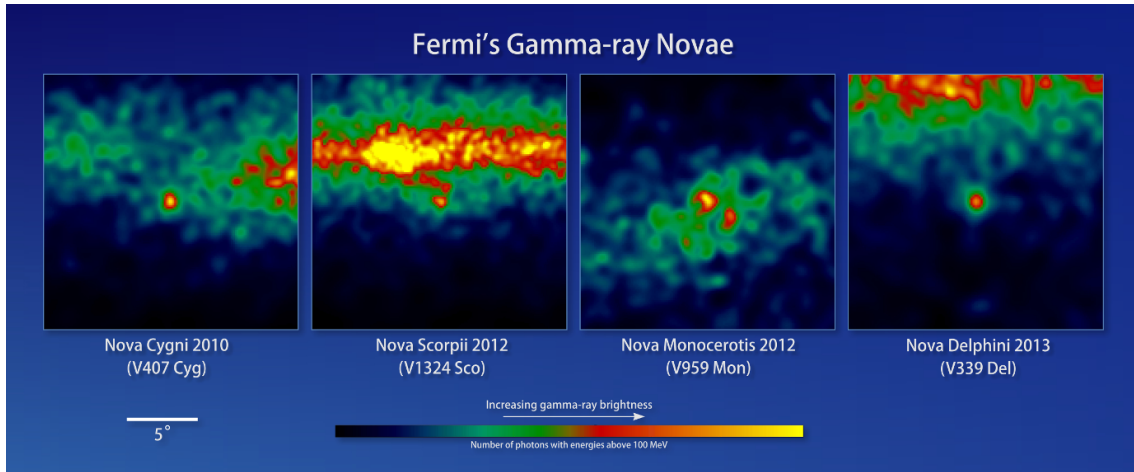


Figure 4.2: Pictures of novae taken from the Fermi telescope in the $E > 100$ MeV γ -ray energy range. Credits: NASA/DOE/Fermi LAT Collaboration

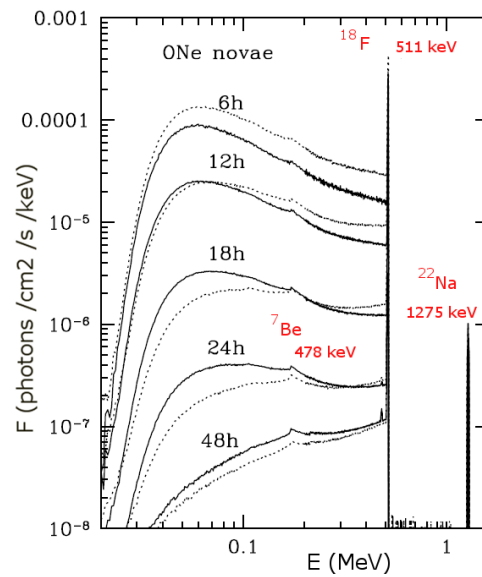


Figure 4.3: Predicted γ -ray spectra of ONe novae of masses $1.15 M_{\odot}$ (solid) and $1.25 M_{\odot}$ (dotted) at different epochs after T_{peak} . The 478 keV and 1275 keV lines are produced from the decay of ^7Be and ^{22}Na nuclei. Predictions by Hernanz [67].

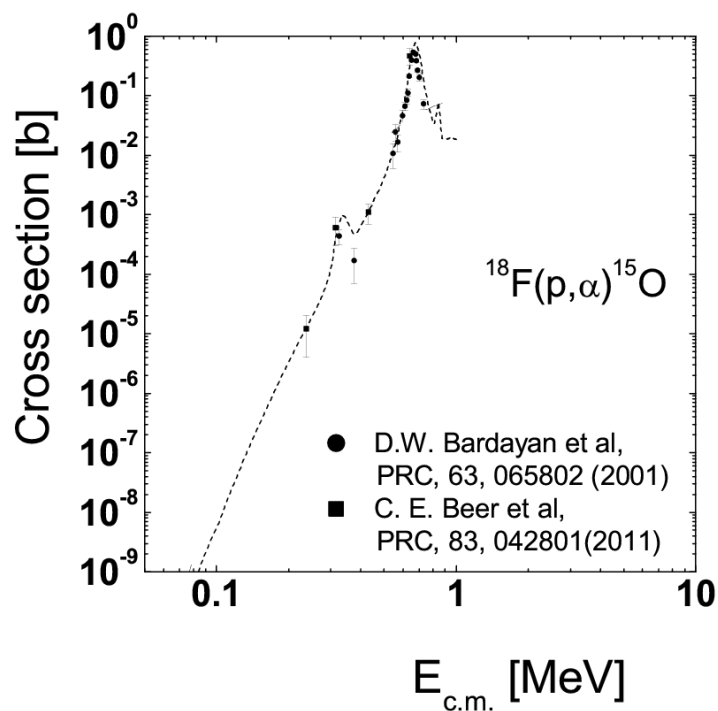


Figure 4.4: Measured cross section of the $^{18}\text{F}(p,\alpha)^{15}\text{O}$ reaction, and a fit of the data [76].

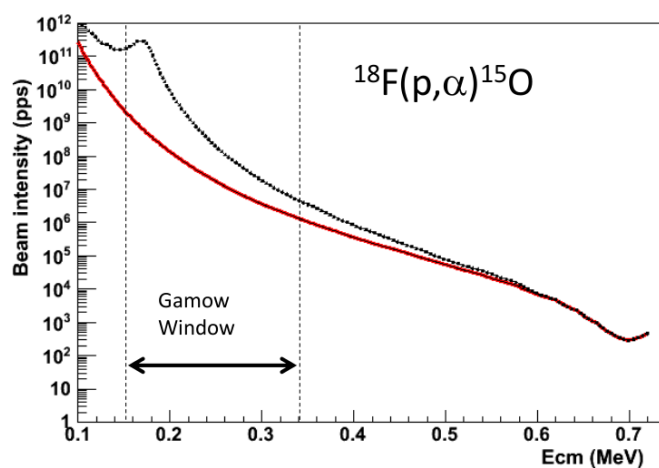


Figure 4.5: Beam intensities needed for a direct measurement of the $^{18}\text{F}(p,\alpha)^{15}\text{O}$ reaction cross section (in order to get 10 counts/day). The two lines correspond to two different realistic predictions.

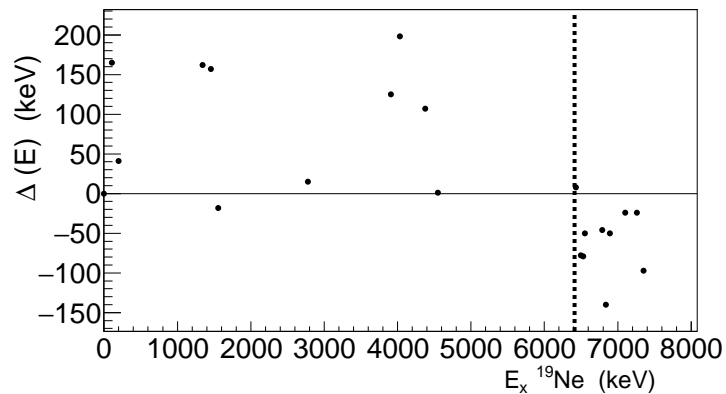


Figure 4.6: The energy shifts between the mirror states in $^{19}\text{Ne} / ^{19}\text{F}$ are shown as a function of the excitation energy of ^{19}Ne . The dotted line correspond to the proton emission threshold.

of the states can be observed in Fig. 4.6. The energy shift between the mirror analog states is shown as a function of the excitation energy in ^{19}Ne . This energy shift, the Coulomb displacement energy, should be a constant as shown in many examples in the Ref. [78]. But in the case of ^{19}Ne , in Fig. 4.6 we can clearly see that above the proton emission threshold the shift is mainly negative (mean value = -53 keV) whereas it is positive below the threshold (mean value = +92 keV). This is very surprising.

In 2007, Marianne Dufour and Pierre Descouvemont [79] predicted the existence of two not-yet-observed $\frac{1}{2}^+$ states, one at 0.41 MeV below the proton emission threshold S_p , and a second broad resonance at about 1.49 MeV above the threshold. If the existence and properties of these $\frac{1}{2}^+$ states were confirmed, the reaction rate at typical novae temperatures would be dominated by reactions through these $\ell=0$ states. Maybe, these states were already known, but with the wrong spin assignment. The ^{19}Ne -spins problem was the main objective of our study.

4.2 The inelastic scattering reaction $^{19}\text{Ne}(p,p')^{19}\text{Ne}^*$ (PH221)

Since many experiments had been performed with "traditional techniques" (transfer, direct measurement, resonant elastic scattering) in order to study the properties of ^{19}Ne , and since they could not determine the spin of all these important states, we proposed a new experimental approach to achieve this objective. We proposed to perform the measurement of the inelastic scattering reaction $^1\text{H}(^{19}\text{Ne},p')^{19}\text{Ne}^*(p'')^{18}\text{F}$. This idea came naturally after the ^{19}Na experiment (see Chapter 6) when it was realized that inelastic scattering reactions could be a very efficient way to populate particle-unbound states and to measure the angular distributions of the emitted particles. In fact, the general principle of the experiment was described in the Feynman lectures [80] on quantum mechanics (with the case of the $^{12}\text{C}+^{12}\text{C}$ reaction). In the decay of the $^{19}\text{Ne}^*$ excited states, the angular distribution of the emitted particles (above particle emission thresholds) should follow simple rules that can be used to determine, in a model-independent way, the spin of the states.

4.2.1 Experimental measurement

The experiment was performed at the Centre de Recherches du Cyclotron at Louvain-la-Neuve (Belgium) using the very intense $^{19}\text{Ne}^{6+}$ radioactive beam. The ^{19}Ne beam was produced with a mean intensity of $\approx 8 \times 10^7$ pps and accelerated to 9 MeV/u. The beam was incident on a $3.5 \mu\text{m}$ thick polypropylene target during 100 hours. No deterioration of the target was observed during the experiment. The beam intensity was monitored in a beam catcher in which it was stopped. With an upper limit of 1%, no contamination of the beam by ^{19}F was observed. A dedicated setting used a ^{19}F beam under similar conditions to calibrate the target and beam catcher thicknesses as well as the energies of the detectors using the inelastic scattering reaction $^1\text{H}(^{19}\text{F},\text{p}')^{19}\text{F}^*(\alpha)^{15}\text{N}$.

Excited states in ^{19}Ne were populated by inelastic scattering reactions $^1\text{H}(^{19}\text{Ne},\text{p}')^{19}\text{Ne}^*$ occurring in the target. Scattered protons p' were detected at zero degree by a $\Delta E - E$ telescope of silicon detectors located 50 cm downstream of the target, see Fig. 4.7. The telescope was composed of a $500 \mu\text{m}$ ΔE detector (18 keV FWHM resolution) and a 6 mm Si(Li) E detector (28 keV FWHM) cooled to -25°C , and covered a solid angle of 5 msr. We chose to detect scattered protons at 0° for three reasons: First, the best energy resolution for the excited states in $^{19}\text{Ne}^*$ is obtained for this angle as the reaction is made in inverse kinematics. Second, due to the axial symmetry of this experimental configuration, the analysis of the proton-proton angular correlation is simplified. Third, a strong alignment of the populated states in ^{19}Ne [81] is expected when the scattered proton is measured in coincidence at zero degree, resulting in a pronounced spin-dependent angular distribution of their particle decays. A $250 \mu\text{m}$ -thick aluminium foil, placed between the target and the telescope, was used as a beam catcher. The intense radioactive beam was stopped inside this catcher while the scattered protons lost less than 20% of their energy when passing through it.

The states located above the particle emission thresholds ($S_p = 6.411$ MeV and $S_\alpha = 3.529$ MeV) decay mostly by particle emission. These particles, α -particles or protons, were measured with a telescope of annular stripped silicon detectors (CD-PAD). This telescope was positioned between the target and the beam catcher, 10 cm downstream of the target. It covered laboratory angles between 4.3° and 21.6° .

4.2.2 Inelastic scattering spectrum

The excitation energies spectrum produced in the inelastic scattering reaction $^1\text{H}(^{19}\text{Ne},\text{p}')^{19}\text{Ne}^*$ was derived from the energies of the proton p' detected at zero degree. The requirement of another proton detected in coincidence in the CD-PAD detector (from $^{19}\text{Ne}^*(\text{p}'')^{18}\text{F}$) was used to suppress the background induced by reactions of the beam in the catcher. The corresponding differential cross section is presented as a function of the $^{19}\text{Ne}^*$ excitation energy in Fig.4.8.

The energy resolution in excitation energy of ^{19}Ne was measured to be 30 keV FWHM. This spectrum was analyzed with a multiple peak-fitting program. A minimum of 6 states (labeled A to E) is required to fit the proton spectrum within the excitation energy range $\approx 6.9 - 8.4$ MeV. Their properties are reported in Table 4.1. These peaks correspond to excited states in ^{19}Ne having a large branching ratio ($> 10\%$) for proton emission. Gaussian shapes were used for all peaks, except for the broad resonance (labeled E in Fig.4.8) at ≈ 7.9 MeV for which an energy dependent Breit-Wigner shape [82] was used instead.

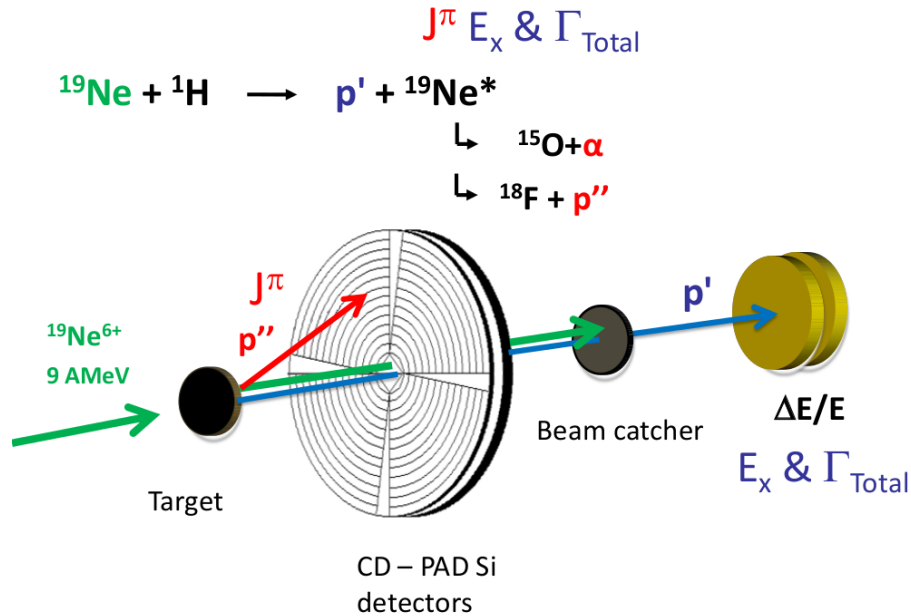


Figure 4.7: Drawing of the experimental setup used to measure the $^1\text{H}(^{19}\text{Ne},p')^{19}\text{Ne}^*(\alpha)^{15}\text{O}$ reaction.

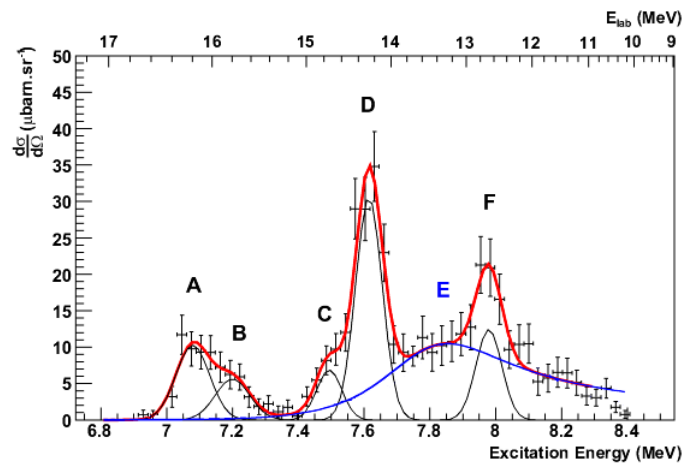


Figure 4.8: The measured differential cross section for the $^1\text{H}(^{19}\text{Ne},p')^{19}\text{Ne}^*$ reaction, with the associated proton p' detected at zero degree, is presented as a function of the $^{19}\text{Ne}^*$ excitation energy (lower axis) and the measured energy in the laboratory (upper axis) corrected for energy losses in the beam catcher. This figure was obtained in coincidence with the detection of another proton in CD-PAD detectors coming from the emission channel $^{19}\text{Ne}^*(p'')^{18}\text{F}$. Gaussian-shaped peaks were used to fit five of the observed peaks. The broad peak E was fitted with a Breit-Wigner shape using an energy-dependent proton width.

Table 4.1: Properties of the ^{19}Ne excited states measured in the present experiment are compared to results from previous measurements.

| Label | This experiment | | | | Previous measurements | | | |
|-------|-------------------|-------------------|----------------------|---------------------|-----------------------|----------------------|-------------------|------|
| | $E_r(\text{keV})$ | $E_x(\text{MeV})$ | $\Gamma(\text{keV})$ | J^π | $E_x(\text{MeV})$ | $\Gamma(\text{keV})$ | J^π | ref |
| A | 669(5) | 7.079(5) | 32(8) | $\frac{3}{2}^{(+)}$ | 7.075(1.6) | 39(2.2) | $\frac{3}{2}^{+}$ | [72] |
| B | 793(31) | 7.203(31) | 35(12) | $\frac{3}{2}^{(+)}$ | 7.173(5) | - | - | [70] |
| | | | | | 7.238(6) | - | - | [70] |
| C | 1092(30) | 7.502(30) | 17(7) | $\frac{5}{2}^{(-)}$ | 7.500(9) | 16(16) | - | [70] |
| | | | | | 7.531(11) | 31(16) | - | [70] |
| D | 1206(5) | 7.616(5) | 21(10) | $\frac{3}{2}^{(+)}$ | 7.608(11) | 45(16) | $\frac{3}{2}^{+}$ | [83] |
| | | | | | 7.644(12) | 43(16) | - | [70] |
| E | 1452(39) | 7.863(39) | 292(107) | $\frac{1}{2}^{(+)}$ | - | - | - | |
| F | 1564(10) | 7.974(10) | 11(8) | $(\frac{5}{2}^{-})$ | 7.944(15) | - | - | [84] |
| | | | | | 8.069(12) | - | - | [84] |

4.2.3 Spin Assignment

Angular distributions of the protons p^n , produced in the reaction $^1\text{H}(^{19}\text{Ne}, p)^{19}\text{Ne}^*(p^n)^{18}\text{F}$, were derived from the annular strips of the CD-PAD detectors. As the scattered protons p' were detected at 0° , the excited states in $^{19}\text{Ne}^*$ were expected to be nearly totally aligned [81]. We measured that the distribution of the magnetic substates population $P(m)$ is maximum for $P(|m| = \frac{1}{2}) \approx 0.9$, see Fig. 4.9. The incident

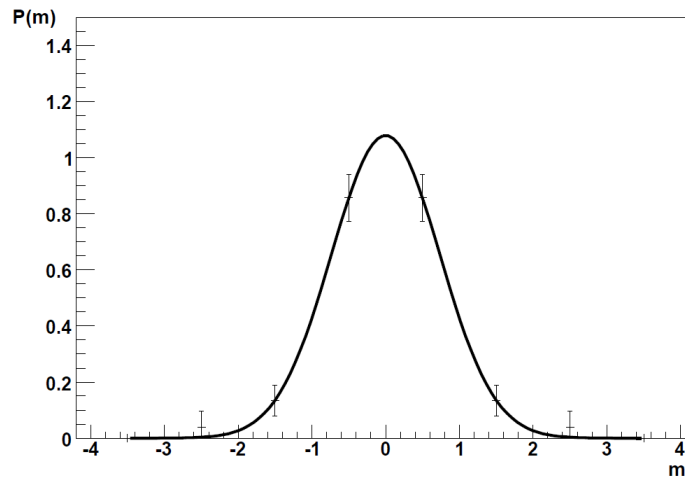


Figure 4.9: Measured distribution of the magnetic substates population $P(m)$ as a function of m . The inelastic scattering reaction measured at 0° produced strongly aligned states.

particle brings angular momentum which is perpendicular to the beam axis. If the reaction mechanism is

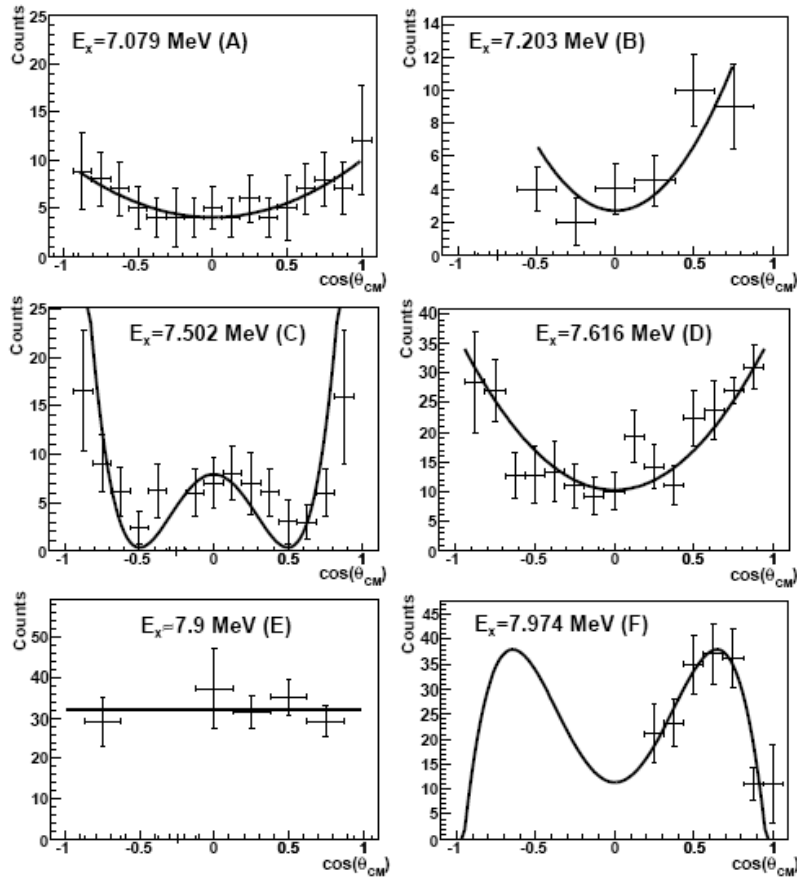


Figure 4.10: Center-of-mass angular distributions measured for each excited state in $^{19}\text{Ne}^*$. Lines correspond to the best fits obtained in the present analysis. Part of the angular distribution of levels E and F was beyond the angular coverage of the detectors.

mainly the compound nucleus, the incident angular momentum is transferred to the compound nucleus. Consequently, pronounced angular distributions were observed for the 6 peaks, see Fig. 4.10, depending on the spin of the intermediate states in $^{19}\text{Ne}^*$.

Angular-correlation analysis was used to assign the spin of the emitting states in ^{19}Ne by following the general method outlined by Pronko and Lindgren [85]. Note that it is analogous to the collinear γ -ray angular correlation method of Ferguson [81]. As described in [81, 85, 86], the angular distribution should be of the form $\frac{d\sigma(\theta_{CM})}{d\Omega} = \sum_{k=even} A_k P_k(\cos(\theta_{CM}))$, where P_k are Legendre polynomials. Then, in the present case it would be isotropic for the spin $J = \frac{1}{2}$ state, parabolic for $J = \frac{3}{2}$, biquadratic for $J = \frac{5}{2}$ and so on. As stated in Ref. [85] the angular distributions are parity independent, meaning that the parity of the observed states could not be inferred from this sole information. However, the most likely parity value can be derived from the following property. The proton-unbound states observed here have large proton widths. These states therefore emit protons with the lowest possible angular momentum value, for which the centrifugal barrier is the smallest. Based on this fact and on the ground state spin value 1^+ of ^{18}F , a

parity value (+) is derived for the $^{19}\text{Ne}^*$ spins $J = \frac{1}{2}, J = \frac{3}{2}, J = \frac{7}{2} \dots$ and (-) for spins $J = \frac{5}{2}, J = \frac{9}{2}$ etc. The measured spins and favored parity values are presented in Table 4.1.

4.2.4 Discussion

Energies, widths and spin values of the known states A and D in ^{19}Ne are remarkably reproduced by the present work, which demonstrates the reliability of the experimental method. For example, the first state labeled A is found at an excitation energy of $E_x = 7.079(5)$ MeV and a width $\Gamma = 32(8)$ keV, to be compared to $E_x = 7075(1.6)$ keV and $\Gamma = 39(2.2)$ keV [72, 77]. The angular distribution of the corresponding protons can be fitted with a polynomial of order 2 (see Fig. 4.10), leading to $J = \frac{3}{2}$ and a favored (+) parity, which is in accordance with $J^\pi = \frac{3}{2}^+$ obtained in Refs. [72, 77]. In addition to a good energy and width matching for the states B, C, and F, their spin assignments are deduced for the first time.

The 7.5 to 8.4 MeV region in Fig. 4.8 cannot be fitted without introducing at least one broad state. The analysis of the spectrum using a Breit-Wigner shaped peak gives an energy $E_x = 7.863(39)$ MeV and a total width $\Gamma = 292(107)$ keV. The angular distribution corresponding to this peak (labeled as E in Fig. 4.10) is flat, meaning that its spin value is $J = \frac{1}{2}^{(+)}$. This state is observed for the first time. Excellent agreement is found with the predictions of Ref. [79] which proposed the existence of a broad $1/2^+$ state at $E_x = 7.901$ MeV with $\Gamma = 296$ keV.

To ensure that this broad peak (E) does not originate from parasitic reaction-induced background, several checks have been made: (i) Proton energies and relative angles measured for this broad peak follow the expected kinematics relationship of the $\text{H}(^{19}\text{Ne}, p)^{19}\text{Ne}^*(p)^{18}\text{F}$ reaction, as well as the other peaks. Such correlations do not hold true for other possible reactions as $\text{H}(^{19}\text{Ne}, p)^{19}\text{Ne}^*(p)^{18}\text{F}^*$ reaction or carbon-induced fusion-evaporation reactions from the $(\text{CH}_2)_n$ target. (ii) Random proton coincidences were generated by taking the proton parameters of two distinct events. The resulting background on the differential cross section is flat over the studied energy range, and amounts to less than $\approx 10\%$ of the peak height. (iii) A combination of more than one resonance, instead of a broad one, is unlikely as they should all exhibit the same angular distribution. Moreover when using several peaks to fit the data, the agreement is not improved. (iv) Finally no state was so far observed in this energy domain [77]. The presence of one broad resonance is therefore the only plausible interpretation to explain the excitation energy spectrum around 7.8 MeV. The second $1/2^+$ state, predicted in Ref. [79] to be below the proton threshold, was not observed in this experiment.

4.2.5 Impact on novae

The astrophysical factor $S(E)$ for the $^{18}\text{F}(p, \alpha)^{15}\text{O}$ reaction is presented in Fig. 4.11 as a function of the center-of-mass energy. The first three $\frac{3}{2}^+$ states above the proton emission threshold lead to four distinct interference possibilities which are indicated by different continuous lines. In the range of interest corresponding to novae explosions, the S factor varies by more than three orders of magnitude, from $< 10^2$ to 10^5 KeV·b. The contribution of the new broad s state is superposed in this figure. Even if located far away from the proton emission threshold, the low energy tail of this resonance contributes significantly to the $S(E)$ factor at novae temperatures. It becomes the dominant contribution in the case of destructive interferences between the $3/2^+$ states. It brings so far the stringent lower limit of $S(E)$.

These results, and other results not shown here, for many states in ^{19}F and ^{19}Ne , including new spins

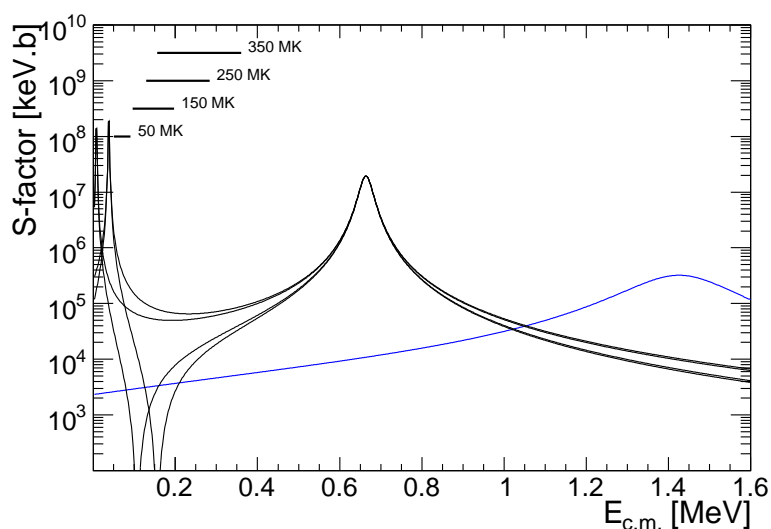


Figure 4.11: The astrophysical S -factor of the $^{18}\text{F}(p, \alpha)^{15}\text{O}$ reaction is plotted as a function of the center-of-mass energy. The corresponding nova temperatures are indicated by upper marks in the top left corner of the figure. Possible interference patterns of the three known $\frac{3}{2}^+$ states are shown [79]. The contribution of the new s -wave state is superimposed in this figure. In the range of interest this state could become the major contribution to the S -factor.

assignments, were obtained mostly by Dr. Jean-Christophe Dalouzy during his Ph.D. thesis [87] (a former student of mine), and they were presented in conferences and in the publication Ref. [88].

4.3 First direct measurement at GANIL (E561S)

Although the existence of the $\frac{1}{2}^+$ state was predicted theoretically, the observation for the first time in 2009 at GANIL of this broad resonance was questioned. Indeed, the same year a direct measurement [89] of the cross section performed at the TRIUMF facility by A. Murphy *et al* using the thick target method revealed no such feature, though a narrow state of different spin was observed in the vicinity. This measurement only took data up to $E_{c.m.} \sim 1.6$ MeV, hence the assignment of parameters to this state was hampered by its vicinity to this high energy cutoff. The two groups, the TRIUMF and the GANIL collaborations, joined in a new project. A new experiment was proposed and carried out at the GANIL-SPIRAL facility in April 2010 with the objective to confirm or reject the existence of this new state.

4.3.1 The experiment

A schematic diagram of the experimental set up used is shown in Fig. 4.12.

A 95 MeV/nucleon primary beam of ^{20}Ne bombarded a thick carbon target. Secondary ^{18}F ions were extracted in the molecular form HF, ionized in an ECR ion source, and postaccelerated with the CIME cyclotron to form a secondary radioactive ion beam of energy 3.924 MeV/nucleon. The typical ^{18}F intensity was 2×10^4 pps. The beam optics were tuned to deliver ions of mass-to-charge ratio equal to 2, i.e., a 9^+

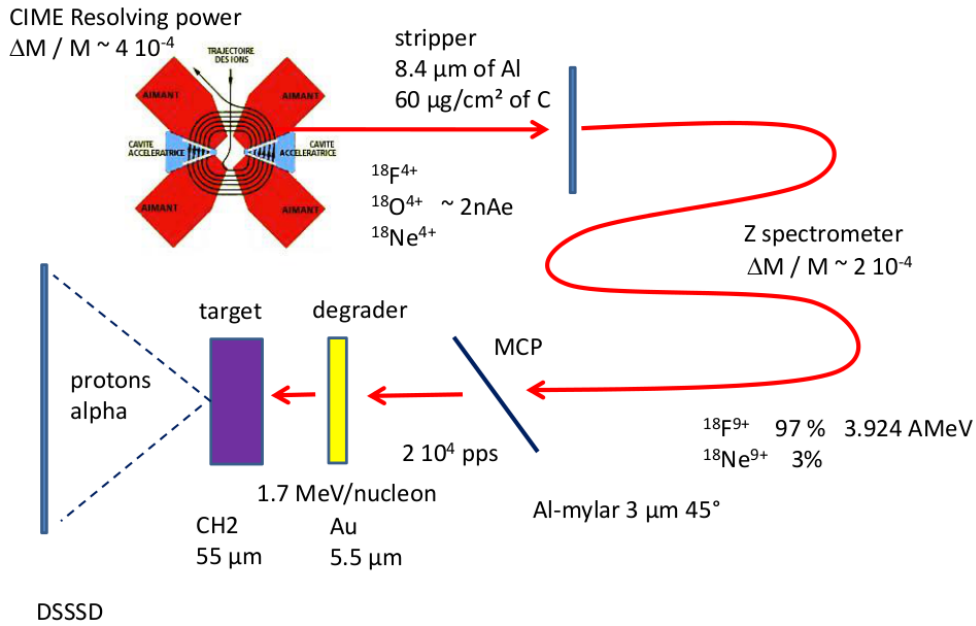


Figure 4.12: Schematic diagram of the E561S experimental set up.

charge state for ^{18}F ions. This was achieved through use of a thin carbon stripper-foil placed in the beam line after the CIME cyclotron and was motivated by the desire to eliminate contamination with ^{18}O ions. The beam was found to be contaminated with $\sim 3\%$ ^{18}Ne , thus contributing negligibly to the results.

A gold foil of $5.5 \pm 0.3 \mu\text{m}$ was mounted on the upstream face of the target, degrading the ^{18}F beam to an energy of 1.7 MeV/nucleon. The target then consisted of $55 \pm 4 \mu\text{m}$ of low density CH₂ polymer, thick enough to stop the beam, but thin enough to allow light ions to escape. Protons and alpha particles, emitted from $^{18}\text{F}(p,p)^{18}\text{F}$ and $^{18}\text{F}(p,\alpha)^{15}\text{O}$ reactions in the target, were detected in a 50 mm \times 50 mm double sided silicon strip detector.

For a thick-target experiment, the detected energy and angle of a particle (proton or α) is uniquely related to the center-of-mass energy of the scattering/reaction. By consideration of all possible target depths at which reactions might occur and angles to which particles might be detected, an angle-dependent algorithm was generated mapping laboratory energy to center-of-mass energy. Energy losses in the degrader, the target and in detector dead layers were taken into account. The algorithm was then applied to each event to generate center-of-mass energy spectra for the $^{18}\text{F}(p,p)^{18}\text{F}$ and $^{18}\text{F}(p,\alpha)^{15}\text{O}$ reactions. The resulting spectra are presented in Fig. 4.13.

4.3.2 Results

Data from all scattering angles were included in Fig. 4.13 as the limited number of events precluded projection of angular distributions. Furthermore, despite the good intrinsic energy resolution, the limited statistics have required that the spectra are binned at 25 keV (c.m.). Several resonant structures are observed of which the most prominent is that at 665 keV, due to the well known $E_x=7075 \text{ keV } J^\pi = \frac{3}{2}^+$ state in ^{19}Ne (state labeled A in Table 4.1). The observed proton and alpha widths of this peak matches

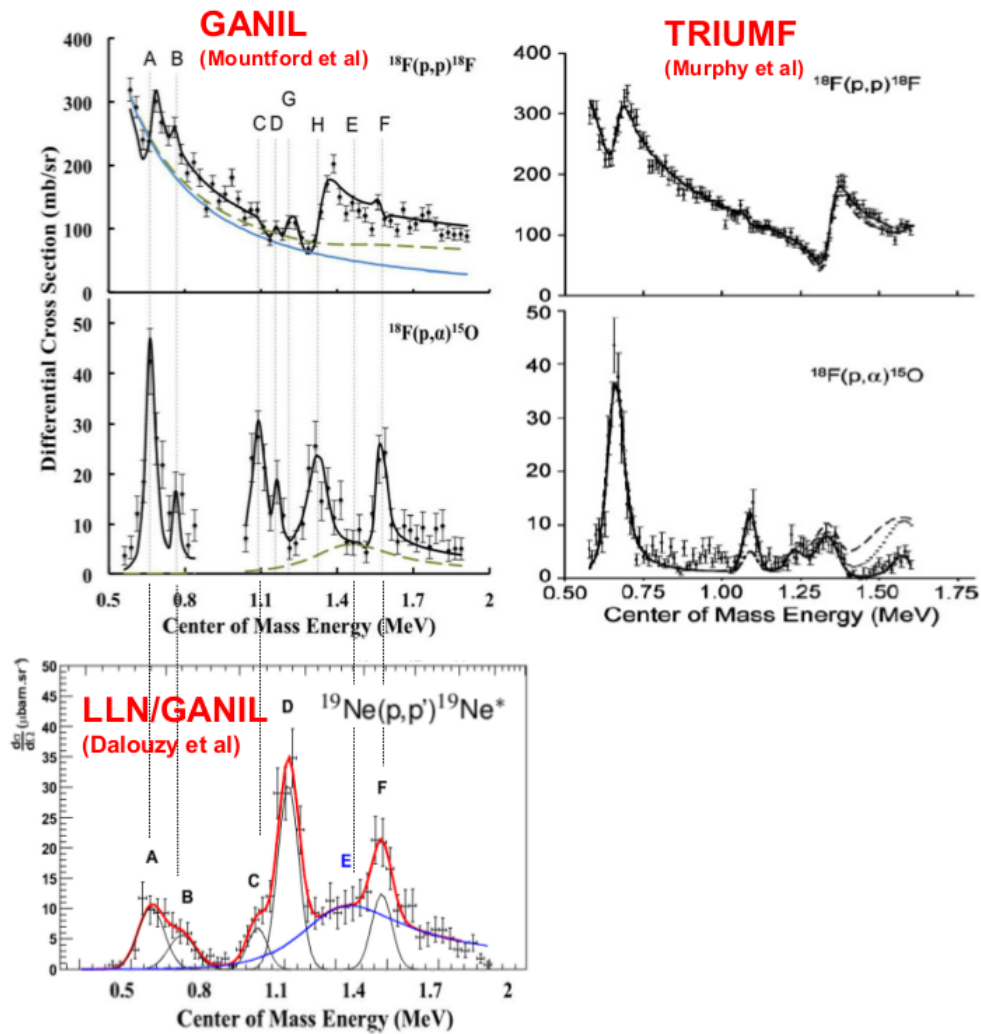


Figure 4.13: Excitation functions measured at GANIL (top left) [90], at TRIUMF (top right) [89] and Louvain-La-Neuve/GANIL [88]. The labels are the same as in Fig. 4.8. The new broad resonance observed in the LLN/GANIL (bottom) experiment is confirmed in the GANIL experiment (green and blue lines).

Table 4.2: Properties of the ^{19}Ne excited states measured in the second GANIL experiment are compared to results obtained in the LLN/GANIL experiment.

| Label | First experiment | | | Second experiment | | | |
|-------|-------------------|----------------------|---------------------|-------------------|------------------------|-----------------------------|-------------------|
| | $E_r(\text{keV})$ | $\Gamma(\text{keV})$ | J^π | $E_r(\text{MeV})$ | $\Gamma_p(\text{keV})$ | $\Gamma_\alpha(\text{keV})$ | J^π |
| A | 669(5) | 32(8) | $\frac{3}{2}^{(+)}$ | 665 | 15.2 | 23.8 | $\frac{3}{2}^{+}$ |
| B | 793(31) | 35(12) | $\frac{3}{2}^{(+)}$ | 759(20) | 1.6(5) | 2.4(6) | $\frac{3}{2}^{+}$ |
| C | 1092(30) | 17(7) | $\frac{5}{2}^{(-)}$ | 1096(11) | 3(1) | 54(12) | $\frac{5}{2}^{+}$ |
| D | 1206(5) | 21(10) | $\frac{3}{2}^{(+)}$ | 1160(34) | 2.3(6) | 1.9(6) | $\frac{3}{2}^{+}$ |
| E | 1452(39) | 292(107) | $\frac{1}{2}^{(+)}$ | 1455(38) | 55(12) | 347(92) | $\frac{1}{2}^{+}$ |
| F | 1564(10) | 11(8) | $(\frac{5}{2}^{-})$ | 1571(13) | 1.7(4) | 12(3) | $\frac{5}{2}^{+}$ |
| G | - | - | - | 1219(22) | 21(3) | 0.1(1) | $\frac{3}{2}^{-}$ |
| H | - | - | - | 1335(6) | 65(8) | 26(4) | $\frac{3}{2}^{+}$ |

well the precise widths found in previous studies. Interpretation of the data, aided by R-matrix calculations and informed by previous results in the literature, revealed four further resonant structures present in the excitation functions. Their properties agree well with those obtained in the GANIL experiment, see Table 4.2. Two new states, labeled G and H in Fig. 4.13, were also observed. As projection of angular distributions was not possible, spin and parity assignments made here are inferred from previous works and remain tentative. In addition, there is also additional strength in the region of 1.3 - 1.7 MeV (GANIL Mountford *et al* in Fig 4.13). An additional broad seventh state (labelled E) has been included to account for this additional strength. It corresponds very well with the new broad resonance observed in the LLN/GANIL experiment.

Three conclusions should be written about this experiment:

- It was the first time at GANIL a nuclear reaction cross section was measured directly at low energy. In other words, GANIL with its post-accelerated radioactive beams is well adapted for this kind of measurement.
- The new experiment at GANIL confirmed the existence of the broad $\frac{1}{2}^{+}$ resonance.
- About the method. As it was shown in this experiment, resonant elastic scattering measurement, associated with an R-Matrix analysis of the excitation function, is also a very powerful method to perform the spectroscopy of nuclei above their particle emission thresholds. This experimental method was developed at GANIL and used successfully in several studies. Several examples are shown in Chapter 6.

4.4 Conclusion and Outlook

To summarize, the inelastic scattering reaction $^1\text{H}(^{19}\text{Ne}, p)^{19}\text{Ne}^*(p)^{18}\text{F}$ was measured in inverse kinematics at Louvain-La-Neuve to study the excited states in ^{19}Ne which can contribute to the $^{18}\text{F}(p, \alpha)^{15}\text{O}$ reaction cross section. The main objective of this experiment was to determine the spins of the excited

states above the proton emission threshold. Proton-proton coincidences between protons arising from the inelastic reaction and emitted from unbound $^{19}\text{Ne}^*$ states were used for determining energies, widths and for the first time spin values of the resonant states. Besides the remarkable agreement with the insofar known resonances, a new broad $\frac{1}{2}^+$ resonance was found at ~ 1.4 MeV above the reaction threshold. Despite the fact the new state properties was in perfect agreement with a recent theoretical prediction, a controversy started about the existence of this broad state. We performed a second experiment at GANIL in order to confirm its existence and properties. Direct measurements of the cross section of both the $^{18}\text{F}(p,\alpha)^{15}\text{O}$ and the $^{18}\text{F}(p,p)^{18}\text{F}$ reaction have been performed. Simultaneous fits to both data sets with the R-matrix formalism revealed several resonances, with the inferred parameters of populated states in ^{19}Ne in general agreement with previous measurements. Extra strength has been observed above $E_{c.m.} \sim 1.3$ MeV in the $^{18}\text{F}(p,p)^{18}\text{F}$ reaction and between 1.3-1.7 MeV in the $^{18}\text{F}(p,\alpha)^{15}\text{O}$ reaction. This is well described by a broad $\frac{1}{2}^+$ state, consistent with both the recent theoretical prediction and our first measurement. The low energy tail of this resonance contributes to a significant enhancement of the ^{18}F destruction rate at nova temperature. This reduces significantly the chance to observe γ -ray emission of ^{18}F from a nearby nova explosion with existing space telescopes.

A few words should be said about recent developments and the outlook:

4.4.1 The VAMOS experiment (E641S)

A third experiment about the ^{19}Ne spectroscopy was proposed at GANIL in 2011, accepted and performed [91] in 2013. This study was the subject of the Ph.D. thesis of Florent Boulay (I co supervised with B. Bastin and Gilles de France). The main motivation of this experiment was the search for the predicted second $\frac{1}{2}^+$ state below the proton threshold. The experimental technique was identical to the one of the first experiment, using a slightly higher energy of 10 MeV/nucleon, a mean intensity of 3×10^7 pps, and a thinner target of 1 μm . The experimental set up was improved. The excited states of ^{19}Ne were populated via the inelastic scattering reactions (p,p') occurring in the target. The scattered protons p', which have an energy from 20 MeV to 25 MeV in the range of interest, were detected at zero degree with the VAMOS magnetic spectrometer. In the setup, a telescope of $\Delta E(\sim 30 \mu\text{m})$ - $E(\sim 1.5 \text{ mm})$ annular silicon detectors was placed 10 cm from the reaction target and was used to detect protons (p") and α -particles, see Fig. 4.14. The first advantage of the experimental setup consisted on the rejection of the incident beam and therefore the suppression of the huge background induced by the use of the beam catcher. The other strength was the resolution that could be achieved in the reconstruction of the p' scattered protons measured with VAMOS. The resolution of the VAMOS spectrometer is about 1/500 (at best it could be 1/1000) in Brho, leading to 34 (17) keV in the center of mass spectra. The last main advantage was the large angular acceptance of VAMOS (up to ~ 60 msr) that could provide more statistics on the spectra.

The VAMOS spectrometer was used for the first time on the spectrograph mode to measure protons. One of the great technical challenges of the experiment consisted on the detection of very energetic protons (~ 20 MeV) with the drift chambers of VAMOS. The energy loss was only a few keV. A preparatory working program was initiated to define the optimal settings (pressure and tensions) using the Mayaito drift chamber prototype with combined offline (alpha source) and online (test experiment at the Institute of Nuclear Physics, located at Rez in Czech Republic using a proton beam of 25 MeV) measurements. Then, gain measurements of VAMOS drift chambers were realized with an alpha source. The extrapolation with GARFIELD simulations allowed to define the best pressure (40 mbar) and tensions (cathode:

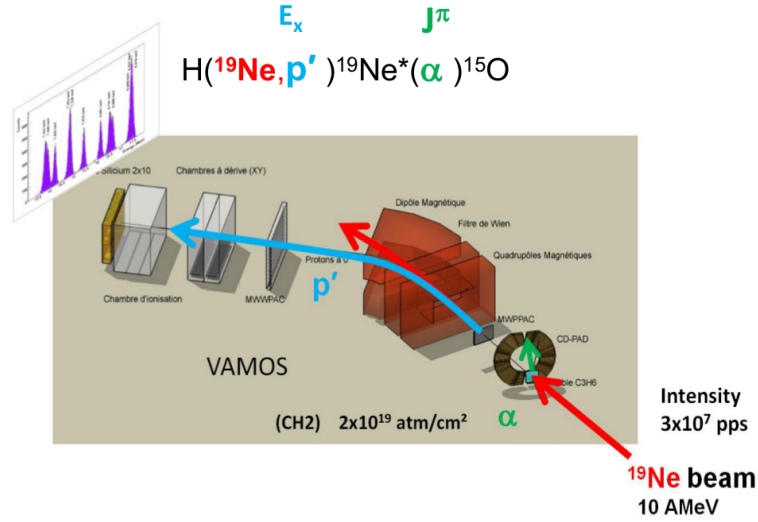


Figure 4.14: Drawing of the E641S experimental set up, from Ref. [91].

2200 V, wires: 1000 V) values to be set for the detection of p' protons of interest.

Results of this experiment were presented by Florent Boulay during the defense of his Ph.D. thesis. A paper is in preparation (we don't show spectra here for that reason). A first indication of the presence of this $\frac{1}{2}^+$ state was obtained.

Here we make a side comment about theory. We have used the code AZURE2 [92] for the calculation of the $^{18}\text{F}(p, \alpha)^{15}\text{O}$ reaction within the R-Matrix formalism. This $\frac{1}{2}^+$ state is bound for the proton emission. To take this level into account in the calculation of the reaction rate, it is needed to determine the ANC coefficient (asymptotic normalisation coefficient). We cannot get this parameter from the inelastic scattering experiment, nor from the resonant elastic scattering experiment. The spectroscopic factor predicted by Dufour and Descouvemont [79], $S_p=0.082$ could be used instead. We used a Woods-Saxon potential to calculate the wave function of the proton $u(r)$ (with $\int u(r)dr = 1$) in a single-particle configuration $^{19}\text{Ne}=^{18}\text{F}+p$ where ^{18}F is the core. The depth of the potential is adjusted in order to fit the binding energy of the proton. It is possible to deduce the single-particle ANC coefficient $C_{s.p.}$ through the formula:

$$u(r) = C_{s.p.} \times W_{-\eta, \ell + \frac{1}{2}}(-2kr) \quad (4.1)$$

where $W_{-\eta, \ell + \frac{1}{2}}(-2kr)$ is the Whittaker function. The relationship is true only far from the nucleus. And then, it is possible to deduce the ANC coefficient C through the relationship:

$$C^2 = C_{s.p.}^2 \times S_p \quad (4.2)$$

To illustrate the impact of this $\frac{1}{2}^+$ state on the reaction rate, cross section calculations are shown for three values of the ANC in Fig. 4.15. The change could be higher than a factor 10. The astrophysical impact of this new state was evaluated for the first time in Ref. [91]. Eventually, it was shown that the expected rate of nova detection with the INTEGRAL space telescope is reduced by a factor 20, from $\sim 2 \text{ year}^{-1}$ to $\sim 0.1 \text{ year}^{-1}$. The latter is in better agreement with the non observation of event since INTEGRAL was launched by the European Space Agency into Earth orbit in 2002.

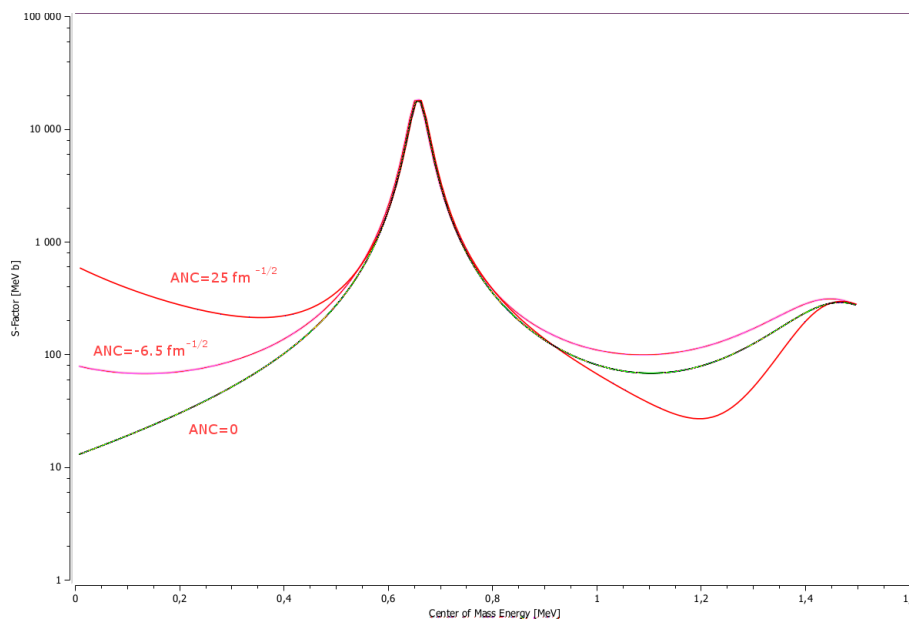


Figure 4.15: The cross section of the $^{18}\text{F}(p,\alpha)^{15}\text{O}$ reaction is shown for different values of the subthreshold state ANC coefficient. It illustrates the impact of this state in the low energy range. In the astrophysical region ($E < 0.4$ MeV), the change could be higher than a factor 10.

4.4.2 The $^{15}\text{O}(\alpha,\alpha)^{15}\text{O}$ experiment (E442S)

Within the framework of this scientific program to understand the novae, we performed another experiment to investigate the spectroscopy of the ^{19}Ne nucleus. The main idea was to obtain an excellent energy resolution in order to see if several states are folded together. Several states, known in the mirror nucleus, are still missing in ^{19}Ne . The method used was the resonant elastic scattering at low energy. We measured $^{15}\text{O}(\alpha,\alpha)^{15}\text{O}$. Since ^{15}O is radioactive, we had to measure this elastic reaction in inverse kinematics using a thin helium gas target and a radioactive beam. In fact, the excitation function is measured at once from the entrance energy down to the outgoing energy of the heavy ions, after they have crossed the gas target and lost energy. The inverse geometry and small specific energy loss of the alpha strikingly reduce the influence of the beam spread and straggling on the final resolution. This method is very well suited for secondary beams since the limited intensity is compensated by the large cross sections (several hundreds of mbarn/sr). From the shape of the resonances one can obtain the angular momentum of the reaction, and finally deduce the spin assignment of the states. Another advantage in that case is that the first excited state in ^{15}O is very high, at 5183 keV, which means the contribution from inelastic scattering is forbidden. In fact, all inelastic processes producing alpha particles are totally forbidden.

The experimental setup is shown in Fig. 4.16. The zero degree magnetic spectrometer LISE was used to select the scattered α -particles and to reject the intense radioactive beam. The gas target was located at the object point of the spectrometer. We built a special target of helium, a cell with 2.5 and 1.5 μm mylar windows. A silicon detector, with an extremely good energy resolution of 11.46 keV FWHM resolution (lab) was placed at the image point of the spectrometer (in D4). A realistic simulation of the expected

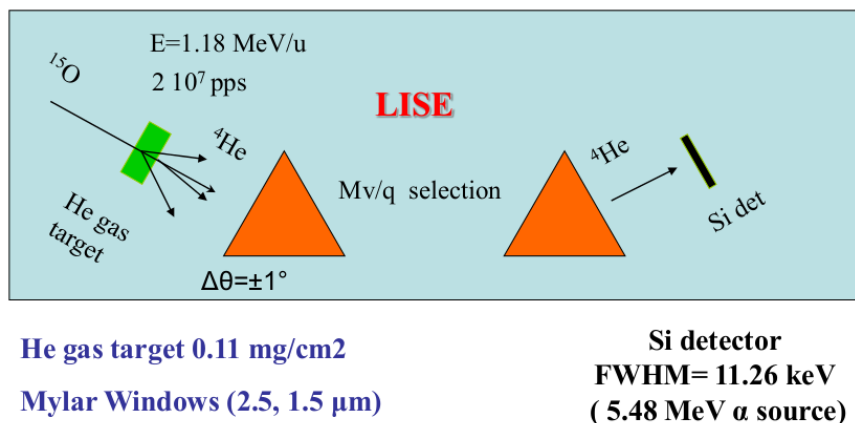


Figure 4.16: Schematic drawing of the experimental set up used to measure the reaction ${}^4\text{He}({}^{15}\text{O},\alpha){}^{15}\text{O}$.

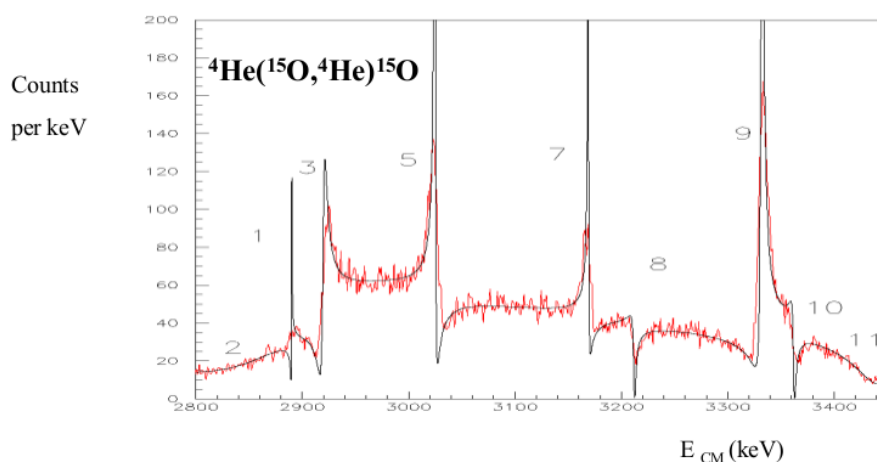


Figure 4.17: Expected spectrum obtained after realistic simulations. The excellent resolution could allow us to observe yet unknown resonances in the region of astrophysical interest. The spin of the states could be assigned from an analysis of the shape of the resonances.

spectrum is shown in Fig. 4.17. The energy resolution is expected to be ~ 3.3 keV (FWHM) in the center of mass system.

This experiment was not successful since the scattered α -particles were strongly contaminated by unknown particles, whatever was the gas pressure or the selection conditions of the LISE spectrometer. Despite the fact that a great part of the beam time was dedicated to identify the origin of the noise, it was not possible to solve this problem. The same problem happened in several other experiments. The noise seems to be incident particles with a kind of continuous energy distribution.

However, the proposed experimental method is still very interesting and promising. The noise is produced somewhere in the beam line. It is one of our priorities to identify the origin of this problem and remove

it. In principle, once solved, we could submit the same proposal to the GANIL PAC committee. Another interesting idea is to use an active target, like ACTAR TPC. The noise could be strongly reduced by selecting each event with an interaction point within the gas target.

4.4.3 Study of another γ -ray emitter: ^{22}Na (E710)

Our scientific program about novae led us to perform a new experiment in August 2016. As it was shown here above, the γ -ray spectrum of the nova ejecta is dominated by the ^{18}F contribution a few hours after the explosion. Indeed, the emission resulting from $e^- e^+$ annihilation is the most intense γ -ray outcome of classical novae, but these γ -rays are emitted well before the visual maximum of the nova, i.e., before the nova is discovered, and have a very short duration (see Fig. 4.3). Other nuclei, i.e. ^{22}Na and ^{26}Al , dominate the spectrum several days or years after the explosion. These isotopes can be detected by space γ -ray telescopes. In particular, ^{22}Na decays with a 2.602 yr lifetime into a short-lived excited state of ^{22}Ne . The characteristic 1275 keV γ -ray line from ^{22}Na is considered as the best known test of novae models, given the short half-life of the parent, that allows to localise in time and space the astrophysical event. The flux of the 1275 keV γ -rays emitted from novae is directly proportional to the amount of ^{22}Na produced during the outbursts. The main destruction process of ^{22}Na during the novae explosion is the $^{22}\text{Na}(p,\gamma)^{23}\text{Mg}$ reaction. It was shown in Ref. [93] that an increase of the $^{22}\text{Na}(p,\gamma)^{23}\text{Mg}$ reaction rate by a factor 3.2 resulted in a reduction of the amount of ^{22}Na by a factor between 2 and 3, depending on the novae model. It means that the production of ^{22}Na is quasi inversely proportional to the rate of the $^{22}\text{Na}(p,\gamma)^{23}\text{Mg}$ reaction.

The two cross-section determinations of this reaction existing in the literature disagree [94]. These experiments, which aimed at providing a direct determination of the cross section at low energy, are very challenging since they involve the use of a radioactive ^{22}Na target. Both these measurements showed that the reaction rate is dominated in the Gamow window by one resonance at about 213 keV above the proton-capture threshold corresponding to the state in ^{23}Mg with $E_x=7786$ keV and $J^\pi=7/2^+$.

It is possible to show that the reaction rate (Section 1.13) can be written for this narrow resonance:

$$N_A \langle \sigma v \rangle = 1.4 \times 10^{-10} \frac{B(1-B)}{\tau(s)} T_9^{-\frac{3}{2}} e^{-\frac{2.472}{T_9}} \quad (4.3)$$

where B is the proton branching ratio, τ the lifetime in seconds, and T_9 the temperature in billion degrees. To calculate the rate at a temperature T_9 only two parameters are needed: B and τ . The measurement of these parameters was the aim of our experiment.

We (Caterina Mechelagnoli, F. de Oliveira *et al*) proposed to determine the lifetime of the 7.786 MeV state in ^{23}Mg with the Doppler Shift Attenuation Method (DSAM). We populated the state of interest with the reaction $^3\text{He}(^{24}\text{Mg}, ^4\text{He})^{23}\text{Mg}^*$ at 4.6 MeV/u. The ^3He nuclei were implanted onto gold foils at the Helmholtz-Zentrum Dresden-Rossendorf Institute of Ion Beam Physics and Materials Research (Germany). The ^{23}Mg nuclei excited to the level of interest were tagged with the α -particles detected with the VAMOS spectrometer placed at 0° and the γ -rays were detected with the state-of-the-art AGATA gamma spectrometer. The protons, emitted from the state of interest, were detected with the annular dE-E silicon detector called SPIDER located 12 cm after the target and covering angles between 9 and 20 degrees.

This experiment is very recent. Since the analysis of the data has just started, no spectrum is shown here. A lineshape analysis over the almost continuous angular distribution of AGATA will be perform to

extract the lifetime. In principle, in the same experiment, the branching ratio B could be obtained by measuring in SPIDER the number of protons emitted from the 7.786 MeV state observed in coincidence with α -particles in the VAMOS spectrometer.

4.4.4 Related developments

To finish this Chapter, let's highlight 3 important related developments:

- With the first study, we proposed a new technique, the inelastic scattering, to perform efficiently the spectroscopy of nuclei and to determine the spin of the states in a model-independent way. Since then, this new technique had been used in several experiments proposed by other groups. For example recently, the technique was proposed at GANIL by F. Hammache *et al* (E746) in order to study of the astrophysical reaction $^{30}\text{S}(\alpha, p)^{33}\text{Cl}$, important for the X-ray busters, through the measurement of the inelastic scattering reaction $^{34}\text{Ar}(p, p')^{34}\text{Ar}^*$. This experimental technique could be used in several other problems in astrophysics and in nuclear structure.
- In many interesting cases, these studies require radioactive beams. We would like to emphasise the need for new and intense radioactive beams.
- The INTEGRAL space telescope mission had been extended to December 2016, and will be soon ended. A new generation of γ -ray space telescope is urgently needed if we want to observe γ -rays in the MeV range from novae outbursts. Several ideas have been discussed the last years, including the e-ASTROGAM project [95] based on cerium-doped lanthanum bromide (LaBr3:Ce) scintillator, which had interesting properties for γ -ray astronomy as good energy resolution, high detection efficiency and fast time response.

Light curve of X-ray bursts

Sommaire

| | |
|--|-----------|
| 5.1 Introduction: The XRB-LCP problem | 57 |
| 5.2 Predicting the rate of $^{15}\text{O}(\alpha,\gamma)^{19}\text{Ne}$ reaction | 59 |
| 5.3 Conclusion and Outlook | 60 |

Que le soleil est beau quand tout frais il se lève, Comme une explosion nous lançant son bonjour !

Le Coucher du Soleil romantique, Baudelaire

5.1 Introduction: The XRB-LCP problem

X-ray bursts (XRB) are astrophysical phenomena similar to novae explosions [96, 97, 98]. XRB are characterized by a repeated sudden increase of X-ray emission within only a few seconds to a total energy of about 10^{39} ergs (novae are one million times more intense, and type I supernovae are one million times more intense than novae), followed by a 5-100 seconds decline, see the example shown in Fig. 5.1. The recurrence time between bursts can range from hours to days.

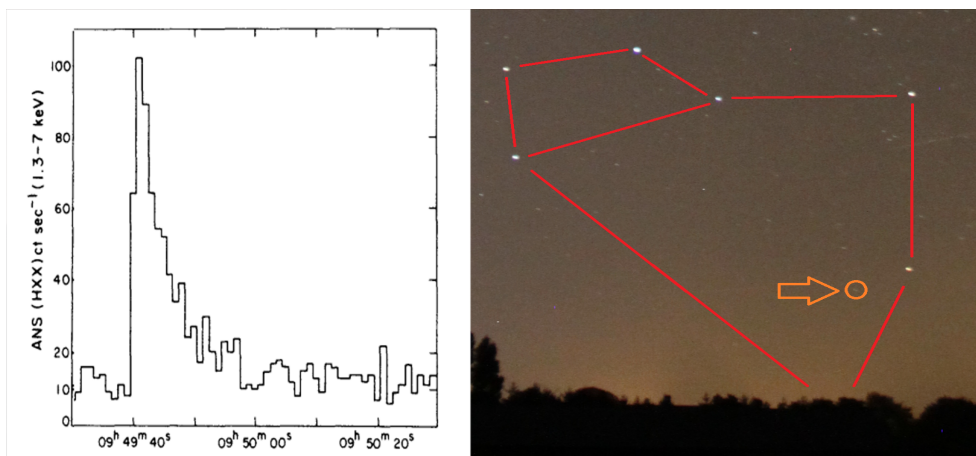


Figure 5.1: The very first X-ray burst was observed in the constellation of Sagittarius. From Ref. [96].

It is thought that these explosions are produced in binary systems of close stars, as it is in the novae but with the white-dwarf-star being replaced by a neutron-star. X-ray bursts are explained as thermonuclear explosions in the atmosphere of the accreting neutron star. When critical values for density and temperature are reached in the neutron star atmosphere, the freshly accreted hydrogen and helium ignites and burns. The rate of energy release in the hot CNO (HCNO) cycles is limited by the β^+ decays of ^{14}O ($T_{1/2}=71$ s) and ^{15}O ($T_{1/2}=122$ s), the longest lived and most abundant radioisotopes in the HCNO cycles, see Fig. 5.2.

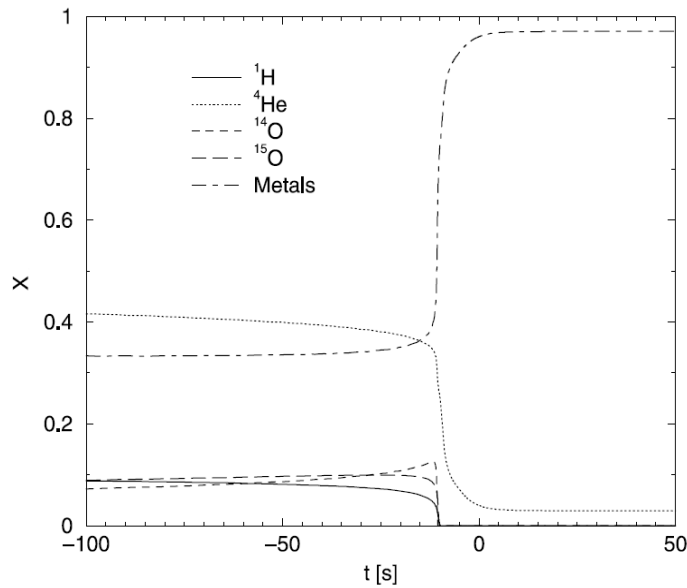


Figure 5.2: Hydrogen, helium, CNO type matter, and metal (the rest) mass fractions as a function of time, calculated for a XRB. From Ref. [99].

One of the biggest problems about the XRB is their light curve profiles (LCP). Can we understand their LCP? What are the conditions that make the outburst occur? It has been shown that the strength of the $^{15}\text{O}(\alpha,\gamma)^{19}\text{Ne}$ reaction not only controls the ignition point of the burst but affects also the burst recurrence rate [100]. Indeed, if the rate of the α -capture by ^{15}O reaction is comparable to the β^+ decay rate of this nuclei, ^{19}Ne can be formed in appreciable numbers and substantial energy is released. The ^{19}Ne nucleus can then capture a proton, yielding ^{20}Na , which in turn β^+ decays to ^{20}Ne , breaking out the HCNO cycles into the rp process. The rp process converts the light element fuel into heavy elements up to Cd-Sn within only a few seconds.

The breakout reaction $^{15}\text{O}(\alpha,\gamma)^{19}\text{Ne}$, which regulates the flow between the hot CNO cycle and the rp process, is critical for the explanation of the burst amplitude and periodicity of X-ray bursters. Knowing the rate of the $^{15}\text{O}(\alpha,\gamma)^{19}\text{Ne}$ reaction is a prerequisite for understanding XRB LCP.

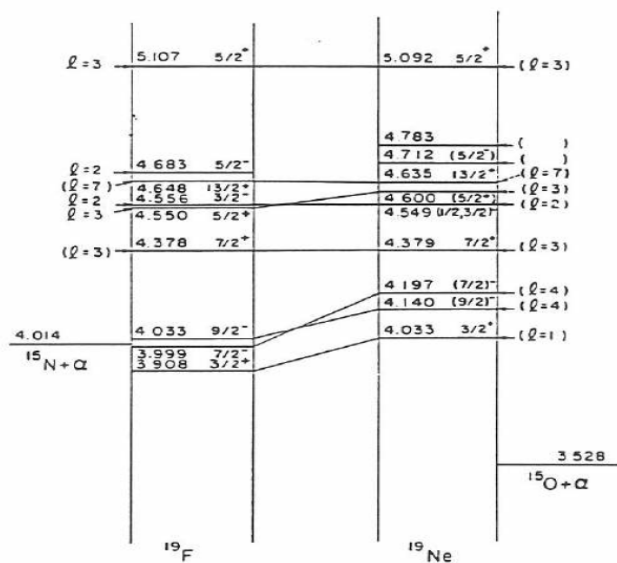


Figure 5.3: Comparison of the levels schemes of the mirror nuclei ^{19}Ne and ^{19}F .

5.2 Predicting the rate of $^{15}\text{O}(\alpha,\gamma)^{19}\text{Ne}$ reaction

Direct measurement of the $^{15}\text{O}(\alpha,\gamma)^{19}\text{Ne}$ reaction is not possible now since the count rate predicted for this reaction is about 1/hour using an extremely intense radioactive beam of ^{15}O with 10^{11} pps (not yet available in the world).

The reaction $^{15}\text{O}(\alpha,\gamma)^{19}\text{Ne}$ being the mirror of the $^{15}\text{N}(\alpha,\gamma)^{19}\text{F}$ reaction studied in Chapter 3, we were well placed to study the first reaction indirectly. We predicted the unknown properties of the compound nucleus ^{19}Ne . Energies of the ^{19}Ne levels were well known, and the corresponding states in the mirror nucleus ^{19}F are shown in Figure 5.3. Several branching ratios $\frac{\Gamma_\alpha}{\Gamma_{\text{total}}}$ were measured by transfer reaction [101]. The missing parameters were calculated from the properties of the mirror nucleus ^{19}F we have measured, see Chapter 3, and from unknown properties that we have supposed. To perform the calculations, we have chosen to take the measured dimensionless reduced alpha widths of ^{19}F , that is $\theta_\alpha^2(^{19}\text{Ne}) = \theta_\alpha^2(^{19}\text{F})$. The alpha widths in ^{19}Ne are calculated using the relations

$$\Gamma_\alpha(^{19}\text{Ne}) = 2\gamma_\alpha^2 P_L(^{19}\text{Ne}) \quad (5.1)$$

$$\gamma_\alpha^2 = \Theta_\alpha^2 \gamma_W^2 \quad (5.2)$$

with γ_W^2 the Wigner width limit and $P_L(^{19}\text{Ne})$ the penetrability through the Coulomb barrier of the α -particle. The obtained new values are shown in Fig. 5.4.

Final results are shown in Table 5.1. We adopted the γ -widths of the analogues states in ^{19}F . In the last column, it is shown the ratios between the new resonance strengths $\omega\gamma$ and the former values proposed by Langanke *et al* given Ref. [103].

We obtained results relatively close to those of Langanke *et al* [103], it might seem particularly surprising for the level $E_x = 4.377$ MeV because our new value of the α -width is about 60 times lower than that

| $E_x(^{19}\text{Ne})$ (MeV) | $E_x(^{19}\text{F})$ (MeV) | J^π | Θ_α^2 (10^{-2} à 5 fm) | Γ_α (1) (MeV) |
|--------------------------------|-------------------------------|---------|--|------------------------------|
| 4,140 | 4,033 | 9/2- | 13,5 (3) | — |
| 4,197 | 3,999 | 7/2- | 13,5 (3) | — |
| 4,379 | 4,377 | 7/2+ | 0,56 (3) | — |
| 4,635 | 4,648 | 13/2+ | 0,35 (2) | — |
| 4,710 | 4,683 | 5/2- | — | $2,1 \cdot 10^{-9}$ |

Figure 5.4: Properties of the ^{19}Ne states. (1) Measured directly Ref. [101], (2) taken from the theoretical prediction of Ref. [102] and corrected for $s=5$ fm, (3) our values deduced from the mirror nucleus ^{19}F .

Table 5.1: Properties of the ^{19}Ne levels used in this study. The last column corresponds to the ratios between the new resonance strengths $\omega\gamma$ and the former values proposed in Ref. [103].

| $E_x(^{19}\text{Ne})$ (MeV) | Γ_α (meV) | Γ_γ (meV) | Ratio |
|--------------------------------|--------------------------|--------------------------|-------|
| 4.140 | 1.13×10^{-3} | 9.8 | 1.1 |
| 4.197 | 5.6×10^{-3} | 35 | 1.1 |
| 4.379 | 0.2 | > 60 | 0.29 |
| 4.635 | 1.6×10^{-5} | 0.3 | 3.5 |

extracted from the rate of Caughlan and Fowler [46]. In fact, Langanke *et al* were very well wise to use for this level, not the value from Caughlan and Fowler, but a lower value, as arbitrary as the former value. The ratio between the rate of the $^{15}\text{O}(\alpha,\gamma)^{19}\text{Ne}$ reaction corrected by us to the former rate presented in Ref. [46] as a function of the temperature un billion degrees is shown in Fig. 5.5. The agreement is quite satisfactory. Our new results confirm the choices of Langanke *et al* in the calculation of this reaction rate.

We don't discuss here the astrophysical impact of this study. The new rate was not so different from the former one. A study on the sensitivity of the curve light profile to the $^{15}\text{O}(\alpha,\gamma)^{19}\text{Ne}$ reaction rate can be found in Ref. [104, 105].

5.3 Conclusion and Outlook

Most of the astrophysical reactions involving a radioactive nucleus cannot be measured directly due to the lack of beams. An educated guess about the ^{19}Ne properties allowed predicting the rate of the reaction $^{15}\text{O}(\alpha,\gamma)^{19}\text{Ne}$, but the prediction was still quite arbitrary. We used the measured properties of the mirror nucleus ^{19}F (Chapter 3) to deduce those of ^{19}Ne and calculate the rate of the reaction. Indirect measurements are sometimes a good way, if not the only way, to obtain the necessary pieces of information to calculate the astrophysical reaction rates.

For the outlook, two main ideas should be presented:

- The rate of the $^{15}\text{O}(\alpha,\gamma)^{19}\text{Ne}$ reaction is far from being well known. Firstly, the properties of ^{19}F

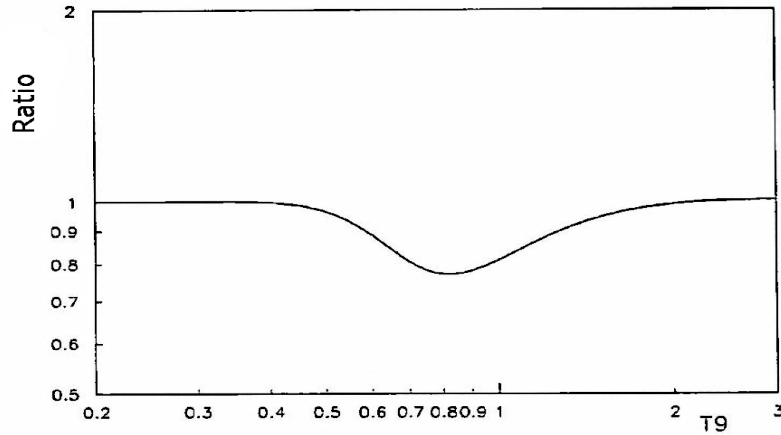


Figure 5.5: Ratio between the rate of the $^{15}\text{O}(\alpha,\gamma)^{19}\text{Ne}$ reaction corrected by us to the former rate presented in Ref. [46] as a function of the temperature in billion degrees. The change is not huge since the former study used a guessed value of $\theta_\alpha^2=0.02$ for the $E_x=4.378$ MeV state instead of usual value of 0.1, in better agreement with our measured value of $\theta_\alpha^2=0.006$.

used in the calculations of the ^{19}Ne rate are not well known. The α -width of the $E_x=4.378$ MeV state is known with a factor 2 uncertainty ($\Gamma_\alpha = (1.5_{-0.8}^{+1.5}) \times 10^{-9}$ eV). Secondly, we assumed the equality of the reduced α -widths between mirror nuclei. This symmetry is not always true. We published a study about this question, see Ref. [55]. These questions were also discussed in Ref. [106]. It was found that the equality of reduced widths between mirror nuclei is true only within a factor 10, especially when the spectroscopic factors are small.

Other rules can be used to deduce the unknown properties. For example, we can assume the identity of the structure for all members of a K^π band. This also apply to the $E_x=4.378$ MeV state in ^{19}F . In the Ref. [55] we discussed that this equality is true only within a factor 10.

- The isotope ^{14}O is very abundant before the outburst of the XRB. If the temperature and the reaction rate are high enough, it is quickly transformed into ^{15}O through the chain of reactions $^{14}\text{O}(\alpha,p)^{17}\text{F}(\beta,\gamma)^{18}\text{Ne}(\beta^+)^{18}\text{F}(\beta,\alpha)^{15}\text{O}$, with a lot of energy released. The first reaction $^{14}\text{O}(\alpha,p)^{17}\text{F}$ is still badly known. The $^{14}\text{O}(\alpha,p)^{17}\text{F}$ reaction rate is governed by the properties of states in the compound nucleus ^{18}Ne in the energy range between the $^{14}\text{O}+\alpha$ threshold ($E_x \sim 5$ MeV) and $E_x \sim 7$ MeV. In particular, at temperatures $T \leq 10^9$ K the $^{14}\text{O}(\alpha,p)^{17}\text{F}$ reaction rate is believed to be dominated by a single resonance arising from a $J^\pi = 1^-$ state at 6.15 MeV in ^{18}Ne , whereas several other states at $E_x = 7-7.5$ MeV could contribute to the rate at higher temperatures ($T \sim 3 \times 10^9$ K), relevant to XRB. Also a non-resonant reaction contribution is expected to be significant in the excitation energy region between 6 and 7 MeV where no resonant state is present in ^{18}Ne . This contribution, however, is still experimentally unconstrained. An experiment (E560S - spokesperson M. Aliotta) was scheduled at GANIL in order to measure directly the cross section of this reaction at low energy, and so to put constraints on the cross section. This experiment did not succeed. The beam was accelerated to 3.5 MeV/u, followed with a stripper foil in order to purify the beam, and a degrader to reduce the beam energy to ~ 1.7 MeV/u. The degrader was located

in front of the helium gas target. The degrader was at the origin of a huge background of protons and α -particles which contaminated the measured spectra.

Two ideas have been proposed to solve this problem. We could use an active target to degrade the beam energy and, in the same time, to select the good events with protons produced in the $^{14}\text{O}(\alpha,p)^{17}\text{F}$ reaction vertex. The second solution is to modify the CIME cyclotron of SPIRAL in order to accelerate the beam to lower energies (lower than 3.5 MeV/u) and to better purify the beam in the same time. Solution exist for relatively cheap price, this idea is discussed in Chapter 7.

Unbound Nuclei and Astrophysics

Sommaire

| | | |
|------------|---|------------|
| 6.1 | Introduction - Motivations | 64 |
| 6.2 | ^2He in the Sun | 65 |
| 6.3 | ^{19}Na: The first SPIRAL1 experiment (E400S) | 68 |
| 6.3.1 | Astrophysical motivation | 68 |
| 6.3.2 | Principle of the resonant elastic scattering | 69 |
| 6.3.3 | Experiment | 69 |
| 6.3.4 | Results | 71 |
| 6.3.5 | Astrophysical applications | 74 |
| 6.3.6 | Conclusion | 77 |
| 6.4 | ^{18}Na: A masterpiece in the two-proton radioactivity (E521aS) | 78 |
| 6.4.1 | Astrophysical motivation | 78 |
| 6.4.2 | Experiment | 78 |
| 6.4.3 | Results | 81 |
| 6.4.4 | Conclusion | 82 |
| 6.5 | ^{16}F: New pathway to bypass the ^{15}O waiting point (E442S) Probing Nuclear forces beyond the drip-line | 83 |
| 6.5.1 | Motivations | 83 |
| 6.5.2 | Experiment | 84 |
| 6.5.3 | Results | 85 |
| 6.5.4 | Interpretation | 85 |
| 6.5.5 | Conclusion and Outlook | 94 |
| 6.6 | ^{15}F: Reefs in the Sea of Instability (E521S) | 95 |
| 6.6.1 | Astrophysical motivation | 95 |
| 6.6.2 | Experiment | 96 |
| 6.6.3 | Results | 97 |
| 6.6.4 | Conclusion and Outlook | 99 |
| 6.7 | Final Conclusion | 100 |

Par existence, nous n'entendons pas une substance stable qui se repose en elle-même mais un déséquilibre perpétuel, un arrachement à soi de tout le corps.

Critique de la raison dialectique. J.P. Sartre

6.1 Introduction - Motivations

The boundaries for nuclear stability against particle emission are called drip lines. Beyond the drip lines, the particle emission time τ is usually very short, shorter than 10^{-21} seconds. As the state has a finite lifetime Δt , then it has an energy uncertainty ΔE . Unbound nuclei are observed as broad resonances with an energy uncertainty $\Delta E = \frac{\hbar}{2\Delta t} \sim 1$ MeV due to the Heisenberg's uncertainty principle.

Unbound nuclei are interesting in many ways:

- The proton drip line plays an important role in nuclear astrophysics, in the Big Bang Nucleosynthesis and in the Main Sequence and Red Giant stars (${}^2\text{He}$, ${}^4\text{Li}$, ${}^5\text{Li}$, ${}^8\text{Be}$ are unbound) and in the *rp*-process [99] during type I X-ray bursts where rapid proton captures reactions reaching the proton drip line (from ${}^{15}\text{F}$ up to ${}^{101}\text{Sb}$) should wait for β decays before proceeding further. Some unbound nucleus are directly involved in astrophysical reactions, that is the case of ${}^8\text{Be}$ in the triple alpha reaction, and ${}^2\text{He}$ in the *pp1* reaction chain as shown with simple model calculations in Section 6.2.

The extreme case of ${}^{19}\text{Na}$, involved in the double proton capture reaction ${}^{18}\text{Ne}(2p, \gamma){}^{20}\text{Mg}$, is discussed in Section 6.3.

The inverse reaction, the two-proton radioactivity, is directly linked to the two proton capture. The same models are used to calculate the two processes. The example of ${}^{18}\text{Na}$ is shown in Section 6.4.

- The symmetry of mirror nuclei is often used in nuclear astrophysics. The unknown properties of a neutron deficient nucleus can be deduced from the known properties of its mirror nucleus (see the case of ${}^{19}\text{Ne}/{}^{19}\text{F}$ in Section 4 and the mirror reactions ${}^{15}\text{N}(\alpha, \gamma){}^{19}\text{F}/{}^{15}\text{O}(\alpha, \gamma){}^{19}\text{Ne}$ in Chapter 5). But the mirror symmetry is not perfect, deviations are observed that make the matching sometimes uncertain. Unbound nuclei can be used to study these small deviations in extreme cases, in order to find some rules, to search the origin of these deviations. The structure of the low lying states in unbound nuclei is often simple, the states are often described with pure single particle configurations which makes the modeling and calculations much easier. Their mirror nuclei are often well known and can be compared with. Unbound nuclei are perfect cases to study the effect of the coupling with continuum. During the last decades, changes in nuclear shells ordering when going away from the valley of stability was observed, sometimes giving rise to new magic numbers. As an extreme case, it is very interesting to study the low lying states of nuclei located beyond the proton drip line. Could it be possible to measure some changes in the effective nucleon-nucleon interaction? This question is discussed in Section 6.5.
- Tunnelling through the Coulomb barrier is a purely quantum effect. In principle tunnelling is a very well known effect. Pushed to its extreme limits, some questions remains. What is the decay law of unbound nuclei? Is it a purely exponential decay law? This question is discussed in Section 6.5.
- There is a very interesting conjecture made by Ikeda *et al* [107] which can be formulated simply: The coupling to a nearby particle/cluster decay channel induces particle/cluster correlations in nuclear wave functions. In other words, the clustering is the generic near-threshold phenomenon in open quantum systems that does not originate from any particular property of the Hamiltonian or

some symmetry of the nuclear many-body problem. It is claimed in Ref [108] that this conjecture holds for all kinds of cluster states including unstable systems like dineutron, or ${}^8\text{Be}$. This mechanism, for example, could explain the origin of the Hoyle state in ${}^{12}\text{C}$, one of the most important states in astrophysics. There are chemical elements heavier than helium in the Universe only because there is this Hoyle state in ${}^{12}\text{C}$ that allows the triple alpha reaction $3\alpha \rightarrow {}^8\text{Be} + \alpha \rightarrow {}^{12}\text{C}$ to be efficient. The unbound nucleus ${}^{15}\text{F}$, presented in Section 6.6, could be one example of such a induced correlation.

In the following sections, a review of different studies involving unbound nuclei is presented. Not all these studies were motivated by astrophysical questions, but they all have a link with astrophysics.

6.2 ${}^2\text{He}$ in the Sun

The following work is a good introduction to the following Sections. This study was the subject of the Master thesis of Mr. Grégoire GIRAULT (a former student of mine).

Hans Bethe demonstrated for the first time in 1938, in his article "The Formation of Deutrons by Proton Combination" [109], that the reaction $p(p,e^+\nu)d$ is at the origin of the energy generated in the Sun. It is the first reaction of the $pp1$ chain of reactions at work in our Sun, the most important reaction in astrophysics since it is directly linked to the existence of life on Earth. The cross-section of the $p(p,e^+\nu)d$ reaction has been studied extensively, see Ref. [110] and references therein. The precise calculation of this reaction is very complicated, it is expressed in terms of nuclear overlap, ratio of the axial vector to the vector coupling constant g_A/g_V , correction to the nuclear matrix element due to exchanges of π and ρ mesons and phase space factor. It is calculated in the framework of the particle physics. There are two components, the impulse-approximation where the weak interaction takes place on a single proton (95 % of the cross-section), and the two-nucleon process where the protons are undergoing a strong interaction at the same time as the weak interaction [111]. The cross-section is so low, $\sigma \sim 10^{-24}$ b, that it is impossible to measure it with the current means. Figure 6.1 shows the calculated reaction rate.

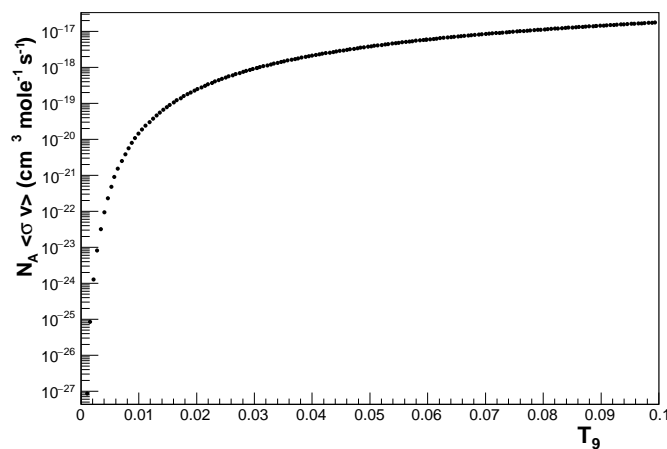


Figure 6.1: Calculated rate of the reaction $p(p,e^+\nu)d$ (CF88 [46]).

Here it is proposed, for the first time to my knowledge, an extremely simple model to calculate the rate of this reaction $p(p, e^+ \nu)d$. The model is based partly on the article of Hans Bethe. The main idea is summarized in Fig. 6.2. In the very hot and dense plasma of the Sun's core, protons collide incessantly

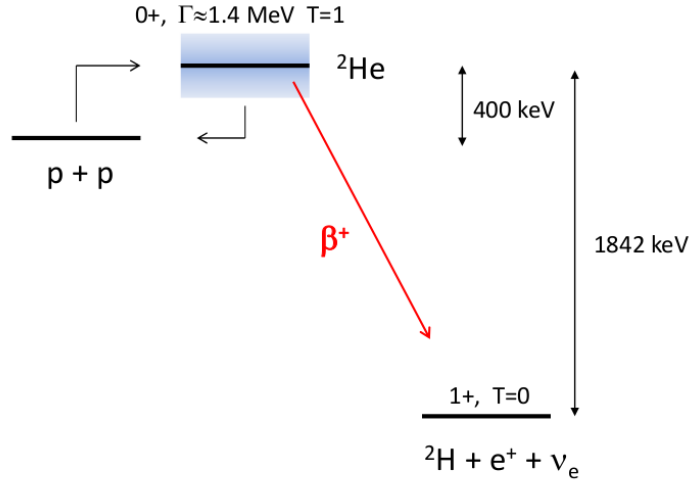


Figure 6.2: Scheme of the model proposed to calculate the rate of the reaction $p(p, e^+ \nu)d$.

forming the unbound nucleus ${}^2\text{He}$. The ground state of ${}^2\text{He}$ is observed in the elastic scattering reaction $p(p,p)p$ as a broad resonance located 0.4 MeV above the $p+p$ threshold with a width of ~ 1.4 MeV [112]. The ground state of ${}^2\text{He}$ decays back to the $p+p$ channel in less than 10^{-21} s. The cross section of the $p(p,p)p$ elastic scattering reaction can be calculated with the Breit-Wigner formula

$$\sigma(E)_{pp} = \pi \lambda^2 \omega \frac{\Gamma_p \Gamma_p}{(E - E_R)^2 + (\frac{\Gamma_{total}}{2})^2} \quad (6.1)$$

Sometimes, before ${}^2\text{He}$ decays back to $p+p$, it β -decays to ${}^2\text{H}$. The extremely weak branching to ${}^2\text{H}$ is equal to the ratio between the β -decay width and the total width $BR_{\beta^+} = \frac{\Gamma_{\beta^+}}{\Gamma_{total}} \approx \frac{\Gamma_{\beta^+}}{\Gamma_p}$, this gives

$$\sigma(E)_{p,\beta^+} = \sigma(E)_{pp} BR_{\beta^+} = \pi \lambda^2 \omega \frac{\Gamma_p \Gamma_{\beta^+}}{(E - E_R)^2 + (\frac{\Gamma_{total}}{2})^2} \quad (6.2)$$

The β -decay width is calculated simply with

$$\Gamma_{\beta^+} = \frac{\hbar}{2 t_{\beta^+}} \quad (6.3)$$

with t_{β^+} the β -decay half-life of ${}^2\text{He}$ if it were bound. It is possible to calculate it since it would have been a $(J^\pi=0^+, T=1)$ to $(J^\pi=1^+, T=0)$ Gamow-Teller (GT) transition. The GT transition the most similar to this one is the β -decay of the neutron $n \rightarrow p$ which has $\text{Log } ft = 3.0$. Let's suppose $\text{Log } ft_{\beta^+} = 3.0$. Since f is the Fermi function, it is easy to calculate t_{β^+} . One get $t_{\beta^+} = 530$ s at the maximum of the ${}^2\text{He}$ resonance.

Since ${}^2\text{He}$ is a resonance, it has not one well defined energy but a broad distribution of energies. This fact has to be taken into account in the calculation of the cross-section $\sigma(E)_{p,\beta^+}$. All parameters have to be function of the energy [109]

$$\sigma(E)_{p\beta^+} = \pi\lambda^2 \omega \frac{\Gamma_p(E)\Gamma_{\beta^+}(E)}{(E - E_R)^2 + (\frac{\Gamma_{total}(E)}{2})^2} \quad (6.4)$$

$$\Gamma_{\beta^+}(E) = \frac{\hbar}{2 t_{\beta^+}(E)} \quad (6.5)$$

$$\Gamma_p(E) = \Gamma_p(E_R) \frac{P(E)}{P(E_R)} \quad (6.6)$$

$$\text{Log}\{f(E) t_{\beta^+}(E)\} = 3.0 \quad (6.7)$$

$$f(W) = \text{sqr}t\sqrt{W^2 - 1} * (W^4/30 - 3 * W^2/20 - 2/15) + W/4 * \text{Log}(W + \sqrt{W^2 - 1}) \quad (6.8)$$

$$W = \frac{E(\text{keV})}{511} + 1 \quad (6.9)$$

The reaction rate is an integral of the cross-section over the full range of center of mass energies from 0 to infinity. This simple model gives the very interesting results shown in Fig. 6.3. The black line correspond to the ratio between the calculated rate of the $p(p,e^+\nu)d$ reaction to the CF88 one as a function of the temperature in billion degrees. It is mostly equal to 1. This simple model reproduces perfectly the rate of this reaction.

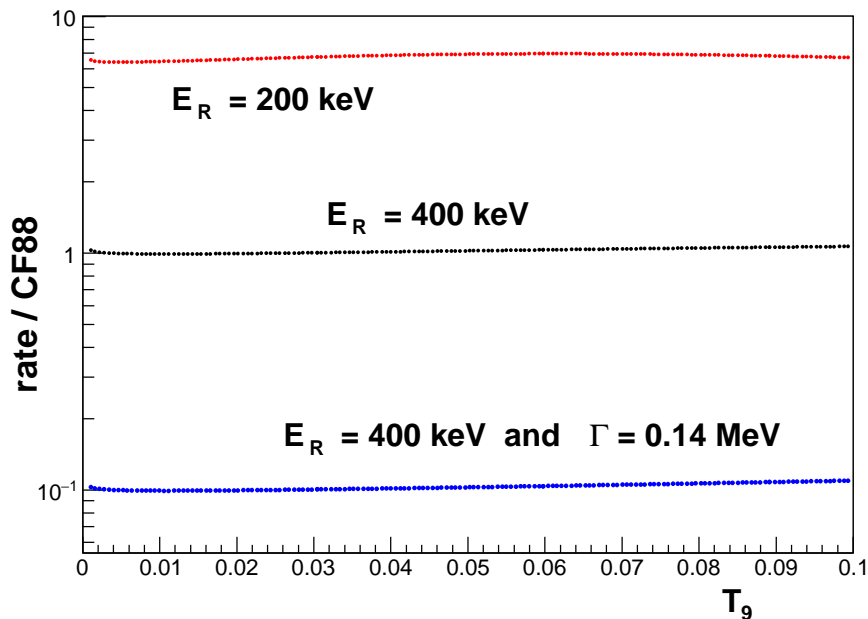


Figure 6.3: Ratio between the calculated rate of the $p(p,e^+\nu)d$ reaction to the CF88 [46] rate as a function of the temperature in billion degrees (black line). Results for a little more bound ${}^2\text{He}$ nucleus with $E_R = 0.2$ MeV, and a longer lived one with $\Gamma_p = 0.14$ MeV are shown with the red and the blue lines.)

The interests of this simple model are multiple. It is easy to calculate the rate of the reaction for different

values of the parameters. For example, the results for a little more bound ${}^2\text{He}$ nucleus with $E_R = 0.2$ MeV, and a longer lived one with $\Gamma_p = 0.14$ MeV are shown in Fig. 6.3 with the red and the blue lines. This simple model will be used later in Section 6.5 for other new calculations.

6.3 ${}^{19}\text{Na}$: The first SPIRAL1 experiment (E400S)

6.3.1 Astrophysical motivation

The hot CNO cycles and the rp process have been proposed as the dominant nucleosynthesis processes in explosive hydrogen burning, which takes place most notably in cataclysmic binary systems, such as novae and X-ray bursts. In this context, the double proton capture reaction ${}^{18}\text{Ne}(2p,\gamma){}^{20}\text{Mg}$, bridging the unbound nucleus ${}^{19}\text{Na}$ from the waiting point ${}^{18}\text{Ne}$ (see Fig. 6.4) to the bound nucleus ${}^{20}\text{Mg}$, was first studied by Görres et al. [113]. The idea of this very exotic direct two-proton capture reaction was a real

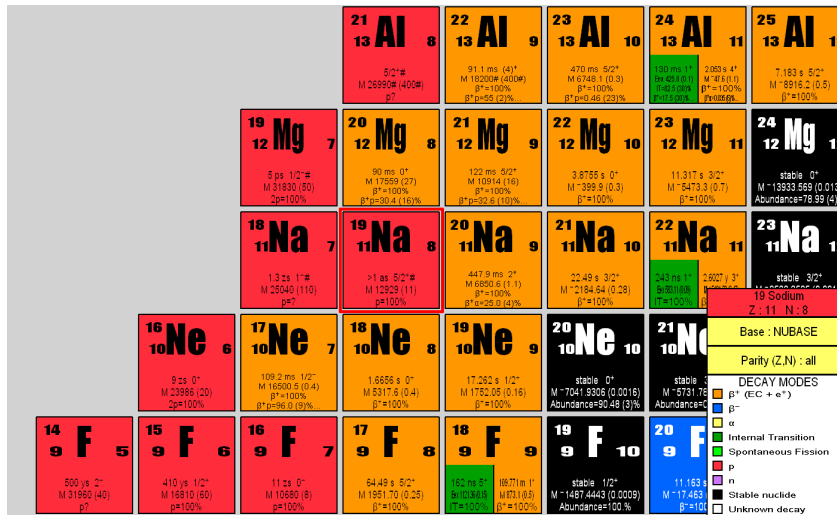


Figure 6.4: The isotope ${}^{19}\text{Na}$ is located one neutron beyond the proton drip line. (image produced with the code NUCLEUS-Win version 2.1 produced by AMDC at CSNSM)

innovation. The two-step formalism described by Nomoto, Thielemann and Miyaji [114] in the case of the triple-alpha reaction, was used to calculate the rate of the reaction. This ${}^{18}\text{Ne}(2p,\gamma){}^{20}\text{Mg}$ reaction is very interesting since ${}^{18}\text{Ne}(T_{1/2}=1.67$ s) is a waiting point in the reaction flow and since it is well produced in X-ray bursts through the reactions ${}^{16}\text{O}(p,\gamma){}^{17}\text{F}(p,\gamma){}^{18}\text{Ne}$ and ${}^{14}\text{O}(\alpha,p){}^{17}\text{F}(p,\gamma){}^{18}\text{Ne}$ [99]. It could be an alternative reaction to the breakout reaction ${}^{18}\text{Ne}(\alpha,p){}^{21}\text{Na}$. The rate of the reaction ${}^{18}\text{Ne}(2p,\gamma){}^{20}\text{Mg}$ depends on the properties of the intermediate unbound nucleus ${}^{19}\text{Na}$. The ground state of ${}^{19}\text{Na}$ is probably very narrow ($Q_p = +323$ keV), it is quasi-bound, making the case even more interesting. Because most of the properties of ${}^{19}\text{Na}$ and ${}^{20}\text{Mg}$ were not known, the reaction rate was calculated via shell-model predictions and systematics. The final conclusion of the Görres et al. study was that the two-proton captures couldn't compete for realistic astrophysical densities. However, it was not discussed how sensitive this conclusion is to the unknown properties of those nuclei. It could be that, using different parameters for the calculation of the reaction rate, a completely different conclusion could be drawn. In fact, the most sensitive parameters are the properties of the ${}^{19}\text{Na}$ ground state and of the first excited

state of ^{20}Mg above the proton emission threshold. A new experiment was proposed at GANIL to measure the properties of the low lying states of ^{19}Na , in order to constrain the double proton capture reaction $^{18}\text{Ne}(2p,\gamma)^{20}\text{Mg}$.

6.3.2 Principle of the resonant elastic scattering

In order to investigate the structure of ^{19}Na , the excitation function for the elastic scattering reaction $p(^{18}\text{Ne},p)^{18}\text{Ne}$ was measured with the ^{18}Ne post-accelerated radioactive beam from the SPIRAL1 facility at the GANIL laboratory. The principle of the experiment is described in Ref. [115]. In short, radioactive ions are sent onto a thick target containing hydrogen atoms, thick enough to stop the beam. Elastic scattering reactions between the ions and protons occur in the target along the slowing-down trajectory, from the incident energy down to zero. The scattered protons are ejected at forward angles. Due to their lower energy loss, scattered protons pass through the target without losing much of their energy, as shown in Fig. 6.5. The center mass energy of the interaction point can be deduced from the measured

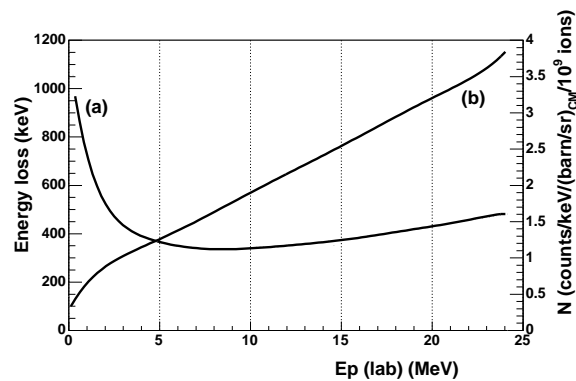


Figure 6.5: The energy loss (left axis in keV) of the protons inside the hydrogen target is plotted in curve (a) versus the proton energy (in MeV) in the laboratory frame. Moreover, the number of counts N (per barns per steradian in center of mass frame, per 10^9 incident ions, per keV in laboratory frame) is plotted (curve b, right axis) as a function of the detected proton energy.

energy of the protons, after correction of the energy lost in the target. The measured cross-section has to be corrected for different effects, mainly the fact that the effective target thickness is not constant. The count rate obtained in a simulation using a constant cross-section is shown in Fig. 6.5.

6.3.3 Experiment

This experiment was the first one performed with a radioactive beam from the SPIRAL1 facility at GANIL. The experiment was performed with a cryogenic hydrogen target of an average thickness of $1050 \pm 20 \mu\text{m}$ (using constant density of 88.5 mg/cm^3), that is thick enough to stop the beam inside the target. The scattered protons escaped the target because of their smaller energy loss, and were detected at forward angles in the laboratory frame. Therefore, the thick target made it possible to obtain a complete and continuous excitation function over a wide range of energies, by detecting the scattered protons and measuring their energies, without changing the energy of the incident beam. The radioactive beam was

accelerated with the new compact cyclotron CIME (Cyclotron d'Ions à Moyenne Energie) up to an energy of 7.2 MeV/u. The beam was contaminated by 15 % of ^{18}O and a very small amount ($< 1\%$) of ^{18}F . To get rid of the contamination, the LISE magnetic spectrometer was used as a separator. A thin carbon stripper foil ($40 \mu\text{g}/\text{cm}^2$) was placed at the target position of the spectrometer to select the 10+ charge state of the beam, yielding a pure $^{18}\text{Ne}^{10+}$ beam with a mean intensity of $2.5 \cdot 10^5$ pps. During the whole experiment, the beam intensity was measured and monitored by using a multi channel plate detector placed in front of the target. The pure ≈ 1 mm thick cryogenic hydrogen target was chosen for two reasons. Firstly, the use of compound targets (like $(\text{CH}_2)_n$) introduces other elements (e.g. Carbon) in which new reactions can occur and may pollute the measurement. Secondly, the use of a pure hydrogen target maximizes the counting rate because the highest stoichiometric ratio leads to a highest effective target thickness. Here, the enhancement ratio is 3.2. A cryogenic system was designed to make this target [116], see Fig. 6.6. Cryogenic target systems have already been designed in various laboratories, particularly by directly

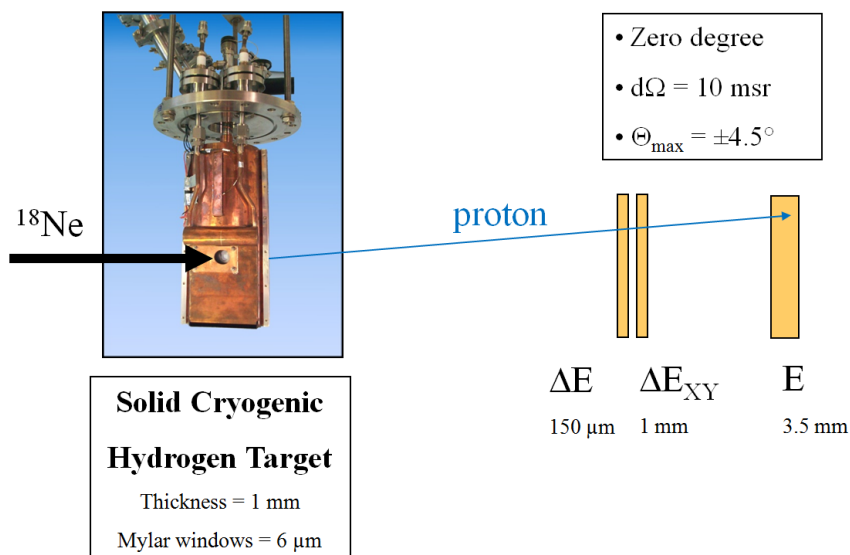


Figure 6.6: The ≈ 1 mm thick hydrogen cryogenic target used in the ^{19}Na experiment [116].

condensing H_2 gas to make the target. In the system developed at GANIL, we have opted for a transition to the liquid phase (16.2 K - 230 mbar) before progressive solidification of the hydrogen ($T < 13.9$ K). Liquid helium has been used as a cold source at 4 K and the growth of the hydrogen crystal has been imposed by the temperature gradient in the metal frame supporting the target. The target was made using a metal frame to which mylar windows (6 μm) were glued. A stack of frames has formed an H_2 target cell with a He cell on either side of the target. During the target production phase, equivalent pressure has been maintained on either side of the target windows. Once the target was formed, the helium gas was evacuated. The target was placed in the experiment chamber during nearly a week ($P \sim 20 \mu\text{W}$ on the target) and temperature has stayed below 9 K. The scattered protons escaped from the cryogenic target and were detected in a telescope of 3 silicon detectors 50 x 50 mm in size. A 150 μm ΔE detector, a 1 mm double-sided strip detector, and a 3.5 mm thick Si(Li) detector was used. The large total thickness

of the telescope was chosen in order to cover the full proton energy range. The ΔE detector was placed 317 mm behind the target in order to decrease the counting rate due to the β -rays from the decay of the beam particles. The second silicon detector was placed just behind the first one. The angular acceptance of this detector was $\pm 4.5^\circ$ (in the laboratory frame). Due to geometrical constraints, the Si(Li) detector was placed farther away from this ensemble, 495 mm from the target, corresponding to a calculated solid angle of $d\Omega_{lab} = 10$ msr.

6.3.4 Results

Figure 6.7 shows the excitation function for the elastic scattering of a radioactive ^{18}Ne beam on the proton target. A few broad resonances can be seen, labelled from A to F, corresponding to different excited states in the unbound nucleus ^{19}Na .

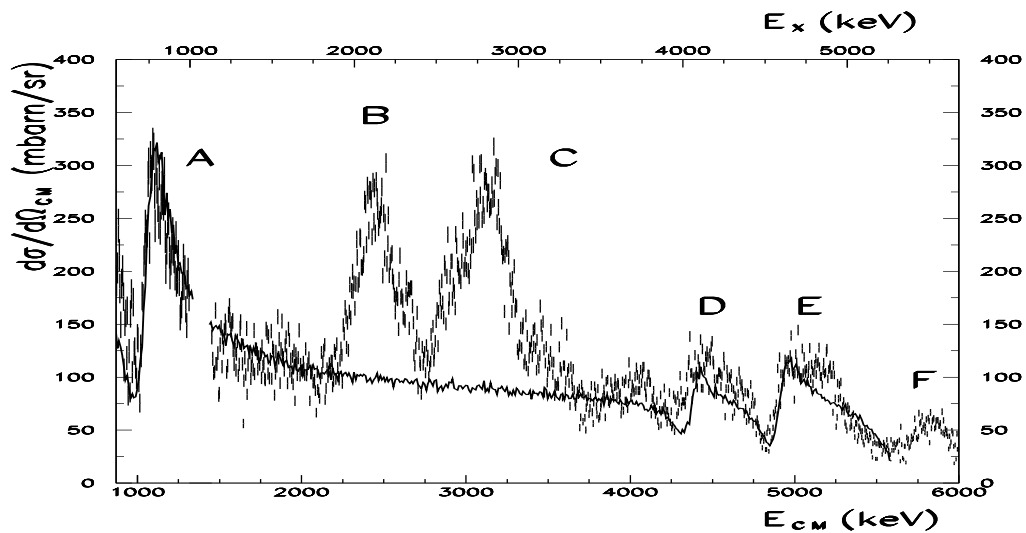


Figure 6.7: The reconstructed differential cross section ($\Theta_{CM} = 180^\circ$) for the elastic scattering reaction $p(^{18}\text{Ne},p)^{18}\text{Ne}$ is shown as a function of the center of mass energy E_{CM} (lower axis) and the excitation energy E_x in ^{19}Na (upper axis). The labels correspond to the peaks described in the text. The continuous line represents a R-Matrix calculation when the properties of four states of ^{19}Na are taken into account (see text). This figure corresponds to a measurement with a total of $3.4 \cdot 10^{10}$ incident ^{18}Ne nuclei.

- The characteristic shape of the first peak A in figure 3 suggests its spin and parity assignment $J^\pi = \frac{1}{2}^+$. For that state we obtained $E_{CM} = 1076 \pm 6$ keV and $\Gamma = 80 \pm 20$ keV. These values are in good agreement with the already known properties of the second excited state in ^{19}Na , previously measured at $E_{CM} = 1066 \pm 2$ keV with a width of $\Gamma = 101 \pm 3$ keV [117]. It is very interesting to compare this level with the known levels in ^{19}O , since the position of the excited states and the spectroscopic factors should be nearly identical for mirror nuclei. This level is positioned at an excitation energy of $E_x = 746 \pm 14$ keV in ^{19}Na , which only matches in the mirror nucleus with the known $\frac{1}{2}^+$ state at a position of $E_x = 1471.7 \pm 0.4$ keV. This means that the corresponding state in ^{19}Na is lowered by 725 ± 15 keV.

Table 6.1: Predicted properties of states in ^{19}Na from shell model calculations. The symbol E_x^{exp} corresponds to the values used to calculate the widths Γ_{gs} and Γ_{2+} . These correspond to the measured values of the excitation energies when known [117], or the excitation energies measured in the mirror nucleus ^{19}O [119], otherwise the predicted values E_x are used.

| Label | J^π | E_x (keV) | E_x^{exp} (keV) | Γ_{gs} (keV) | Γ_{2+} (keV) |
|-------|---------|----------------|----------------------|------------------------|------------------------|
| 1 | 5^+ | 0 | 0 | 0.2 eV | 0 |
| 2 | 2^+ | 293 | 120 | 0.6 eV | 0 |
| 3 | 1^+ | 1467 | 746 | 96 | 0 |
| 4 | 1^- | 2405 | - | 6.1 | 0.004 |
| 5 | 5^+ | 3167 | 3153 | 5.4 | 367 |
| 6 | 3^+ | 3746 | 3231 | 2.4 | 203 |
| 7 | 2^- | 4258 | 3944 | 51 | 0.017 |
| 8 | 2^- | 4667 | 4582 | 45 | 0.080 |
| 9 | 1^- | 4890 | - | 0.1 | 29 |
| 10 | 5^+ | 5010 | - | 6.9 | 216 |
| 11 | 3^- | 5466 | - | 161 | 1.3 |

To study the origin of this energy shift we have performed calculations using a potential model. The analog state in ^{19}O was built with a model of one neutron in the potential of a ^{18}O core. This model is clearly a good approximation when the dimensionless reduced width θ^2 (sometimes called spectroscopic factor) for this configuration is close to 1, which is the case in the mirror nucleus. In a first step we fitted the depth of a Wood-Saxon well to reproduce the experimental neutron separation energy. In a second step we used the same potential in addition to the Coulomb interaction for the mirror system of one proton and a ^{18}Ne core. The calculations predict an energy shift between analog states. The largest shift is observed for the s-orbital, which corresponds to the $J^\pi = \frac{1}{2}^+$ assignment of the state. In this case, we calculated an energy shift of 749 keV, a value in excellent agreement with the experimental one (725 ± 15 keV).

We also performed shell model calculations, in the *spsdpf* space and with the WBT [118] interaction, to predict the properties of the ^{19}Na states. Results are shown in Table 6.1. For this state, it is predicted $\theta^2 = 0.83$ that gives a width of $\Gamma = 96$ keV, again in excellent agreement with the experimental value ($\Gamma = 80(20)$ keV). In conclusion, this state can be mainly described by the shell model configuration $\pi(1d5/2)^2(2s1/2)^1$ and the origin of the energy shift is mainly due to the Coulomb interaction.

- The intense and broad ($\Gamma \approx 300$ keV) peak B at an energy $E_{CM} \approx 2.4$ MeV corresponds to an excitation energy of $E_x \approx 2.1$ MeV. Surprisingly it does not match any known state in the mirror nucleus. There are two known states in ^{19}O at energies of $E_x = 2.3715$ MeV and $E_x = 2.7790$ MeV. However, these states can not match because they are assigned with spins $J^\pi = \frac{9}{2}^+$ and $\frac{7}{2}^+$ implying an angular momentum of $\ell = 4$. This high value of the angular momentum is excluded in

our experiment because it corresponds to a very narrow width. There are also two other known states in the mirror nucleus, positioned at excitation energies of $E_x = 3.0671$ MeV and $E_x = 3.1535$ MeV. The spin assignments are $\frac{3}{2}^+$ and $\frac{5}{2}^+$, which means the angular momentum number is $\ell = 2$. Those states are also excluded because the Coulomb energy shift can not be so large as to explain the difference in energy.

- The broad ($\Gamma \approx 500$ keV) peak C is positioned at an energy of $E_{CM} \approx 3.1$ MeV, corresponding to an excitation energy of $E_x \approx 2.8$ MeV. The intensity and the shape of this peak are very similar to peak B. There is also no known analog state in the mirror nucleus which could correspond to this peak.
- Peaks D and E were fitted using an R-Matrix code. The two peaks fitted quite well with spin $\frac{3}{2}^-$.

The final result of the above analysis is plotted in Fig. 6.7 with a continuous line. We can observe a good overall agreement, except for the peaks B and C. The measured properties of the states are shown in Table 6.2.

Table 6.2: Properties of the peaks measured in ^{19}Na assuming a pure elastic scattering. As the R-matrix calculations cannot fit the peaks B and C, their reported properties are just indicative. See Fig. 6.7 and Table 6.1 for labels.

| Labels | J^π | E_x (keV) | Γ_{gs} (keV) |
|--------|-----------------|-------------------|---------------------|
| A - 3 | $\frac{1}{2}^+$ | 756 ± 18 | 80 ± 20 |
| B | - | ≈ 2.1 MeV | ≈ 300 keV |
| C | - | ≈ 2.8 MeV | ≈ 500 keV |
| D - 7 | $\frac{3}{2}^-$ | 4371 ± 10 | 30 ± 10 |
| E - 8 | $\frac{3}{2}^-$ | 4903 ± 10 | 50 ± 10 |

The two main observed peaks B and C can not be explained by the elastic scattering channel. Nevertheless, the shell-model calculations (Table 6.1) have revealed several broad states in the inelastic channel corresponding to the reaction: $p(^{18}\text{Ne}, p_1)^{18}\text{Ne}^*$. The use of a thick target does not allow us to separate the inelastic contributions from the elastic scattering.

We observed that inelastic reactions resulted in the emission of protons. We observed a few hundred of events with a proton multiplicity equal to two, see Fig. 6.8. This emission might have produced additional peaks in the one-proton excitation function. Indeed, the probability to detect only one proton after a two-proton emission is much larger than the probability to detect the two protons in coincidence, this means that the two-proton emission channel may induce extra peaks in the elastic scattering excitation function. In Fig. 6.9, the individual energies of the two-proton events measured in the present experiment were plotted as a continuous line. This spectrum is compared with that obtained for only one detected proton in the region of the peaks B and C (dashed line), elastic scattering subtracted. A similar pattern is observed for the two plots, two peaks are present but slightly shifted in energy and with different widths. In fact, the plots correspond to two different selections of the same events. In one case we impose the detection of the two protons, in the other case only one of the two protons is detected, and the differences between the plots are due to correlation and kinematical effects. The detailed analysis of the data showed that the

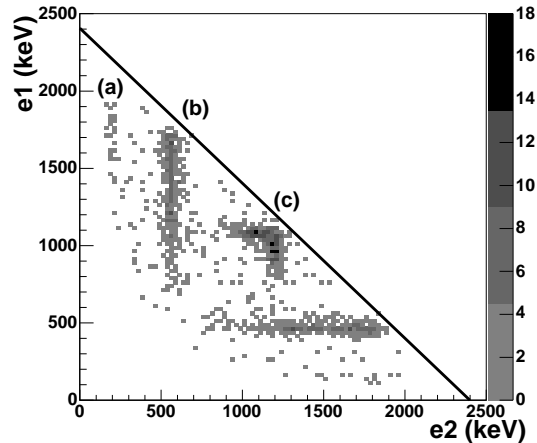


Figure 6.8: The reconstructed two dimensional energy distribution of the experimental two-proton events. The y axis corresponds to the center of mass energy of the first transition, from one excited state in ^{19}Na to one excited state in ^{18}Ne , the x axis is the energy of the second transition from the state in ^{18}Ne to $^{17}\text{F}_{gs}$. The continuous line corresponds to the maximum energy available in the center of mass system. The 3 clusters of events producing the vertical lines labelled (a), (b) and (c), correspond to sequential transitions.

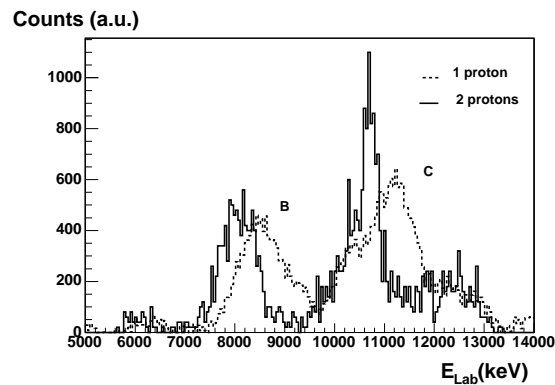


Figure 6.9: The individual energies in laboratory frame of the two-proton events are plotted with a continuous line. The dashed curve represents the spectrum obtained in the region of the peaks B and C, elastic scattering part subtracted. A similar pattern is observed.

two peaks B and C resulted from the detection of only one proton from a complex combination of several two-proton emissions as shown in the Fig. 6.10.

6.3.5 Astrophysical applications

The ground state and the second excited state of ^{19}Na have not been observed in this experiment. The properties measured for the second excited state are quite close to those guessed by Görres et al. [113].

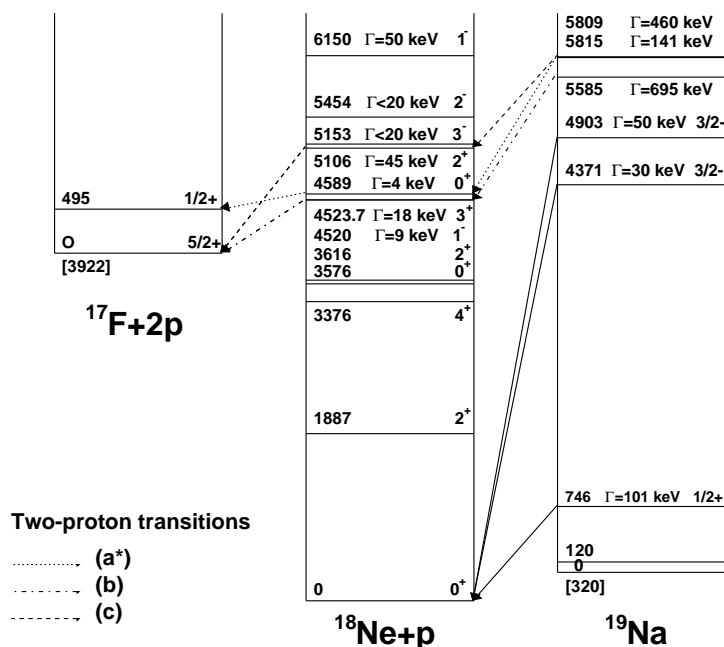


Figure 6.10: Level scheme which summarizes the known states properties of ^{19}Na . All known states on ^{18}Ne are also shown up to 6.2 MeV. The observed two-proton transitions are shown with dashed lines. They are all connected with known states in ^{18}Ne above the proton emission threshold.

For the astrophysical impact, the conclusion written in the Ref. [113] remains unchanged after this work: the reaction $^{18}\text{Ne}(2p, \gamma)^{20}\text{Mg}$ compete with other reactions only for densities larger than 10^9 gcm^{-3} , that is much larger than typical densities of X-ray burst and novae. Considering what we know, this reaction has no impact in astrophysics. But our knowledge about the ^{19}Na low lying states properties is still limited, particularly the first two states.

Now, let's estimate freely the maximum rate of the two-proton capture reaction. The reaction mechanism is schematically presented in Fig. 6.11. The first step is the capture of one proton by ^{18}Ne . The evolution equation is

$$\frac{dN_{^{19}\text{Na}}}{dt} = N_p N_{^{18}\text{Ne}} \langle \sigma v \rangle_{^{19}\text{Na}} - \lambda N_{^{19}\text{Na}} \quad (6.10)$$

where N_i are the densities of the nuclei i , $\langle \sigma v \rangle_{^{19}\text{Na}}$ the rate of the reaction $^{18}\text{Ne}(p,p)^{18}\text{Ne}$ through one resonance in ^{19}Na , and λ the decay constant of this resonance in ^{19}Na . At equilibrium

$$\frac{dN_{^{19}\text{Na}}}{dt} = 0 = N_p N_{^{18}\text{Ne}} \langle \sigma v \rangle_{^{19}\text{Na}} - \lambda N_{^{19}\text{Na}} \quad (6.11)$$

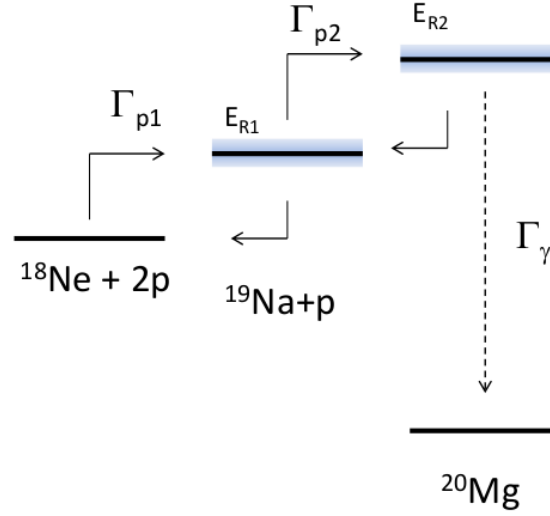


Figure 6.11: Schematic view of the two-proton capture reaction.

that gives

$$N_{^{19}\text{Na}} = \frac{1}{\lambda} N_p N_{^{18}\text{Ne}} \langle \sigma v \rangle_{^{19}\text{Na}} . \quad (6.12)$$

Before ^{19}Na decays back to $^{18}\text{Ne} + p$, it might capture a new proton. The evolution equation is

$$\frac{dN_{^{20}\text{Mg}}}{dt} = N_p N_{^{19}\text{Na}} \langle \sigma v \rangle_{^{20}\text{Mg}} . \quad (6.13)$$

This gives

$$\frac{dN_{^{20}\text{Mg}}}{dt} = N_p \frac{1}{\lambda} N_p N_{^{18}\text{Ne}} \langle \sigma v \rangle_{^{19}\text{Na}} \langle \sigma v \rangle_{^{20}\text{Mg}} = \frac{1}{2} \langle \sigma v \rangle_{^{18}\text{Ne}+2p} . \quad (6.14)$$

So the two-proton capture reaction rate is

$$\langle \sigma v \rangle_{^{18}\text{Ne}+2p} = 2 \frac{1}{\lambda} \langle \sigma v \rangle_{^{19}\text{Na}} \langle \sigma v \rangle_{^{20}\text{Mg}} . \quad (6.15)$$

Since these are narrow resonances, one get [120]

$$N_A \langle \sigma v \rangle_{^{19}\text{Na}} = 1.54 \times 10^{11} \mu^{-3/2} \omega \Gamma_{p1} T_9^{-3/2} \exp\left(-\frac{11.605 E_{R1}}{T_9}\right) \quad (6.16)$$

and

$$N_A \langle \sigma v \rangle_{^{20}\text{Mg}} = 1.54 \times 10^{11} \mu^{-3/2} \omega \Gamma_\gamma T_9^{-3/2} \exp\left(-\frac{11.605 E_{R2}}{T_9}\right) . \quad (6.17)$$

For the latter equation, we used the maximum value of $\gamma = \frac{\Gamma_{p2} \Gamma_\gamma}{(\Gamma_{p2} + \Gamma_\gamma)} = \Gamma_\gamma \sim 1 \text{ eV}$.

Finally, one get

$$N_A^2 \langle \sigma v \rangle_{^{18}\text{Ne}+2p} \approx 10^{-5} T_9^{-3} \exp\left(-\frac{11.605 (E_{R1} + E_{R2})}{T_9}\right) \quad (6.18)$$

since

$$\frac{1}{\lambda} = \tau = \frac{\hbar}{\Gamma_{p1}}. \quad (6.19)$$

It is interesting to note that the rate does not depend on the ^{19}Na width. The rate is maximum when $E_{R1} + E_{R2} = 0$, then

$$N_A^2 \langle \sigma v \rangle_{^{18}\text{Ne}+2p} \approx 10^{-5} T_9^{-3}. \quad (6.20)$$

This is the extreme limit of the two-proton capture reaction. This extreme limit is shown in Fig. 6.12 (blue line) in a density versus temperature plot. It shows that, at this extreme limit, the reaction could be effective in the novae explosions, as well as X-ray bursts.

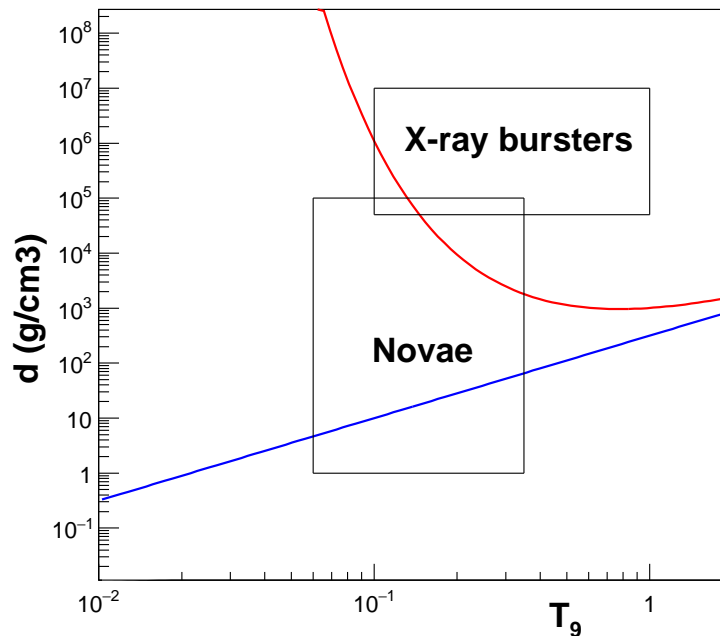


Figure 6.12: The extreme limit ($E_{R1} + E_{R2} = 0$) of the two-proton capture reaction $^{18}\text{Ne}(2p,\gamma)^{20}\text{Mg}$ is shown with the red line in this density versus temperature plot. The upper part above the red line corresponds to the conditions where the hydrogen is consumed in less than 1 seconde. The condition limits of the novae and X-ray outbursts are also shown. The red line corresponds to the case $E_{R1} + E_{R2} = 0.1$.

6.3.6 Conclusion

The results of this study were published in the article [121] and were presented in several conferences. This study was also the subject of the Master training of Peter Himpe (University of Leuven - Belgium). Later, a part of the experimental results were reproduced by Y. Jaganathen *et al* [122] within the new Gamow Shell Model in the coupled-channel representation (GSM-CC). This new model provided an unified description of low-energy nuclear structure and reactions using the same Hamiltonian.

We evaluated the astrophysical impact of the two-proton capture reaction $^{18}\text{Ne}(2p,\gamma)^{20}\text{Mg}$ using the formalism of sequential, quasi-simultaneous two-proton capture. It was found that, very probably, this reaction is interesting only at extreme densities well above the X-ray conditions. An improved formalism of direct three-body resonant radiative capture reaction was proposed by L. V. Grigorenko and M. V. Zhukov [123]. This formalism allowed them to update significantly the capture rate for the $^{18}\text{Ne}(2p,\gamma)^{20}\text{Mg}$ and $^{15}\text{O}(2p,\gamma)^{17}\text{Ne}$ reactions. The updated rate is four to nine orders of magnitude larger (in the temperature range of astrophysical interest). It was shown in Ref. [124] that, for realistic densities, temperatures and concentrations of α -particles the contributions of $^{15}\text{O}(2p,\gamma)^{17}\text{Ne}$ and $^{15}\text{O}(\alpha,\gamma)^{19}\text{Ne}$ processes become comparable in X-ray bursts.

6.4 ^{18}Na : A masterpiece in the two-proton radioactivity (E521aS)

6.4.1 Astrophysical motivation

The formalism used to calculate the astrophysical direct two-proton capture reaction is the same used to calculate the inverse process: the two-proton radioactivity. The correctness of the theoretical formalism used in the two-proton capture could be confirmed with a detailed study of a two-proton radioactivity. The mechanism of two-proton radioactivity can either be sequential via intermediate configurations or direct with simultaneous emission of the two protons to the continuum. However, there is no case of two-proton radioactivity where the intermediate nucleus (the mother nucleus minus one proton) is known. It is very important to know the properties of the intermediate nucleus since it is used to fit the nuclear potential of the calculations, and also because the two-proton radioactivity can proceed via a sequential decay through tails of resonances. We proposed to study ^{18}Na , the intermediate nucleus of the ^{19}Mg two-proton radioactivity.

6.4.2 Experiment

A new case of two-proton radioactivity, ^{19}Mg [125], was observed in 2007. Its half-life of 4.0(15) ps makes ^{19}Mg an intermediate case between short and long-lived two-proton decaying nuclei. The measured lifetime and p-p angular correlations [126] are well described by the predictions of Ref. [127] when assuming only d -wave single-particle states in the low-lying structure of the intermediate nucleus ^{18}Na and thus a dominant d^2 single-particle configuration for ^{19}Mg . Theoretical calculations of properties of ^{19}Mg depend strongly on the assumptions made about the structure of ^{18}Na and its mirror nucleus. The ^{18}Na nucleus is one of the rare intermediate nuclei which is accessible experimentally.

The dimensionless reduced widths θ^2 (sometimes called spectroscopic factors) were estimated with the shell model. The values shown in Tab. 6.3 were obtained with the OXBASH code [128] and the ZBM interaction [129] in the $1p_{1/2}$, $1d_{5/2}$ and $2s_{1/2}$ shells space. It predicts that the first six low-lying states can be described mainly (with $\theta^2 > 0.5$) by single particle configurations. The 1_1^- and the 2_2^- states are well described by the coupling $|^{17}\text{Ne}_{(3/2^-)}^* \otimes |\pi d_{5/2}\rangle$. The 2_1^- and the 3_1^- states arise from the coupling $|^{17}\text{Ne}_{(1/2^-)} \otimes |\pi d_{5/2}\rangle$. The two states 0_1^- and 1_2^- are described by the coupling $|^{17}\text{Ne}_{(1/2^-)} \otimes |\pi s_{1/2}\rangle$. The energies of the resonances can be predicted accurately from the known analog states of the mirror nucleus ^{18}N [130] according to the following prescription. We assumed pure core + neutron configurations to describe the states in ^{18}N . A nuclear Woods-Saxon potential was fitted in order to reproduce the binding

| J^π | E_r (keV) | $\theta^2 \text{ } ^{17}\text{Ne}_{g.s.}$ | | $\theta^2 \text{ } ^{17}\text{Ne}_{3/2^-}^*$ | | Γ to g.s (keV) | Γ to 3/2- (keV) | E_r this work | Γ to g.s this work | Γ to 3/2- this work |
|---------|----------------|---|------------|--|------------|-----------------------------|------------------------------|--------------------|---------------------------------|----------------------------------|
| | | $1d_{5/2}$ | $2s_{1/2}$ | $1d_{5/2}$ | $2s_{1/2}$ | | | | | |
| 1_1^- | 1300 | - | 0.086 | 0.921 | 0.183 | 22-1.3 | 0 | - | < 1 | < 1 |
| 2_1^- | 1500 | 0.644 | - | 0.311 | 0.042 | 8 | 0 | 1552(5) | 5(3) | < 1 |
| 0_1^- | <i>1650</i> | - | 0.759 | - | - | 189 | 0 | 1842(40) | 300(100) | < 10 |
| 2_2^- | 1950 | 0.004 | - | 0.507 | 0.028 | 0.2 | 0.45 | - | < 1 | < 1 |
| 1_2^- | 2450 | - | 0.654 | 0.031 | 0.027 | 1275 | 4.8 | 2030(20) | 900(100) | < 100 |
| 3_1^- | 2050 | 0.621 | - | 0.109 | - | 31 | 0.04 | 2084(5) | 42(10) | < 1 |

Table 6.3: Left side: Predicted resonance energies of the low-lying ^{18}Na states deduced from known analog states in the mirror nucleus ^{18}N or deduced from the ^{19}O $1/2^+$ state (in italic), and dimensionless reduced widths θ^2 calculated with the shell model and the corresponding proton widths to the g.s and the first excited state of ^{17}Ne (see text). (Right side) Measured spin, resonance energies and widths of the low-lying states in ^{18}Na .

energy of the states in ^{18}N . The information obtained was used to infer the position of the mirror core + proton states in ^{18}Na taking into account the Coulomb interaction. The states 0_1^- and 1_2^- are not known in ^{18}N [130]. In order to infer their position in ^{18}N , we used the same method as in ref. [131, 132]. We assumed the same mean value as for the ^{19}O $1/2^+$ second excited state, i.e. ~ 1.4 MeV [130] and an energy difference of 600 keV (that of the 2^- and 3^- doublet in ^{18}N). The partial proton widths were obtained using the relation $\Gamma_i = \theta^2 \Gamma_i^W$ where Γ^W is the Wigner limit. The calculated proton widths show a very small contribution from the inelastic channel and some states are very narrow. A width of 22 keV is calculated for the ground state, an even smaller value of 1.3 keV is obtained if the spectroscopic factor given in the ref. [133] is used. The spin-parity of the ^{18}Na ground state is predicted to be 1^- and the separation energy $S_p = 1.3$ MeV. This value means that all states in ^{18}Na are unbound to one-proton and also to three-proton emission.

We measured the resonant elastic scattering reaction $p(^{17}\text{Ne}, p)^{17}\text{Ne}$ in inverse kinematics. A pure beam of radioactive $^{17}\text{Ne}^{3+}$ ions was produced by the Spiral facility at GANIL with a mean intensity of 10^4 pps and accelerated to 4 A.MeV. The beam impinged on a fixed $50\mu\text{m}$ thick polypropylene C_3H_6 target coupled to a second rotating $50\mu\text{m}$ thick C_3H_6 target.

The two targets together were thick enough to stop the ^{17}Ne beam. This method, described for the first time in Ref. [134], has enabled us to measure the excitation function from 0.8 MeV to 3.8 MeV in the center-of-mass (CM). Scattered protons were detected by a ΔE -E annular telescope of silicon detectors placed at forward angles [135]. The telescope was composed of a thin ($\approx 40\mu\text{m}$) double-sided silicon strip ΔE detector and a 1.5mm thick E detector which covered laboratory angles from 5 to 20 degrees.

The scattered proton spectrum had background from beta-delayed protons emitted in the beta decay of ^{17}Ne . This nucleus decays with a lifetime of 0.109 s and a proton emission probability of $\sim 90\%$. More than 98% of the β -delayed protons were rejected by using a circular target of 60 cm diameter (FULIS target [136]) rotating at 1000 rpm. The ions were implanted in the target and moved away before their decay. A supplementary Microchannel Plate (MCP) was used for time of flight (ToF) and beam measurement with an efficiency close to 100%. From ToF measurement and ΔE -E selection, the scattered protons were identified and the proton spectrum was obtained (see Fig. 6.14).

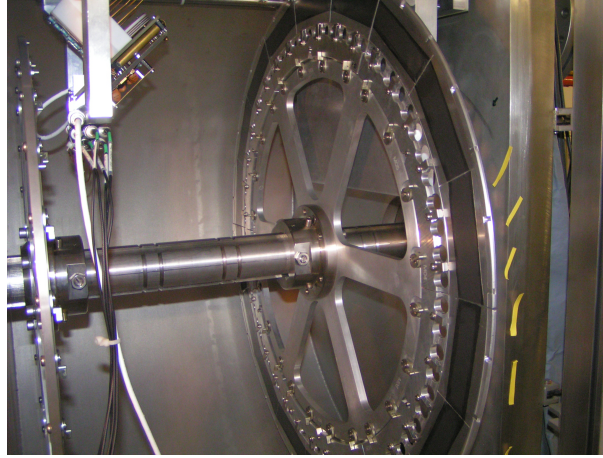


Figure 6.13: Rotating target (FULIS) used in the E521aS experiment.

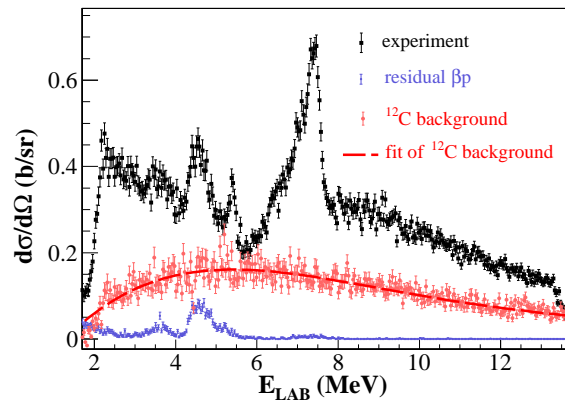


Figure 6.14: Proton spectrum measured between 5 and 20 degrees in the laboratory, reconstructed at 0 deg. These protons were produced by reactions between the ^{17}Ne beam and the polypropylene C_3H_6 target. The dashed line represents a fit of the ^{12}C background measured in this experiment (using a pure carbon target). The low lying data points (blue) represent the remaining contribution of βp decay of ^{17}Ne after selection with ToF.

The residual β -delayed protons were subtracted following the same technique. The background produced by the presence of ^{12}C in the target was measured using a pure carbon target with equivalent thickness and was also subtracted. Then, the proton spectrum was converted to the CM excitation function by using a Monte-Carlo algorithm taking into account the energy resolution of the detectors and energy loss in the target. An overall energy resolution of 15 keV FWHM was obtained.

The excitation function obtained (see Fig. 6.15) shows at energies higher than 1.5 MeV several resonances reflecting the ^{18}Na compound nucleus structure. The position of these resonances is related to the energy of the excited states in the compound nucleus and their widths and shapes provide information on lifetimes (and spectroscopic factors) and spin-parity respectively. Spectroscopic properties of the

low-lying states in ^{18}Na can be extracted using an R-matrix analysis of the measured excitation function. In order to perform this analysis, it is essential to find good initial conditions for the fit. For this, we used the properties predicted by the shell model (see Tab. 6.3). A fit with the R-matrix code Anar χ [137] was performed with energies and widths for the resonances as free parameters. The best fit obtained in this analysis is presented in Fig. 6.15, with energies and widths of the resonances shown in Tab. 6.3.

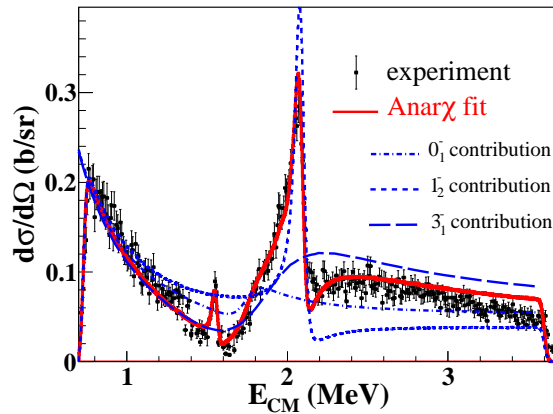


Figure 6.15: Measured excitation function of the $H(^{17}\text{Ne},p)^{17}\text{Ne}$ reaction presented as a function of CM energy. It is measured between 5 and 20 degrees (LAB) and reconstructed at 180 degrees in the CM. Lines show R-matrix calculations based on the properties of the states given in Table 6.3. The continuous line is degraded by the energy resolution of the experiment. Three individual contributions are shown with discontinuous lines.

6.4.3 Results

It is interesting to note that our results are in contradiction with the predictions of Ref. [127] where the two broad s-wave states have much higher energies (higher than 3.5 MeV). We also note the absence of a peak located at low energy and corresponding to the 1^- ground state. As the energy resolution was 13 keV FWHM in the CM, there are two possibilities: either (i) the 1^- ground state and the 2^- first excited state of ^{18}Na could not be resolved, this means that both states are narrow and the energy difference between the two states is lower than 5 keV or, (ii) the 1^- state is so narrow that it is not visible. The latter would be in agreement with shell-model calculations. Also, the 2_2^- state is not visible in our spectrum, meaning that its width is very small, in agreement with the predictions. It might appear surprising to have such narrow states in an unbound nucleus located beyond the proton drip-line but the lifetime is increased by the effect of the Coulomb barrier and the structure of the state. Indeed, the overlap of the ^{18}Na (1_1^- or 2_2^-) state with the ^{17}Ne ground state is very small ($\theta^2=0.086$ and $\theta^2=0.004$). The ground state of ^{18}Na (if 1_1^-) is mainly constructed on the first excited state of $^{17}\text{Ne}^*(3/2^-)$. Few events of multiplicity 2, or more, were observed in our experimental data supporting the assumption of a low contribution from inelastic scattering. Our results are summarised in the level scheme of Fig. 6.16

The properties of ^{18}Na , ^{19}Mg and its two-proton radioactivity were predicted by L. Grigorenko *et al* [127] using a three-body model based on the ground state of ^{17}Ne . Concerning low-lying states of ^{18}Na , the

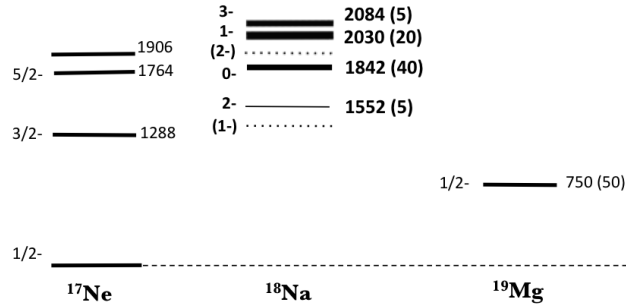


Figure 6.16: States observed in ^{18}Na and in the framework of ^{17}Ne ground state. Decay energies are given in keV relative to the respective $1p$ and $2p$ thresholds. Dotted lines correspond to very narrow states that were not observed.

predictions are not in agreement with the properties measured in this experiment. We observed s -wave states at much lower energies than predicted. An increase of the s^2 component in the ^{19}Mg ground state would have the effect of strongly reducing the two-proton emission lifetime, which would be inconsistent with the experimental value. However, if ^{18}Na ground state is built mainly on the first excited state of ^{17}Ne , then it should also be the case with the ground state of ^{19}Mg . This fact was not taken into account in ref. [127] and could be the solution to the lifetime problem.

It is interesting to estimate the half-life of ^{19}Mg using the quasi-classical R-matrix type model of Grigorenko and Zhukov from Ref. [138] which is known to give results close to those obtained with a three-body model. The main contributions arise through the broader resonances in ^{18}Na , that are $\ell = 0$ decays, so mainly from the 0_1^- state ($\Gamma_2=300$ keV) and from the 1_2^- state ($\Gamma_2=900$ keV). The calculated shell-model spectroscopic factors of ^{19}Mg are: $\theta^2 \left(|^{18}\text{Na}_{(0_1^-)}\rangle \otimes |\pi 2s_{1/2}\rangle \right) = 0.0956$ and $\theta^2 \left(|^{18}\text{Na}_{(1_2^-)}\rangle \otimes |\pi 2s_{1/2}\rangle \right) = 0.24$. The estimated partial decay widths via separate isolated s -wave configurations are 1.5×10^{-10} MeV ($\tau=3.1$ ps) for the 0^- and 6.8×10^{-10} MeV ($\tau=0.67$ ps) for the 1_2^- . The second width exceeds the total experimental width of $\Gamma_{exp} = 1.14 \times 10^{-10}$ MeV by a factor of 6. This difference could easily be corrected with a smaller s -wave spectroscopic factor of ^{19}Mg than the one calculated with the shell model. Therefore, it seems possible to understand in a complete and consistent way the low-lying states of ^{18}Na and the radioactivity of ^{19}Mg . This conclusion could be confirmed with a more sophisticated three-body model calculation.

6.4.4 Conclusion

The measurement of the resonant elastic scattering reaction $p(^{17}\text{Ne},p)^{17}\text{Ne}$ allowed us to obtain the spectroscopic properties of four low-lying states in the unbound nucleus ^{18}Na and suggests the presence of two very narrow states including a ground state located well above the ^{19}Mg ground state. This measurement has been possible thanks to the development of an intense and pure radioactive beam of ^{17}Ne at GANIL. Although the experimental results differ from previous theoretical predictions, they are in good agreement with the calculations based on shell model presented in this article. The main difference arise from two s -wave states observed at much lower energies than previously predicted, about 1.5 MeV below. Half-life of the ^{19}Mg two-proton radioactivity was calculated using a simple quasi-classical R-matrix

model and the measured properties of ^{18}Na , and also using shell model predictions for the structure of ^{19}Mg . The calculated value is not in agreement with the experimental value. This difference might be due to a slightly incorrect shell model prediction, or from the fact that our model is too simple.

If the observed difference is applied to the inverse reaction, this study shows that the calculations of the astrophysical two-proton capture reaction should be reliable within a factor 10.

This work was the subject of the Marlène Assié post-doc, and was published in Ref. [139]. This study was also the subject of the Master thesis of Mr. Tarek AL KALANEE (a former student of mine).

6.5 ^{16}F : New pathway to bypass the ^{15}O waiting point (E442S) Probing Nuclear forces beyond the drip-line

6.5.1 Motivations

New pathway The proton-unbound nuclei ^{15}F and ^{16}F play an important role in X-ray bursts. In these explosive events, the carbon and nitrogen elements are mainly transformed into ^{14}O and ^{15}O by successive proton captures [140, 141]. Then, the pathway for new proton captures is hindered by the proton-unbound nuclei ^{15}F and ^{16}F . The reaction flux and the energy generation are then limited by the relatively slow β^+ -decay of ^{14}O ($t_{1/2}=71$ s) and ^{15}O ($t_{1/2}=122$ s), which create waiting points. The sudden and intense release of energy observed in X-ray bursts requires to circumvent the limited energy generation in breakout reactions. The $^{15}\text{O}(\alpha,\gamma)^{19}\text{Ne}$ reaction is considered to be one of the key reactions in this context [140, 141]. It makes the transition into the nucleosynthetic *rp* process (rapid proton capture) which is responsible for an increased rate of energy generation and the synthesis of heavier elements [142]. In such explosive environments, ^{16}F is strongly populated in the ground state (g.s.) or in the first excited state, and leads to an equilibrium between formation and decay of this proton-unbound nucleus. From time to time before the proton is emitted, ^{16}F can capture another proton thus producing the ^{17}Ne particle stable isotope [113]. This two-proton capture process was calculated to be significant for extreme densities. Here, β^+ -decay of ^{16}F to ^{16}O is proposed as an alternative channel. Two reactions channels $^{15}\text{O}(p,\beta^+)^{16}\text{O}$ and $^{15}\text{O}(p,\gamma)(\beta^+)^{16}\text{O}$ are studied. Both reactions eventually proceed through the β^+ -decay of the intermediate unbound ^{16}F g.s., which is fed directly by a proton capture or indirectly through a proton capture to the first excited state followed by a γ -emission. This is the first time that a $(p,\gamma)(\beta^+)$ reaction is proposed, which is a sequence of reactions that involves an intermediate unbound nucleus. When the γ -decay occurs to the low energy wing of the ^{16}F g.s. resonance the subsequent proton emission is dramatically hindered due to the fact that the low energy proton has to tunnel through the Coulomb potential of the ^{15}O nucleus. The calculation of these reaction cross sections requires the measurement of the energies, widths, spins and parities of the low lying states of ^{16}F .

Nuclear forces Theoretical description of particle-unbound nuclei in the framework of open quantum systems is a challenge to basic nuclear research [143]. In such systems, the coupling to the scattering continuum may lead to the modification of the *effective* interactions [144] and a further reordering of the shells [145]. The identification and understanding of the role of specific parts of the nuclear forces [145] in stabilising atomic nuclei and inducing shell evolutions is a central theme of nuclear physics [146]. This understanding would bring a better predictive power for exotic nuclei such as those involved in the explosive *r-process* nucleosynthesis or X-ray bursters where relevant spectroscopic information is not yet

available [147]. A good way to shed light on the effect of the continuum is to compare level schemes of mirror nuclei involving a bound and an unbound nucleus. The asymmetries observed between the mirror nuclei, the so-called Thomas-Ehrman shifts [148, 149], can be used to single out the role of nucleon-nucleon interaction.

An ideal case to study the effect of the continuum can be found in the mirror systems: *unbound* ${}^1_9\text{F}_7$ and the *bound* ${}^1_7\text{N}_9$ nuclei [150]. We shall use their measured properties to derive the proton-neutron interaction energies in the unbound ${}^{16}\text{F}$ nucleus and to determine the role of the continuum in changing effective interactions in mirror nuclei.

6.5.2 Experiment

Several nuclei were studied through the measurement of elastic scattering excitation functions. Four different beams were used in this experiment: the two radioactive beams of ${}^{15}\text{O}$ and ${}^{14}\text{O}$ for the study of ${}^{16}\text{F}$ and ${}^{15}\text{F}$, and the two stable beams ${}^{14}\text{N}$ and ${}^{15}\text{N}$ for the calibrations. Radioactive ${}^{15}\text{O}^{1+}$ ions were produced at the SPIRAL facility at GANIL through the fragmentation of a 95 AMeV ${}^{16}\text{O}$ primary beam impinging on a thick carbon production target. They were post-accelerated by means of the CIME cyclotron up to the energy of 1.2 AMeV, the lowest energy available at this accelerator. Intense (several nAe) stable ${}^{15}\text{N}^{1+}$ and molecular $({}^{14}\text{N}{}^{16}\text{O})^{2+}$ beams came along with the radioactive beam of interest. The selection of one of these species was obtained by using a vertical betatron selection device [151] located inside the cyclotron, and by choosing the suitable magnetic rigidity of the LISE spectrometer [152] after the nuclei have traversed a $38 \mu\text{g}/\text{cm}^2$ carbon stripper foil located at the object focal point of LISE. It was possible to obtain an ${}^{15}\text{O}^{6+}$ beam with an intensity of $1.0(2)\times 10^6$ pps and 97(1) % purity, or one of two stable beams of ${}^{15}\text{N}^{6+}$ or ${}^{14}\text{N}^{6+}$ with 10^8 pps and 100 % purity. The selected ions were sent onto a thick polypropylene $(\text{CH}_2)_n$ target in which they were stopped. Some ions underwent proton elastic scattering and the scattered protons were detected promptly to the reaction in a $E(300 \mu\text{m})$ silicon detector that covered an angular acceptance of $\pm 1^\circ$ downstream the target. Resonances in the compound nucleus ${}^{16}\text{F}$ were studied through the analysis of the scattered protons spectrum obtained with the ${}^{15}\text{O}$ beam. Stable beams of ${}^{14}\text{N}$ and ${}^{15}\text{N}$ were used for calibration purposes to measure the elastic scattering reactions ${}^1\text{H}({}^{14}\text{N},\text{p}){}^{14}\text{N}$ and ${}^1\text{H}({}^{15}\text{N},\text{p}){}^{15}\text{N}$ in the same experimental conditions. Energy calibrations and resolutions were measured by populating known resonances in the compound nucleus ${}^{15}\text{O}$ and in the compound nucleus ${}^{16}\text{O}$. In the same manner, radioactive ${}^{14}\text{O}$ ions were produced with the intensity of $1.9(1)\times 10^5$ pps and post-accelerated to 6 AMeV. The isobaric contamination of the beam was reduced down to 0.0(1) %. Scattered protons were detected in $\Delta E(500 \mu\text{m})$ - $E(6 \text{ mm cooled SiLi})$ silicon detectors that covered an angular acceptance of $\pm 2.16^\circ$. Resonances in the ${}^{15}\text{F}$ compound nucleus were studied through the analysis of the proton spectrum. A pure ${}^{14}\text{N}^{6+}$ beam accelerated to 6 AMeV was used for calibrations. The energy resolution of the measured scattered protons can be determined by the relation: $\sigma_{\text{Lab}} = \sqrt{\sigma_{\text{det}}^2 + \sigma_{\theta}^2 + \sigma_{\text{strag}}^2}$, where σ_{det} is the energy resolution of the detector that is $\sigma_{\text{det}}=9$ keV (20 keV) in the ${}^{15}\text{O}$ (${}^{14}\text{N}$) setting, σ_{strag} is the energy straggling in the target that is estimated to be lower than 5 keV from simulations, and σ_{θ} is the energy resolution due to the aperture $d\theta$ of the detector. In inverse kinematics it can be derived that $\sigma_{\theta} = \tan(\theta)Ed\theta$. Therefore the degradation in energy resolution is minimal when $\theta = 0^\circ$. For this reason, and for maximizing the ratio between the nuclear and the Coulomb contribution of the differential cross-section, the scattered protons were measured at forward angles. An energy resolution of $\sigma_{\text{Lab}} = 10$ keV was measured in the case of ${}^{16}\text{F}$, which leads to $\sigma_{\text{CM}} \simeq$

Table 6.4: Measured energies, widths and deduced spectroscopic factors C^2S for the low-lying states in ^{16}F . The new recommended separation energy is $S_p = -535 \pm 5$ keV. The spectroscopic factors are calculated using the method proposed in Ref [155].

| Ref. [155] | | | Ref [156] | This work | | New Recommended | | |
|--------------|---------|------------------|------------------|--------------|------------------|-----------------|------------------|---------|
| E_x (keV) | J^π | Γ_p (keV) | Γ_p (keV) | E_x (keV) | Γ_p (keV) | E_x (keV) | Γ_p (keV) | C^2S |
| 0 | 0^- | 22.8 ± 14.4 | 18 ± 16 | 0 | 25 ± 5 | 0 | 25.6 ± 4.6 | 1.1(2) |
| 187 ± 18 | 1^- | 103 ± 12 | 87 ± 16 | 198 ± 10 | 70 ± 5 | 194 ± 5 | 76 ± 5 | 0.91(8) |
| 416 ± 20 | 2^- | 4.0 ± 2.5 | 16 ± 16 | 425 ± 2 | 6 ± 3 | 424.8 ± 1.9 | 5.0 ± 2.0 | 1.2(5) |
| 722 ± 16 | 3^- | 15.1 ± 6.7 | 12 ± 16 | | | 721 ± 4 | 15.1 ± 6.7 | 1.0(5) |

3 keV in the center of mass, and $\sigma_{CM} \simeq 7$ keV in the case of ^{15}F .

6.5.3 Results

The measured scattered protons spectra of $^1\text{H}(^{15}\text{O},p)^{15}\text{O}$ and $^1\text{H}(^{14}\text{O},p)^{14}\text{O}$ were transformed into the center of mass excitation functions by taking into account the energy losses, the energy and angular straggling, the intrinsic energy resolution and the angular acceptance of the Si detectors. This procedure was successfully tested using the $^1\text{H}(^{14}\text{N},p)^{14}\text{N}$ and $^1\text{H}(^{15}\text{N},p)^{15}\text{N}$ reactions (see the upper part of Fig. 6.17). As the lowest excited states in ^{15}O and ^{14}O lie above 5.1 MeV, inelastic scattering do not contribute to the reaction with ^{14}O , and is expected to be negligible in the case of ^{15}O .

The spectra corresponding to ^{16}F and ^{15}F are shown in the lower part of Fig.6.17. They were fitted using the R-matrix formalism with the code Anar χ [137]. The shape and height of the peaks are used to derive the energy, J^π and width of the resonances. The uniqueness of the solution was controlled carefully. Two broad resonances are found at $S_p = -1.31(1)$ MeV, $\Gamma_R = 853(146)$ keV, $J^\pi = 1/2^+$ and $E_R = 2.78(1)$ MeV, $\Gamma_R = 311(10)$ keV, $J^\pi = 5/2^+$ in ^{15}F . Energies and widths of these resonances are consistent with previous results having larger uncertainties [153, 154]. Three resonances corresponding to the 0^- , 1^- and 2^- states in ^{16}F were identified. Their energy and width are given in Table 6.4. A proton separation energy $S_p = -534 \pm 5$ keV was obtained, in agreement with the value $S_p = -536 \pm 8$ keV recommended both in the compilation [31] and the recent measurement $S_p = -535$ keV [155]. Conversely, the observed width of the 1^- resonance, 70 ± 5 keV, differs significantly with the recommended value of < 40 keV or with the recent experimental value of 103 ± 12 keV [155], and is in good agreement with the most recent measurement of 87 ± 16 keV [156]. New recommended weighted mean values are proposed in Table 6.4 for the three resonances, while the properties of the $J^\pi = 3^-$ state are taken from Ref. [155]. The measured widths Γ_p^{exp} of resonances are related to the spectroscopic factors C^2S through the relation $\Gamma_{exp} = C^2S \Gamma_{sp}$, where Γ_{sp} are the calculated single-particle widths [155]. As shown in Table 6.4, the measured spectroscopic factors of the low-lying states in ^{16}F are all close to 1. It is also the case in the mirror nucleus ^{16}N [157, 158].

6.5.4 Interpretation

New pathway The calculation of the $^{15}\text{O}(p,\beta^+)^{16}\text{O}$ cross section was made in the same way as the $p(p,\beta^+)d$ reaction (see Section 6.2 about the $pp1$ reaction). The properties of the ^{16}F g.s. resonance measured in the present work were used. We also used the Breit-Wigner formula for a single-level

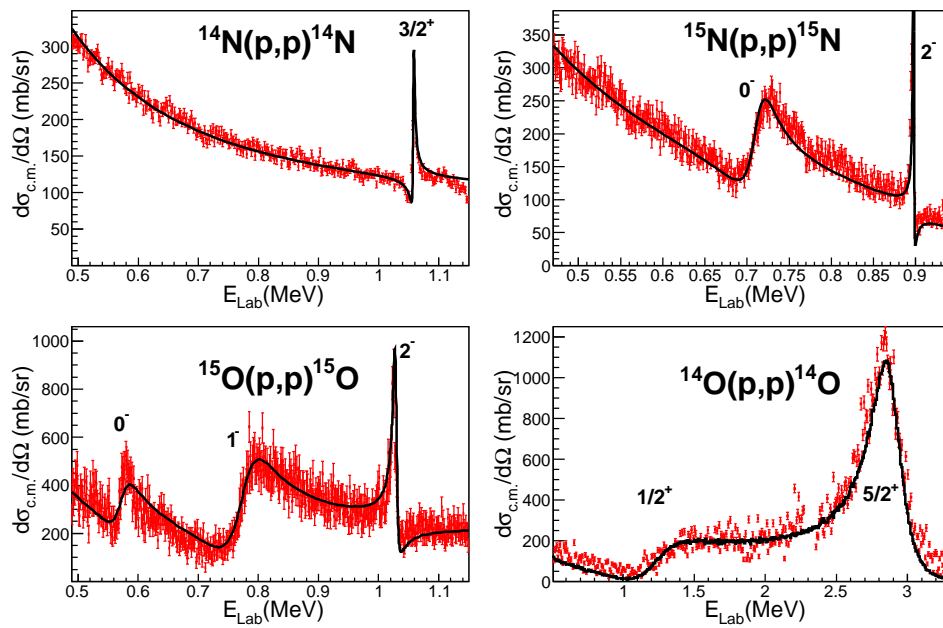


Figure 6.17: Measured excitation functions of proton resonant elastic scattering on the ^{14}N , ^{15}N , ^{15}O and ^{14}O nuclei. The differential cross sections measured at 180° in the CM are shown as a function of the laboratory energy E_{Lab} . Several resonances in the compound nuclei ^{15}O , ^{16}O , ^{16}F and ^{15}F can be observed. The lines are results of the R-matrix calculations using the parameters from Ref. [159] for the ^{15}O and ^{16}O nuclei, and from Table 6.4 for the ^{16}F nucleus, and from this work for the two resonances observed in ^{15}F .

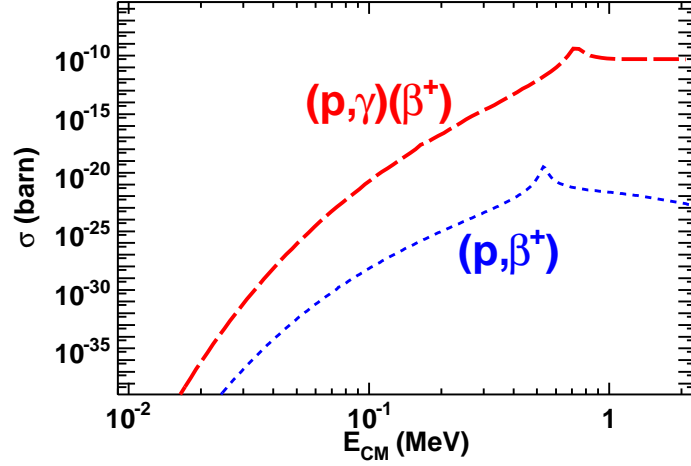


Figure 6.18: Calculated $^{15}\text{O}(p, \beta^+)^{16}\text{O}$ and $^{15}\text{O}(p, \gamma)(\beta^+)^{16}\text{O}$ cross sections are shown as a function of the c.m. energy.

resonance [120]:

$$\sigma(E_p) = \pi \tilde{\lambda}^2 \frac{2J_r + 1}{(2J_i + 1)(2J_f + 1)} \frac{\Gamma_{in} \Gamma_{out}}{(E_p - E_R)^2 + (\frac{\Gamma_{Tot}}{2})^2} \quad (6.21)$$

where $\tilde{\lambda}$ is the de Broglie wavelength, J are the spins, and $E_R, \Gamma_{Tot}, \Gamma_{in}, \Gamma_{out}$ being the resonance energy, total width, and partial widths of the incoming and outgoing channels. In the (p, β^+) case, $E_R = E_{g.s.}$ the energy of the g.s. resonance, $\Gamma_{in} = \Gamma_p^{g.s.}$ the proton width, and $\Gamma_{out} = \Gamma_\beta$ corresponds to the β^+ -decay partial width. The energy dependence of the proton width $\Gamma_p^{g.s.}(E_p)$ for the incoming channel was taken into account using the relation:

$$\Gamma_p^{g.s.}(E_p) = \Gamma_p^{g.s.}(E_{g.s.}) \frac{P(E_p)}{P(E_{g.s.})} \quad (6.22)$$

where $\Gamma_p^{g.s.}(E_{g.s.})$ is the proton width at the resonance energy and $P(E_p)$ is the penetrability function under the Coulomb potential barrier. A partial lifetime for $^{16}\text{F}(\beta^+)$ of 1 second and a negligible branching ratio to the $^{15}\text{O}(p, \beta^+)^{12}\text{C} + \alpha$ final decay channel were assumed. The β^+ -decay partial width was taken as a constant since the energy dependence of the Fermi function is small due to large Q_{β^+} value ($Q_{\beta^+} = 15417(8)$ keV [31]). The calculated $^{15}\text{O}(p, \beta^+)^{16}\text{O}$ cross section is shown in Fig. 6.18 as a function of the c.m. energy. The maximum of the cross section is observed at the energy of 534 keV corresponding to the ^{16}F g.s. resonance. At this energy the (p, β^+) cross section is very small, about 10^{-20} barns, since ^{16}F mainly decays by proton emission, which is $\simeq 10^{20}$ times faster than the β^+ -decay (since $\Gamma_p^{g.s.}(E_{g.s.}) = 25$ keV and $\Gamma_\beta = 0.66 \cdot 10^{-18}$ keV).

The calculation of the $^{15}\text{O}(p, \gamma)(\beta^+)^{16}\text{O}$ reaction was performed sequentially, a schematic representation of this reaction is shown in Fig. 6.19. Proton capture reaction to the first excited state of ^{16}F is considered, followed by a γ decay to the g.s. resonance, from which a β^+ -decay branching ratio is taken into account. The cross section $\sigma_{p\gamma\beta}(E_p)$ for the $(p, \gamma)(\beta^+)$ reaction at the energy E_p is an integration of the differential

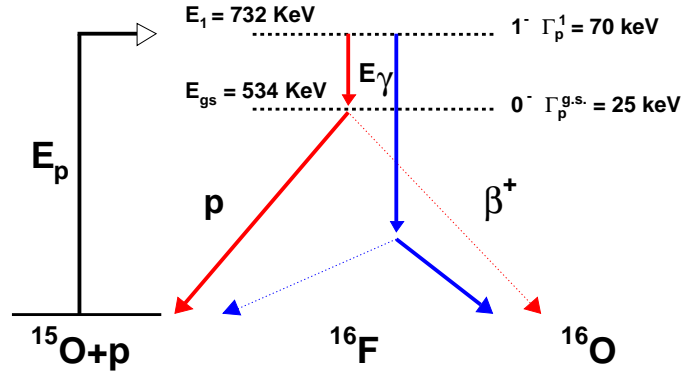


Figure 6.19: Schematic representation of the $^{15}\text{O}(p,\gamma)(\beta^+)^{16}\text{O}$ reaction (see text). Two cases are represented. In red, γ -transitions populate the ^{16}F g.s. at the resonance energy. In that case, ^{16}F mainly decays by proton emission. In blue, high energy γ -transitions populate the low energy wing of the g.s. resonance. In that case, β^+ -decay dominates.

cross section over all possible energies of the γ transition (since the g.s. has a large width):

$$\sigma_{p\gamma\beta}(E_p) = \int \sigma_{p\gamma}(E_p, E_\gamma) P_\gamma(E_\gamma) P_\beta(E_p, E_\gamma) dE_\gamma \quad (6.23)$$

where $\sigma_{p\gamma}(E_p, E_\gamma)$ is the cross section to capture the proton at the energy E_p and to emit a γ -ray with an energy E_γ , $P_\gamma(E_\gamma)dE_\gamma$ is the strength function [160], that is the probability for the γ -ray to have an energy between E_γ and $E_\gamma+dE_\gamma$, and $P_\beta(E_p, E_\gamma)$ is the branching ratio function for the ^{16}F nucleus to decay by β^+ -ray emission. The first term $\sigma_{p\gamma}(E_p, E_\gamma)$ is calculated using a Breit-Wigner formula with the following parameters E_1 , $\Gamma_{Tot}^1(E_p, E_\gamma)$, $\Gamma_p^1(E_p)$, $\Gamma_\gamma^1(E_\gamma)$ being the energy, total width, proton width and γ width for the resonance corresponding to the first excited state of ^{16}F . The γ -ray is emitted from a 1^- state to the 0^- g.s., which corresponds to a M1 transition, whose energy dependence of the γ width $\Gamma_\gamma^1(E_\gamma)$ is:

$$\Gamma_\gamma^1(E_\gamma) = \Gamma_\gamma^1(E_1 - E_{g.s.}) \left\{ \frac{E_\gamma}{E_1 - E_{g.s.}} \right\}^3 \quad (6.24)$$

A γ -transition lifetime of 1 ps was obtained from the mirror nucleus [161], which corresponds to the partial width $\Gamma_\gamma^1(E_1 - E_{g.s.}) = 0.66 \cdot 10^{-3} eV$. The strength function of the ^{16}F g.s. resonance was calculated assuming a Breit-Wigner parametrization:

$$P_\gamma(E_\gamma)dE_\gamma = \frac{1}{N} \frac{dE_\gamma}{(\Delta E)^2 + \left(\frac{\Gamma_{Tot}^{g.s.}(E_p - E_\gamma)}{2} \right)^2} \quad (6.25)$$

and the normalization constant is:

$$N = \int \frac{1}{(\Delta E)^2 + \left(\frac{\Gamma_{Tot}^{g.s.}(E_p - E_\gamma)}{2} \right)^2} dE_\gamma \quad (6.26)$$

with $\Delta E = E_p - E_\gamma - E_{g.s.}$ and $\Gamma_{Tot}^{g.s.}(E_p - E_\gamma) = \Gamma_\beta + \Gamma_p^{g.s.}(E_p - E_\gamma)$ is the total width of the g.s. resonance. The β branching ratio is calculated using:

$$P_\beta(E_p, E_\gamma) = \frac{\Gamma_\beta}{\Gamma_\beta + \Gamma_p^{g.s.}(E_p - E_\gamma)} \quad (6.27)$$

Naively, one might have expected to obtain a small cross section for the $(p, \gamma)(\beta^+)$ reaction, similar to the (p, β^+) one, since γ - and β -widths are much smaller than proton-widths. Contrary to naive expectations, the $(p, \gamma)(\beta^+)$ cross section is about 10^{10} times larger than the (p, β^+) cross section, as shown in Fig. 6.18. The large ratio can be explained in the following way. As it has been shown previously, there is only one (p, β^+) reaction for 10^{20} (p, p) reactions. In the $(p, \gamma)(\beta^+)$ case, one γ -ray is emitted for 10^8 incident protons (from the ratio of the widths) and about one γ -transition over 10^3 populates the low energy wing of the g.s. resonance (less than 15 keV above the proton-emission threshold) where it is almost always followed by a β^+ -decay ($P_\beta \simeq 1$). This implies that one incident proton over 10^9 induces a $(p, \gamma)(\beta^+)$ reaction, that is a factor 10^9 times larger than in the (p, β^+) reaction. This is the main explanation of the large factor between the $(p, \gamma)(\beta^+)$ and the (p, β^+) reaction cross sections.

In the following, uncertainties in the calculations and their evaluated effects on the results are discussed. The position and width of the low lying ^{16}F states were measured with a high precision (see Table 6.4). The effect of the uncertainties in these measured parameters results in a change by less than a factor of 2 in the calculated cross sections. The calculated $(p, \gamma)(\beta^+)$ cross section is insensitive to the ^{16}F β^+ -decay lifetime, as a variation by a factor of 100 causes the cross section to change by only a factor of 2. The lifetime of the γ -transition is a sensitive parameter since the $(p, \gamma)(\beta^+)$ cross section is almost directly proportional to this parameter. A value measured in the mirror nucleus was used, but this assumption works only to within a factor of 10 [55]. The other excited states in ^{16}F were also studied and found to be negligible.

The obtained reaction rates are shown in Fig. 6.20 (a) as a function of the temperature. The rate of the (p, β^+) reaction is negligible compared to that of the reaction $(p, \gamma)(\beta^+)$ at all temperatures. To evaluate the impact of this latter reaction, it has to be compared with the competing β^+ -decay of ^{15}O and the $^{15}\text{O}(\alpha, \gamma)^{19}\text{Ne}$ alpha capture reaction. Fig. 6.20 (b) shows the temperature and density conditions where the $(p, \gamma)(\beta^+)$ reaction represents 10 to 50 % of the total reaction flux initiated by the ^{15}O nucleus. Boxes delimit conditions where novae and X-ray bursts might happen. For the lowest temperatures ($< 10^8$ K), the $(p, \gamma)(\beta^+)$ reaction requires extreme densities ($> 10^{10}$ g cm $^{-3}$) to compete with the $^{15}\text{O}(\beta^+)$ -decay. For the highest temperatures ($> 1.1 \cdot 10^9$ K), the (α, γ) reaction always dominates. In X-ray bursts, the $(p, \gamma)(\beta^+)$ reaction might represent up to 30 % of the total flux. Within the uncertainties of the calculations, the $(p, \gamma)(\beta^+)$ reaction could be faster than the (α, γ) reaction for temperatures up to 10^9 K. A more precise evaluation depends on the (α, γ) reaction rate (not well known) and on the relative abundances in hydrogen and helium, since one reaction consumes protons and the other alpha particles. In these extreme conditions, a new cycle of reactions is operating: $^{15}\text{O}(p, \gamma)(\beta^+)^{16}\text{O}(p, \gamma)^{17}\text{F}(p, \gamma)^{18}\text{Ne}(\beta^+)^{18}\text{F}(p, \alpha)^{15}\text{O}$. This new cycle could speed-up the CNO cycle and occur complementary to breakout reactions. The role of this new proposed cycle of reactions remains to be studied more carefully under various X-ray bursts conditions. Moreover, high temperature and density environments would correspond to conditions where the alternative $^{16}\text{F}(p, \gamma)^{17}\text{Ne}$ reaction might be competitive with the temperature independent $^{16}\text{F}(\beta^+)^{16}\text{O}$ decay. The $^{15}\text{O}(p, \gamma)(p, \gamma)^{17}\text{Ne}$ cross section was estimated using the same formalism as used for the $(p, \gamma)(\beta^+)$ reaction. The first reaction was found to compete with the second in X-ray bursts conditions. However, these calculations are only a first estimate since hitherto unknown widths of the excited states in ^{17}Ne are used.

Nuclear force The comparison of the two level schemes of the mirror nuclei ^{16}N and ^{16}F is shown in Fig.

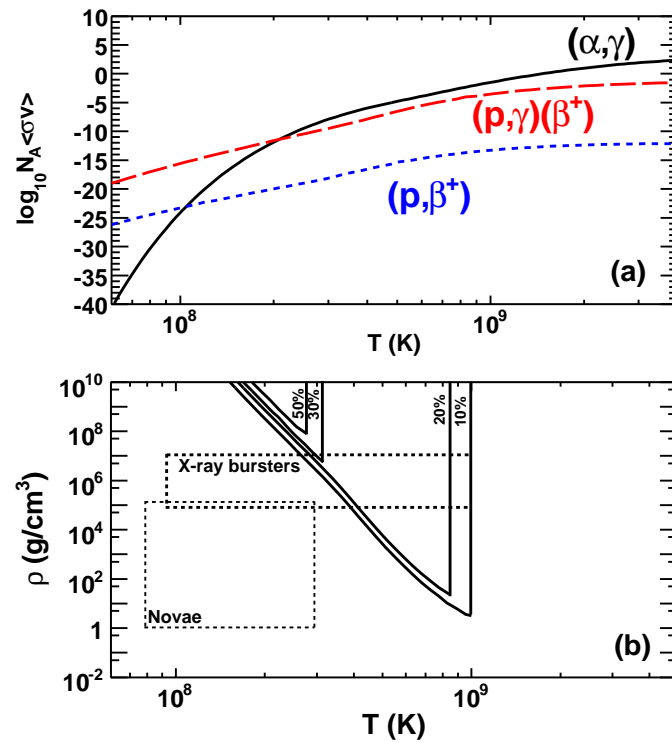


Figure 6.20: (a) $^{15}\text{O}(p, \beta^+)^{16}\text{O}$ and $^{15}\text{O}(p, \gamma)(\beta^+)^{16}\text{O}$ reaction rates are shown as a function of the temperature. The $^{15}\text{O}(\alpha, \gamma)^{19}\text{Ne}$ reaction rate is also shown for comparison. (b) Density versus temperature conditions where the $^{15}\text{O}(p, \gamma)(\beta^+)^{16}\text{O}$ reaction represents 10 to 50 % of the total reaction flux initiated by the ^{15}O nucleus.

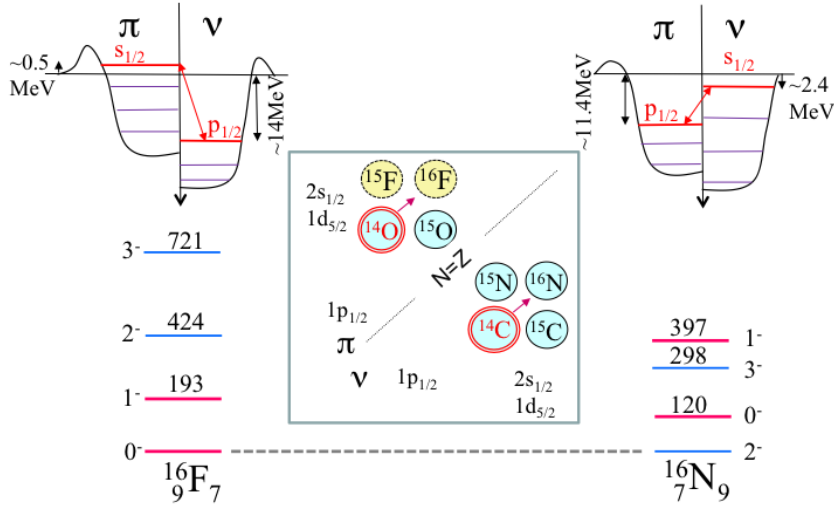


Figure 6.21: Schematic view of the valence proton (π) and neutron (ν) orbits involved in the mirror systems $^{16}_9\text{F}_7$ and $^{16}_7\text{N}_9$ on top of the $^{14}_8\text{O}_6$ and $^{14}_6\text{C}_8$ core nuclei. The major difference between these two systems is that the proton $2s_{1/2}$ or $1d_{5/2}$ (not shown) orbits are unbound in $^{16}_9\text{F}_7$. The level schemes of the two mirror nuclei differ significantly, as shown in the bottom part of the figure.

6.21. Large differences can be observed: the ground state of ^{16}F has 0^- while that of ^{16}N has 2^- , and the two 0^- and 1^- states are down shifted in energy relatively to the other states by more than 500 keV.

In these odd-odd nuclei, a good approach is to use a core plus two nucleons model. The first excited states of the $^{16}_7\text{N}_9$ nucleus can be well described using a single-particle description with a closed core of ^{14}C plus a deeply bound proton in the $1p_{1/2}$ orbital ($S_p(^{15}\text{N})=+10.2$ MeV) plus a neutron in the $2s_{1/2}$ orbital ($S_n(^{15}\text{C})=+1.22$ MeV), leading to $J^\pi=0^-, 1^-$ states, or plus a neutron in the $1d_{5/2}$ orbital ($S_n(^{15}\text{C}^*)=+0.48$ MeV), leading to $J^\pi=2^-, 3^-$ states (see Fig. 6.21). In the same way, $(0,1)^-$ and $(2,3)^-$ states in ^{16}F can be described as a ^{14}O core plus a neutron in the $1p_{1/2}$ orbital ($S_n(^{15}\text{O})=+13.22$ MeV) plus a proton in the $2s_{1/2}$ orbital ($S_p(^{15}\text{F})=-1.31$ MeV) or plus a proton in the $1d_{5/2}$ orbital ($S_p(^{15}\text{F}^*)=-2.78$ MeV). This simplified single particle view is justified as the spectroscopic factor values of the systems ($^{15}\text{N} = ^{14}\text{C} + p$), ($^{15}\text{F} = ^{14}\text{O} + p$) and ($^{15}\text{C} = ^{14}\text{C} + n$) are close to unity [161, 162, 157, 153]. In this framework, the experimental neutron-proton (n-p) *effective* interactions elements in ^{16}N , labeled $\text{Int}_{^{16}\text{N}}^{\text{exp}}(J)$, can be extracted from the experimental binding energies (BE) as in Ref. [163]:

$$\text{Int}_{^{16}\text{N}}^{\text{exp}}(J) = \text{BE}(^{16}\text{N})_J - \text{BE}(^{16}\text{N}_{\text{free}}).$$

In this expression $\text{BE}(^{16}\text{N}_{\text{free}})$ corresponds to the binding energy of the $^{14}\text{C}+1p+1n$ system without residual interaction between the proton and the neutron. In the case of the $J^\pi=0^-$ and 1^- states:

$$\text{BE}(^{16}\text{N}_{\text{free}}) = \text{BE}(^{14}\text{C})_{0^+} + \text{BE}(\pi 1p_{1/2}) + \text{BE}(\nu 2s_{1/2})$$

where

$$\text{BE}(\pi 1p_{1/2}) = \text{BE}(^{15}\text{N})_{1/2^-} - \text{BE}(^{14}\text{C})_{0^+}$$

$$\text{BE}(v2s_{1/2}) = \text{BE}(^{15}\text{C})_{1/2^+} - \text{BE}(^{14}\text{C})_{0^+}$$

Combining these equations, we obtain:

$$\text{BE}(^{16}\text{N}_{\text{free}}) = \text{BE}(^{15}\text{C})_{1/2^+} + \text{BE}(^{15}\text{N})_{1/2^-} - \text{BE}(^{14}\text{C})_{0^+}$$

The same method has been also applied to obtain the $J^\pi=2^-, 3^-$ states originating from the n-p coupling $\pi 1p_{1/2} \otimes v 1d_{5/2}$. The obtained experimental n-p interaction energies $\text{Int}_{^{16}\text{N}}^{\text{exp}}$ and $\text{Int}_{^{16}\text{F}}^{\text{exp}}$ are given in Table 6.5.

Table 6.5: Experimental proton-neutron interaction energies, $\text{Int}_{^{16}\text{N}}^{\text{exp}}$ and $\text{Int}_{^{16}\text{F}}^{\text{exp}}$, derived for the $J^\pi = 0^-, 1^-$ [$1p_{1/2} \otimes 2s_{1/2}$] and $J^\pi = 2^-, 3^-$ [$1p_{1/2} \otimes 1d_{5/2}$] states in ^{16}N and ^{16}F . Calculated interaction energies $\text{Int}_{^{16}\text{F}}^{\text{over}}$ and $\text{Int}_{^{16}\text{F}}^{\text{over+C}}$ are based on the interactions derived for ^{16}N to which the effects of the change in wave functions overlaps (over) between mirror nuclei and the change in Coulomb (over+C) energy have been added (see text for details).

| State (J) | $\text{Int}_{^{16}\text{N}}^{\text{exp}}$ | $\text{Int}_{^{16}\text{F}}^{\text{over}}$ | $\text{Int}_{^{16}\text{F}}^{\text{over+C}}$ | $\text{Int}_{^{16}\text{F}}^{\text{exp}}$ |
|-----------|---|--|--|---|
| 0^- | -1.151 | -0.943 | -0.775 | -0.775 |
| 1^- | -0.874 | -0.716 | -0.581 | -0.577 |
| 2^- | -2.011 | -2.031 | -1.842 | -1.829 |
| 3^- | -1.713 | -1.730 | -1.574 | -1.523 |

While the effective interactions of the $J^\pi=0^-, 1^-$ states differ by as much as 40% in the mirror systems, the interaction energies of the $J^\pi=2^-, 3^-$ states differ only by 10%, despite the fact that the proton $1d_{5/2}$ orbit is less bound than the $2s_{1/2}$ one by about 1.5 MeV.

Hereafter, we show that these changes of n-p effective interactions can be explained by the effect of the coupling with continuum which leads both to a change in the spatial overlap of the neutron and proton wave functions and in the Coulomb electrostatic energy. Since the n-p effective interaction energies (0.5-2 MeV) are much smaller than the mean nuclear potential energy (≈ 50 MeV), we use the approximation that proton and neutron radial wave functions $u_p(r, J)$ and $u_n(r, J)$ can be calculated by neglecting the n-p interaction, and by solving the Schrödinger equation in Woods-Saxon nuclear potentials whose depths have been adjusted to reproduce the observed neutron or proton binding energies for the states in ^{16}N and ^{16}F . Results as shown Fig. 6.22. Wave functions are quasi-identical between ^{16}F (full lines) and ^{16}N (dashed lines) except for the $2s_{1/2}$ wave functions. Using a schematic zero-range $v_J^{pn} = a_J \delta(r_p - r_n)$ interaction, the n-p interaction $\text{Int}^{\text{over}}(J)$ is [164]:

$$\text{Int}^{\text{over}}(J) = \frac{a_J}{4\pi} \int_0^\infty \frac{1}{r^2} [u_p(r, J)u_n(r, J)]^2 dr \quad (6.28)$$

where a_J contains the strength of the n-p nuclear interaction. As the zero-range delta function is only a crude approximation of the nuclear force, the a_J coefficients have been adjusted to equate the calculated and experimental ($\text{Int}_{^{16}\text{N}}^{\text{exp}}(J)$) interaction energies in ^{16}N . By virtue of the charge symmetry of nuclear forces, the *same* a_J coefficients should be used to calculate the interaction energies $\text{Int}_{^{16}\text{F}}^{\text{over}}(J)$ in ^{16}F . Comparison between experimental and calculated interaction energies given in Table 6.5 deserve several

important remarks. Firstly, the $\text{Int}_{^{16}\text{F}}^{\text{over}}(2,3)$ values are similar to those in the mirror system $\text{Int}_{^{16}\text{N}}^{\text{exp}}(2,3)$. This can be explained by the fact that the unbound proton and bound neutron $1d_{5/2}$ wave functions are similar in the mirror systems (see Fig. 6.22). This is due to the high $\ell=2$ centrifugal barrier of ≈ 3 MeV and Coulomb barrier of ≈ 3 MeV that prevent the unbound proton in ^{16}F to couple strongly with the continuum. This is also confirmed with the very narrow measured widths of 5 keV and 15 keV of the 2^- and 3^- states. Secondly, the calculated $\text{Int}_{^{16}\text{F}}^{\text{over}}(0,1)$ values, built on the $2s_{1/2} \otimes 1p_{1/2}$ coupling, are intermediate between the experimental values of ^{16}N and ^{16}F . As $\ell=0$ protons (from $2s_{1/2}$) in ^{16}F do not encounter any centrifugal barrier, their radial wave function is more extended, as shown in Fig. 6.22. Consequently the overlap between the wave functions of the $2s_{1/2}$ unbound proton and the deeply bound $1p_{1/2}$ neutron is reduced. Thirdly, as the $\text{Int}_{^{16}\text{F}}^{\text{over}}(J)$ values differ from the experimental $\text{Int}_{^{16}\text{F}}^{\text{exp}}(J)$ values, an additional effect is required to understand the differences.

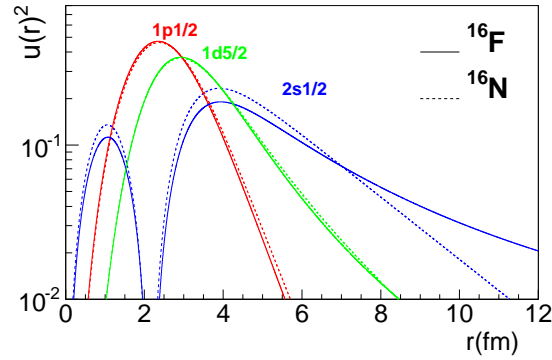


Figure 6.22: Calculated $1p_{1/2}$, $1d_{5/2}$ and $2s_{1/2}$ single particle radial wave functions $u_n(r)$ and $u_p(r)$ (see text) for ^{16}N (dashed lines) and ^{16}F (full lines). For the scattering states, the unbound proton wave function in the region between $r=0$ and $r=16$ fm is renormalized to 1 in order to have the proton inside the nucleus before it decays. The $2s_{1/2}$ wave function of the unbound proton in ^{16}F is more spatially spread than it is for the bound neutron in ^{16}N , contrary to the $1d_{5/2}$ unbound proton wave function that is retained inside the nucleus by the centrifugal barrier.

While the change in Coulomb energy between two isotopes can be usually neglected for bound states, the apparent radial extension of the wave function of an unbound state can be larger than that of a bound state, leading to a change in Coulomb electrostatic energy $E_c(J)$. In the case of ^{16}F , the interaction energy should therefore be rewritten for each state J . As for the $J=0,1$ states it writes:

$$\text{Int}_{^{16}\text{F}}^{\text{over}+\text{C}}(J) = \text{Int}_{^{16}\text{F}}^{\text{over}}(J) + E_c(^{16}\text{F}(J)) - E_c(^{15}\text{F})_{1/2+}$$

Coulomb energies are determined by using the following relation between the charge distribution $\rho(r)$ of the core ^{14}O nucleus with $Z_{\text{core}}=8$ and a single proton in the $2s_{1/2}$ or $1d_{5/2}$ orbit having radial wave functions $u_p(r,J)$:

$$E_c(J) = \frac{Z_{\text{core}}}{4\pi\epsilon_0} \int_0^\infty \frac{\rho(r)u_p(r,J)^2}{r} dr \quad (6.29)$$

To give an example, it is found that $E_c(^{16}\text{F}(0^-)) - E_c(^{15}\text{F})_{1/2+} = 168$ keV. By applying this Coulomb energy correction as well as the one due to the change in wave functions overlaps between mirror nuclei,

it is found that the calculated $\text{Int}_{16\text{F}}^{\text{over}+C}(J)$ and experimental $\text{Int}_{16\text{F}}^{\text{exp}}(J)$ interaction energies are very similar, as shown in Table 6.5. This suggests that differences in the proton-neutron interaction energies between the two mirror nuclei are very well accounted for by these two combined effects, the amplitude of which sensitively depends on the energy *and* angular momentum of the states under study.

Our results agree very well with those obtained by Ogawa et al. [150] where the mirror system ^{16}F - ^{16}N was studied using different model which is based on one particle plus one hole on top of the ^{16}O inert core, the residual interaction being calculated with the M3Y interaction and single-particle wave functions obtained under the Woods-Saxon plus Coulomb potential. Compared to this work, our model is even simpler and explains perfectly the observed differences between the two mirror nuclei. This good agreement and the simplicity of our model makes this system a particularly interesting textbook case for understanding the effect coupling to continuum on effective nuclear forces and subsequent shell reordering.

6.5.5 Conclusion and Outlook

In summary, properties of the low lying states of ^{16}F were measured with unprecedented energy accuracy and resolution by means of the proton elastic scattering reaction $^{15}\text{O}(p,p)^{15}\text{O}$ in inverse kinematics. The measured properties were used in an astrophysical context. For the first time, we proposed to study the sequential $(p, \gamma)(\beta^+)$ reaction, proceeding through an intermediate proton-unbound nucleus. The calculated $^{15}\text{O}(p, \gamma)(\beta^+)^{16}\text{O}$ cross section is found to be almost 10^{10} times larger than the direct $^{15}\text{O}(p, \beta^+)^{16}\text{O}$ reaction cross section. Within uncertainties, the $^{15}\text{O}(p, \gamma)(\beta^+)^{16}\text{O}$ reaction rate is as intense as the rate of the important reaction $^{15}\text{O}(\alpha, \gamma)^{19}\text{Ne}$. It would be of great interest to demonstrate experimentally the existence of $(p, \gamma)(\beta^+)$ reactions. The cross section of the $^{15}\text{O}(p, \gamma)(\beta^+)^{16}\text{O}$ reaction is calculated to be in the nanobarns range and can be measured using next generation intense RIB. The measured ^{16}F properties were also used to deduce that the effective proton-neutron interactions between the mirror nuclei differ by as much as 40% for the $J^\pi=0^-, 1^-$ states and by only 10% for the $J^\pi=2^-, 3^-$ states, although the latter states lie at higher energy in the continuum. We demonstrated that these features are well explained by the effect of the presence of the proton wave functions in the continuum that reduces proton and neutron radial overlaps and induces significant changes in Coulomb energy. A correct treatment of continuum is required for predicting the location of drip-lines, modeling weakly bound nuclei such as halo nuclei and predicting resonant states of astrophysical importance for X-ray bursters and for the r-process nucleosynthesis.

For the outlook, several ideas can be proposed:

- **Is the formalism used here correct?** The strength function of the ^{16}F g.s. resonance was calculated assuming a Breit-Wigner parametrization:

$$P_\gamma(E_\gamma) \propto \frac{1}{(\Delta E)^2 + \left(\frac{\Gamma_{\text{Tot}}^{\text{g.s.}}(E_p - E_\gamma)}{2}\right)^2}. \quad (6.30)$$

It might be incorrect. We discussed this question with several theoreticians. The same question was discussed in the context of the two-proton radioactivity (Ref [165] section 2 simultaneous versus sequential decay) in the calculation of the distance which the "first" emitted proton can

travel while the "second" is "confined" in the tail of the resonance. In the book of A.I. Baz', Ya.B. Zel'dovich and A.M. Perelomov [166], in the case the particle is scattered by a nuclear potential, it is shown that mean lifetime the particle spent inside the nuclear sphere is

$$T(E) = \frac{\hbar\Gamma_{Tot}}{(\Delta E)^2 + (\frac{\Gamma_{Tot}}{2})^2}. \quad (6.31)$$

Then, the branching for β -decay is

$$BR = \frac{\Gamma_{\beta}}{\Gamma_{Tot}} = \frac{T(E)}{T_{\beta}} = \frac{\hbar\Gamma_{Tot}^2}{(\Delta E)^2 + (\frac{\Gamma_{Tot}}{2})^2} \times \frac{\Gamma_{\beta}}{\Gamma_{Tot}} = P_{\gamma}(E_{\gamma}) \times \frac{\Gamma_{\beta}}{\Gamma_{Tot}} \quad (6.32)$$

and so

$$P_{\gamma}(E_{\gamma}) \propto \frac{\Gamma_{Tot}^2}{(\Delta E)^2 + (\frac{\Gamma_{Tot}}{2})^2} \quad (6.33)$$

The term $\Gamma_{Tot}^{g.s.}(E_p - E_{\gamma})^2$ might be missing in the numerator of Equ. 6.30.

Our criticize about this interpretation is the following. Here we are not dealing with a particle outside the nucleus which scatters on a nuclear potential. Here the particle is already inside the nucleus. The probability to find it inside the nucleus at $t=0$ is equal to 1. Equ. 6.31 doesn't apply here. we don't have a definitive conclusion. It would be interesting that theorists work this question.

- **Is this idea of long-lived unbound nucleus incompatible with quantum mechanics rules?** Not at all! It is true that broad resonances mean short-lived states. But, the case presented here, a quasi-bound ¹⁶F ground state when populated in the low energy tail of the resonance, could be a striking example of the predicted and already observed non-exponential decay [167]. This is another theoretical aspect of the study that should be investigated further.

This work was the subject of the Iulian Stefan Ph.D. thesis [168] and was published in Ref. [169].

6.6 ¹⁵F: Reefs in the Sea of Instability (E521S)

6.6.1 Astrophysical motivation

The astrophysical reaction ¹⁵O(p,γ)(β^+)¹⁶O proposed in the Section 6.5 proceed through a γ -transition between two unbound states, an excited state and the ground state of an unbound nucleus. As it was discussed in the Conclusion, there are several theoretical aspects that are still unclear (at least from our point of view). Is it possible to observe internal γ -transitions to the ground state of an unbound nucleus? (a kind of internal bremsstrahlung). What is the strength function of the unbound g.s. resonance seen from an internal γ -transition? Is it possible to transform a short-lived unbound nucleus into a quasi-bound nucleus? (when populated in the very low energy tail of the ground state). It would be very interesting to get the answers to these questions theoretically, or experimentally. Electromagnetic transitions between resonances have been rarely observed, e.g. in the unbound nucleus ⁸Be [170, 171], and never been observed to a ground-state resonance.

We proposed to study the unbound nucleus ¹⁵F. It could be the perfect test case since a narrow excited state was predicted in this nucleus. The ground and the first excited states are known, they are broad

Table 6.6: Resonance energy, width and spin measured and theoretical predictions for the second excited state of ^{15}F .

| | Ref. | Second excited state | | |
|-----------|---------|----------------------|----------------------|-----------------|
| | | $E_R(\text{MeV})$ | $\Gamma(\text{keV})$ | J^π |
| Measured | [178] | 4.800(100) | 150(100) | - |
| | [179] | 4.900(200) | 200(200) | - |
| | Present | 4.757(16) | 36(19) | $\frac{1}{2}^-$ |
| Predicted | [175] | 5.49 | 5 | $\frac{1}{2}^-$ |
| | [176] | 4.63 | 55 | $\frac{1}{2}^-$ |
| | [172] | 4.63 | 38 | $\frac{1}{2}^-$ |

resonances. Candidate for the second excited state can be looked at in the mirror nucleus. The second excited state in the mirror nucleus ^{15}C is known at the energy of 3103 keV, with $J^\pi = 1/2_1^-$ and a width $\Gamma = 29(3)$ keV [172]. This state was populated strongly in two-neutron transfer reactions with a ^{13}C target [173, 174], indicating a structure of mainly two sd-shell neutrons coupled to a ^{13}C core. Canton *et al.* [175] used the multichannel algebraic scattering theory with Pauli-hindered method in order to predict the properties of the low-lying states in ^{15}F . A very narrow width $\Gamma=5$ keV was predicted for the second excited state, see Table 6.6. Fortune and Sherr [176] used a potential model to determine the single-particle widths which they scaled down to reproduce the measured widths in ^{15}C . The extracted θ^2 were used to calculate widths in the mirror nucleus ^{15}F . These calculations confirmed that narrow resonances are to be expected in $^{14}\text{O}+p$, but they obtained a width 10 times larger than the one of Ref. [175] for the second excited state. Refined values were later published by Fortune [172], see Table 6.6. Canton *et al.* [177] objected that θ^2 do not necessary scale with the single-particle widths, especially when the θ^2 is small [55]. A first indication for the observation of the second excited state in ^{15}F was obtained at GANIL by Lepine-Szily *et al.* [178] through the measurement of the transfer reaction $^{16}\text{O}(^{14}\text{N}, ^{15}\text{C}(0.740 \text{ MeV})^*)^{15}\text{F}$. A narrow peak of ≈ 10 counts with a width of only 150(100) keV was observed. This state was also observed through the angular correlations of decay products in the fragmentation of ^{17}Ne [179], with slightly more statistics (≈ 20 counts) but a worse resolution. Results of these measurements are summarized in Table 6.6. The narrow width is particularly surprising since this state is located 3.5 MeV above the Coulomb plus centrifugal barrier of the system $^{14}\text{O}+p$. The spin of this second excited state has not been assigned.

6.6.2 Experiment

The ^{15}F nucleus was studied using the resonant elastic scattering technique, the same technique as used with the other unbound nuclei (Sections 6.3, 6.4 and 6.5). The excitation function of the elastic scattering reaction $^{14}\text{O}(p,p)^{14}\text{O}$ was obtained in inverse kinematics using a thick target. The experiment was performed at the GANIL SPIRAL1 facility. Two beams were used: the radioactive beam of ^{14}O for the study of ^{15}F , and a stable beam ^{14}N for calibrations. Radioactive $^{14}\text{O}^{3+}$ ions were produced through the fragmentation of a 95 MeV/u ^{20}Ne primary beam impinging on a thick carbon production target. The ions were post-accelerated with the CIME cyclotron up to the energy of 5.95(1) MeV/u with an energy

spread $<0.2\%$. The isobaric contamination of the beam was reduced down to $0.0(1)\%$ using a $0.9\ \mu\text{m}$ thick stripper aluminium foil located at the entrance of the LISE zero degree achromatic spectrometer. The $^{14}\text{O}^{8+}$ ions were selected using LISE and transported to the experimental setup located in the D4 experimental area. An average beam intensity of $1.88(1)\times 10^5$ pps was achieved. This value was obtained by regularly measuring the beam intensity with a silicon detector in conjunction with a calibrated beam intensity reduction system, as well as by counting the $2.312\ \text{MeV}$ γ -ray emitted in the β -decay of ^{14}O using a high-purity germanium detector. The beam was sent to a thick target where it was stopped. The target was made of three (four in the case of ^{14}N) polypropylene $(\text{CH}_2)_n$ foils, $50\ \mu\text{m}$ thick each. The foils were fixed side by side with the last one put on the $250\ \text{rpm}$ rotating system FULIS [136]. This system was used to reduce the background arising from the β -delayed proton emission of ^{14}O ($t_{1/2}=70.6\ \text{s}$). Counting rate was reduced from $85\ \text{Hz}$ with the stopped target to $\approx 1\ \text{Hz}$ with the rotating target. The scattered protons were detected downstream in a $\Delta E(500\ \mu\text{m})$ - $E(6\ \text{mm cooled SiLi})$ telescope of silicon detectors that covered an angular acceptance of $\pm 2.2(2)^\circ$. Identification of the protons was made using contours on ΔE - E and time-of-flight parameters. An experimental energy resolution, $\sigma_{c.m.} = 7(2)\ \text{keV}$, was measured from the width of the observed peaks. The major contributions to this resolution were from the ΔE - E detectors ($4.2\ \text{keV}$ and $3.0\ \text{keV}$) and the beam and proton straggling in the target ($4.7\ \text{keV}$).

6.6.3 Results

The measured excitation function of the $^{14}\text{O}(p,p)^{14}\text{O}$ reaction, performed at 180° (c.m.), is shown in Fig. 6.23. An analysis of the excitation function using the R-Matrix method was performed with the code AZURE2 [92]. A deep minimum is observed at $\approx 1\ \text{MeV}$ corresponding to the well known $J^\pi = 1/2_1^+$ ground state resonance of ^{15}F . It is fitted at an energy $E_R = 1270(10)(10)\ \text{keV}$ with $\Gamma = 376(70)(0^{+200})\ \text{keV}$, where the quoted uncertainties correspond to statistical and systematic uncertainties respectively. The peak observed at the resonance energy $E_R = 2763(9)(10)\ \text{keV}$ with $\Gamma = 305(9)(10)\ \text{keV}$ corresponds to the $J^\pi = 5/2_1^+$ first excited state. In addition, for the first time in a resonant elastic scattering experiment, the second excited state is clearly observed (insert of Fig. 6.23) as a narrow dip at a resonance energy of $\approx 4.8\ \text{MeV}$. In the corresponding mirror nucleus, the second excited state has spin $J^\pi = 1/2_1^-$. The resonance has the shape predicted by Canton *et al.* [175], which is due to destructive interferences between the $J^\pi = 1/2_1^-$ resonance and Coulomb scattering. No other spin assignment can better reproduce the shape of the structure. It is the first time the spin of this state is assigned. A GSM calculation in the coupled channel representation (GSM-CC) was performed and reproduced very well the data, see Fig. 6.23. A R-Matrix fit of the excitation function was performed taking into account the experimental resolution. The resonance is measured to be $E_R = 4.757(6)(10)\ \text{MeV}$ with $\Gamma = 36(5)(14)\ \text{keV}$. The measured properties are in good agreement with the previous experimental results, see Table 6.6. The present work shows a significant improvement in the resolution, at least by a factor 5.

The observation of this narrow resonance in ^{15}F is surprising since this resonance is located well above the Coulomb plus centrifugal barrier ($B_C + B_\ell \approx 3.3\ \text{MeV}$) for the proton emission, there is no barrier to retain the proton inside the nucleus. The single-particle width of this state is 1.6 - $3.0\ \text{MeV}$ [176] (depending on the model parameters), compared to the measured value of $36(19)\ \text{keV}$. This implies that the measured lifetime is more than 40 times longer. As discussed before, the second excited state is known in the mirror nucleus ^{15}C at an energy of $3103\ \text{keV}$. It is unbound with respect to one neutron emission, and has a width of $29(3)\ \text{keV}$ [172]. Here too, the resonance is located above the $\ell = 1$ centrifugal barrier

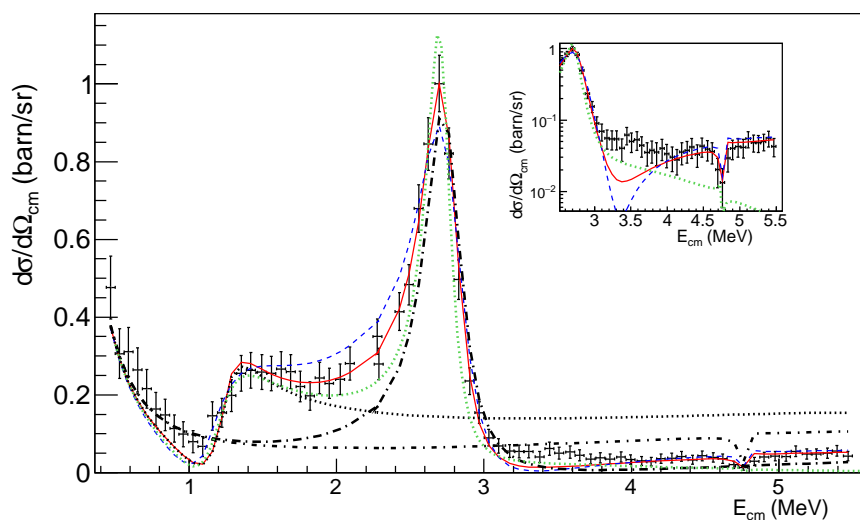


Figure 6.23: The excitation function of the reaction $^{14}\text{O}(p,p)^{14}\text{O}$ measured at 180° in the center of mass system. *R*-Matrix calculations corresponding to the ground state alone (dotted line), first excited state (thick-dot-dash line), second excited state (thin-dot-dash line) are shown. Inset: A structure clearly visible at an energy close to 4.8 MeV is assigned to the $1/2_1^-$ second excited state of ^{15}F (see text for details). Data are compared to the best *R*-Matrix fit (red line) using the properties given in Table 6.6. The *R*-Matrix calculation made with $\Gamma = 737$ keV for the ground state is also shown (blue dashed line) for comparison. Here, the error bars correspond to the statistical uncertainties. The calculation using the GCM-CC approach is also shown (green dotted line).

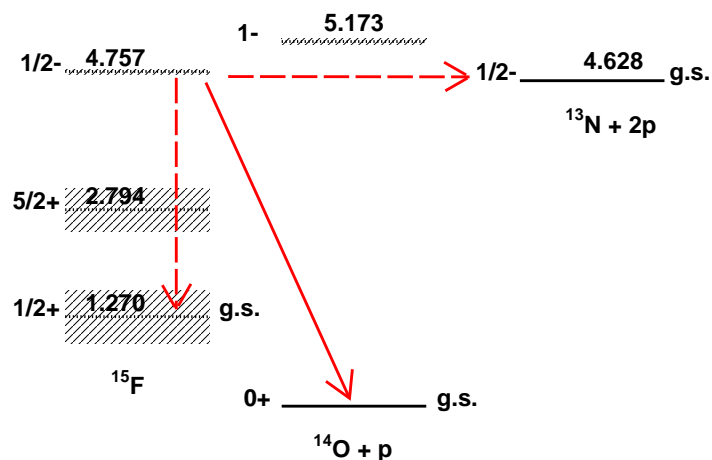


Figure 6.24: Level scheme of ^{15}F . The possible decay channels from the $J^\pi=1/2_1^-$ resonance are: the one proton emission (red arrow), gamma transition and two proton emission (red dashed arrow). The hatched areas correspond to the width of the resonances.

($B_\ell \approx 1.2$ MeV), nevertheless it is still very narrow. There are experimental evidences in the mirror nucleus that this negative-parity state is a nearly pure $(sd)^2$ configuration coupled to the ground state of ^{13}N [173, 174]. This is confirmed for ^{15}F with the GSM calculations. The emission of two protons from the narrow state is energetically possible, as seen in Fig. 6.24. Since there is no intermediate state accessible to ^{14}O , it should be a direct two-proton emission to the g.s. of ^{13}N . However, the available energy is only $Q_{2p} = 129$ keV, inducing a Wigner limit of $\Gamma_{2He} = 4 \times 10^{-11}$ eV ($t_{1/2} = 16.5 \mu\text{s}$) for the emission of a ^2He cluster with $\ell=0$. Moreover, it is known that the modeling of the decay by the tunneling of a ^2He cluster overestimates the two-proton width [180, 181]. Therefore, the branching ratio for the emission of two protons is expected to be extremely small. In another words, we confirm that this state is a good candidate for the observation of γ -transition to the ground state.

This work was the subject of the Ph.D. thesis of Florence de Grancey [182]. Much more details can be found in the Ref. [183].

6.6.4 Conclusion and Outlook

To summarize, our experiment confirmed the existence of a narrow resonance in ^{15}F , the second excited state. The extended lifetime is explained by the fact that the dominant structure of this state involves two-nucleon excitations, whereas the decay is through a single-nucleon emission.

For the outlook, two comments can be proposed:

- Now, this $1/2^-$ state can be used to test our idea of internal γ -transition and its possible astrophysical interest. This state being a "long-lived" resonance, a γ -transition from this resonance to the g.s. resonance is conceivable. $E1$ transitions occurring between $1s_{1/2} \rightarrow 0p_{1/2}$ single-particle states are expected to be extremely fast. In ^{11}Be , the $1/2_1^- \rightarrow 1/2_1^+$ γ -transition is the fastest

known dipole transition between bound states. This remarkable property is due to the neutron halo structure of ^{11}Be [184]. The γ -width is larger since the electric transition is proportional to the radial integral $\int u_f(r) r u_i(r) dr$ where $u_{f,i}(r)$ are final and initial radial wave functions of the nucleon, the ground state of ^{11}Be having a very extended radial wave function. This is also the case of ^{15}F , see Fig. 6.25. Taking this property into account and the neutron/proton effective charge difference,

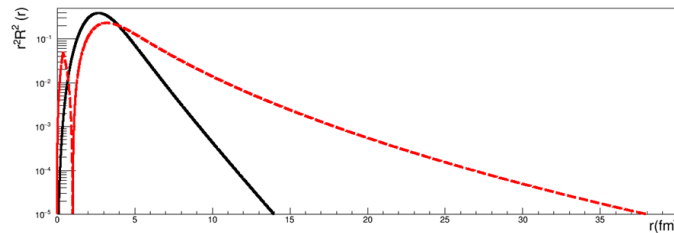


Figure 6.25: Single-particle wave functions of the $1s_{1/2}$ (red line) and the $0p_{1/2}$ (black line) shells in ^{15}F .

we predicted $\Gamma_\gamma \approx 50$ eV. If true, it would be much faster than in ^{11}Be . The cross section for the reaction $^{14}\text{O}(p, \gamma)^{15}\text{F}_{gs}$ is predicted to be ≈ 0.5 mb. Using a 10^5 pps beam of ^{14}O as available at GANIL, the expected count rate is ≈ 13 γ /hour, that can be measured using high efficiency γ -detectors. These γ -rays will be in coincidence with protons emitted from the ground state of ^{15}F , which will make the experiment easier by improving the peak to the noise signal. A proposal was submitted in 2016 to the GANIL PAC (E744: I. Stefan, F. de Oliveira) and was accepted. This next experiment has the objective to observe γ -transition inside an unbound nucleus.

- As discussed in the Introduction of this Chapter, there is a very interesting conjecture made by Ikeda *et al* [107]: The coupling to a nearby particle/cluster decay channel induces particle/cluster correlations in nuclear wave functions. It is claimed in Ref [108] that this conjecture holds for all kinds of cluster states including unstable systems like dineutron, or ^8Be . This mechanism, for example, could explain the origin of the Hoyle state in ^{12}C , one of the most important states in astrophysics. Here, the case of the second excited state in the unbound nucleus ^{15}F could be one example of such an increase of correlation. The state is located very close to the two-proton emission threshold, and it is described as a nearly pure $(sd)^2$ configuration. It would be interesting to measure if this state has an increased $2p$ spectroscopic factor compared to the $2n$ spectroscopic factor in the mirror nucleus. A $2p$ versus $2n$ transfer reaction could be a very interesting way to measure it.

6.7 Final Conclusion

In each section of this Chapter, there is a paragraph giving the conclusion and outlook of the section. To conclude this Chapter, it is good to say that many interesting and surprising results were obtained in the studies of the unbound nuclei. It turned out to be a very rich subject of study. Results were obtained about the nuclear force beyond the drip line, the nuclear structure far from stability, and more surprisingly, they challenged our understanding of quantum mechanics. Possible impact in astrophysics was also discussed.

Conclusion

This document is a review of different studies, mostly experimental studies, performed in order to improve our understanding of several astrophysical problems. To conclude this document, let's summarize the main results obtained within our collaboration and presented in this document, and make a list of interesting ideas for the outlook.

Main results

- The effect of the electron screening, measured on the nuclear cross sections at low energies, is not yet understood. The measured effect ($U_e \approx 200$ eV) is much larger than the adiabatic limit ($U_e \approx 100$ eV). We performed two very precise experiments to measure the effect of the electron screening on the half-life of radioactive nuclei implanted into different materials (metal, superconductor and insulator). No change was observed within the precision of $\approx 10^{-4}$. This is in agreement with the expected "low" effect of the screening ($U_e \approx 100$ eV).
- The origin of fluorine in the Universe is not yet well known. The reaction $^{15}\text{N}(\alpha, \gamma)^{19}\text{F}$ was identified as an important reaction for the production of fluorine in AGB and WR stars. The rate of this reaction was determined indirectly through the measurement of the transfer reaction $^{15}\text{N}(^7\text{Li}, t)^{19}\text{F}$. The new rate being lower than the former, this study has exacerbated the problem of the origin of fluorine in the Universe.
- Novae explosions are predicted to be the source of γ -rays, the isotope ^{18}F being the main source the first hours after the explosion. We performed two experiments in order to measure the properties of the ^{19}Ne excited states which can contribute to the $^{18}\text{F}(p, \alpha)^{15}\text{O}$ reaction cross section. The inelastic scattering reaction $^1\text{H}(^{19}\text{Ne}, p)^{19}\text{Ne}^*(p)^{18}\text{F}$ was measured in inverse kinematics, and both the $^{18}\text{F}(p, \alpha)^{15}\text{O}$ and the $^{18}\text{F}(p, p)^{18}\text{F}$ reactions. The main objectives of these experiments were to determine the spins of the excited states and to confirm the existence of a new broad $\frac{1}{2}^+$ resonance. These experiments were successful. It was found that the low energy tail of the $\frac{1}{2}^+$ resonance contributes to a significant enhancement of the ^{18}F destruction rate at nova temperature. This reduces significantly the chance to observe γ -ray emission of ^{18}F from a nearby nova explosion with existing space telescopes.
- The strength of the $^{15}\text{O}(\alpha, \gamma)^{19}\text{Ne}$ reaction not only controls the ignition point of the X-ray bursts but also affects the burst recurrence rate. An educated guess about the ^{19}Ne properties allowed predicting the rate of this reaction, but the prediction was still quite arbitrary. We used the measured properties of the mirror nucleus ^{19}F to deduce those of ^{19}Ne and calculate the rate of the reaction.
- We proposed a simple formalism to calculate the $pp1$ reaction. The calculated reaction rate is in agreement with the reference one within 10%. This simple formalism can be used to estimate other reactions involving the weak interaction.

- We measured the properties of 4 unbound nuclei: ^{19}Na , ^{18}Na , ^{16}F , ^{15}F with unprecedented energy precision using the resonant elastic scattering method. We calculated the two-proton capture reactions $^{18}\text{Ne}(2p,\gamma)^{20}\text{Mg}$ and $^{18}\text{Ne}(2p,\gamma)^{20}\text{Mg}$ using the formalism of sequential, quasi-simultaneous two-proton capture, and evaluated its astrophysical impact. It was found that, very probably, these reactions are interesting only at extreme densities well above the X-ray bursts conditions. We also evaluated the impact of ^{18}Na on the two proton radioactivity of ^{19}Mg . It was found that the calculated value is not in agreement with the experimental value. This difference might be due to a slightly incorrect shell model prediction of the ^{19}Mg ground state properties. If the observed difference (factor 10) is applied to the inverse reaction (two-proton capture), this study shows that the calculations of the astrophysical two-proton capture reaction should be reliable within a factor 10. For the first time, we proposed to study the sequential $(p,\gamma)(\beta^+)$ reaction (with the formalism used for the $pp1$ reaction), proceeding through an intermediate proton-unbound nucleus. We have also observed a relatively long-lived excited state in ^{15}F . Its extended lifetime is explained by the fact that the dominant structure of this state involves two-nucleon excitations, whereas the decay is through a single-nucleon emission. The measured ^{16}F properties were also used to deduce that the effective proton-neutron interactions between the mirror nuclei $^{16}\text{F} / ^{16}\text{N}$ differ by as much as 40% for the $J^\pi=0^-, 1^-$ states and by only 10% for the $J^\pi=2^-, 3^-$ states, although the latter states lie at higher energy in the continuum. We demonstrated that these features are well explained by the effect of the presence of the proton wave functions in the continuum that reduces proton and neutron radial overlaps and induces significant changes in Coulomb energy.

Outlook

- The large effect of the electron screening measured on the nuclear cross sections at low energies is probably of atomic origin, and the project FISIC will bring new pieces of information on this subject. Recently a new idea was proposed, where the cluster-like structure of the nuclei plays an important role. It would be very interesting to test this idea by measuring the predicted shift of resonance energy due to the electron screening. The energy shift would be "normal" if the cluster-like structure explanation is correct, or "high" if it is an atomic explanation. This is a very difficult experiment since the energy shift is predicted to be only $\approx U_e \approx 100$ eV. In principle, this is possible to measure using the resonant elastic scattering method in inverse kinematics (a factor 4 between center-of-mass and lab in the energy resolution) and a high resolution spectrometer.
- Our study about the origin of fluorine suggests that the rate of the reaction $^{15}\text{N}(\alpha,\gamma)^{19}\text{F}$ is well known, but this is not the case. We know that the rate of this reaction is low, but it is not known precisely. Despite the very weak cross section, direct measurement of the $^{15}\text{N}(\alpha,\gamma)^{19}\text{F}$ reaction at low energy will be reachable at the upgraded LUNA-MV underground laboratory [185] or at the European Recoil Separator for Nuclear Astrophysics (ERNA) installed at the CIRCE laboratory of Caserta in Italy.
- The success of our studies suggest that the ^{19}Ne -spins problem is solved, but the rate of the $^{18}\text{F}(p,\alpha)^{15}\text{O}$ reaction is not yet well known. A third experiment (E641S) about the ^{19}Ne spectroscopy was performed at GANIL with the VAMOS spectrometer. The main motivation of this experiment was the search for the predicted second $\frac{1}{2}^+$ state, expected to be below the proton threshold, and which could have a high contribution. A first indication of the presence of this $\frac{1}{2}^+$

state was obtained. Results obtained in this experiment are about to be submitted. The ANC coefficient of this state was not measured, and it will be the next parameter to measure. Depending on it, the rate could change by more than a factor 10. The measurement of the ANC is possible only with a transfer reaction, like ${}^3\text{He}({}^{18}\text{F},d){}^{15}\text{O}$, or with the direct measurement of the cross section at low energy. The reaction ${}^{15}\text{O}(\alpha,\alpha){}^{15}\text{O}$ could be used, as first tried in the E442S experiment, to obtain an extremely high resolution and to search for not-yet-observed states. An unexpected noise was observed in the E442S experiment. It is one of our priorities to identify the origin of this problem and remove it. In principle, once solved, we could submit the same proposal to the GANIL PAC committee. Another interesting idea is to use an active target, like ACTAR TPC. The noise could be strongly reduced by selecting each event with an interaction point within the gas target.

- We performed another experiment, E710, to study the γ -ray emitter ${}^{22}\text{Na}$. We measured the lifetime of the 7.786 MeV state in ${}^{23}\text{Mg}$ with the Doppler Shift Attenuation Method and the AGATA gamma spectrometer, and tried to measure its branching ratio for the proton emission. This experiment is under analysis.
- We proposed a new technique, the inelastic scattering, to perform efficiently the spectroscopy of nuclei and to determine the spin of the states in a model-independent way. The technique was proposed recently at GANIL to study the astrophysical reaction ${}^{30}\text{S}(\alpha,p){}^{33}\text{Cl}$, important for the X-ray bursters, through the measurement of the inelastic scattering reaction ${}^{34}\text{Ar}(p,p){}^{34}\text{Ar}^*$. This experimental technique could also be used in several other problems in astrophysics and in nuclear structure.
- A new generation of γ -ray space telescope is urgently needed if we want to observe γ -rays in the MeV range from novae outbursts.
- The cross section of the ${}^{15}\text{O}(\alpha,\gamma){}^{19}\text{Ne}$ reaction is known probably within a factor 2 to 10, and will be extremely difficult to measure directly at low energy. An indirect measurement of the reaction, through for example the transfer reaction ${}^6\text{Li}({}^{15}\text{O},d){}^{19}\text{Ne}$, could be proposed at GANIL with the VAMOS spectrometer. In fact, this idea was already proposed in 2010 (Lol of C. A. Diget,... F. de Oliveira *et al*) within the project SPIRAL2 phase2.
- The reaction ${}^{14}\text{O}(\alpha,p){}^{17}\text{F}$ is relevant to the X-ray bursters, and it is badly known. In principle, the direct measurement of this reaction is possible at quite low energy. We could use an active target to degrade the beam energy and, in the same time, to increase the peak to noise signal. Another idea is to modify the CIME cyclotron of SPIRAL in order to accelerate the beam to lower energies (lower than 3.5 MeV/u) and to better purify the beam in the same time.
- It would be of great interest to demonstrate experimentally the existence of $(p,\gamma)(\beta^+)$ reactions. The cross section of the ${}^{15}\text{O}(p,\gamma)(\beta^+){}^{16}\text{O}$ reaction is calculated to be in the nanobarns range and could be measured using next generation intense RIB. It would be interesting that theoreticians work the question of the resonance strength function when fed from inside a nucleus by γ -transition. One step in this direction will be to observe a γ -transition to the ground state in an unbound nucleus. A proposal was accepted recently with the objective to measure this kind of transition from the newly discovered $\frac{1}{2}^-$ state of ${}^{15}\text{F}$.

- It would be interesting to test the conjecture made by Ikeda *et al* [107]: The coupling to a nearby particle/cluster decay channel induces particle/cluster correlations in nuclear wave functions. It would be interesting to measure if the $\frac{1}{2}^-$ narrow state in ^{15}F has an increased $2p$ spectroscopic factor compared to the $2n$ spectroscopic factor in the mirror nucleus. A $2p$ versus $2n$ transfer reaction could be a very interesting way to study it.
- Not presented in this document, the origin of the "*p nuclei*" is also one subject of our scientific program. We started a series of test experiments in order to measure directly the reaction $^{78}\text{Kr}(\alpha, \gamma)^{82}\text{Sr}$ at low energy using the Wien Filter of the LISE spectrometer. The final objective is to measure a finite list of reactions that we be used to constrain the α optical model potentials in the theoretical models (Lol for SPIRAL2 - S. Harrissopulos *et al*, Greece).
- Not presented in this document, β -decay can also be used to study some interesting states in astrophysics. The most interesting cases are the β -delayed proton emission when the protons are emitted from states of astrophysical interest. We studied the case of ^{22}Al in details (see Ref. L. Achouri *et al* [186, 187]). There is still a quite long list of interesting cases to study with the method. Recently, we proposed an experiment (A.M. Sánchez Benítez - L16-18 (E747)) using an active target (TPC Detector) in order to measure the very low energy protons of astrophysical interest (without the energy deposit of the β -particles).
- Radioactive beams developments are also very important. I was the coordinator of the working group for the production of "Radionuclides from Other Beams Other Targets" (ROBOT) within the SPIRAL2 Phase 2 project, which also fits the EURISOL plans. We produced documents and proposed a strategy to get the most important beams for astrophysics. We performed an experiment to measure the production cross section of ^{14}O , see Ref. [188]. Based on this new result, the potential in-target ^{14}O yield at SPIRAL2 was estimated: 2.4×10^{11} pps, for 1mA of ^3He at 35MeV. This is a factor 140 higher than the in-target yield at SPIRAL1. A prototype of production-unit was proposed. The next step will be to test the target, mainly the thermal issues.
- A facility dedicated to the astrophysical reactions with radioactive nuclei, like the LUNA underground facility which involves only stable ions beams, does not exist yet. On the other hand, new generation of RIB facilities are now being conceived and constructed, including SPIRAL2, NSCL ReA3 [189]. In the SPIRAL2 facility, the new production unit ROBOT could provide great opportunity to conduct the direct measurements of important astrophysical reactions whose cross sections are not determined well or not available yet at low energies.
- Another idea is to increase the energy range of the radioactive beams (RIB) at GANIL. Today, the RIB energy is limited from 1.75 MeV/n to 10 MeV/n for the medium mass nuclei or 25 MeV/n for $Q/M > 0.35$ beams. I was in charge of the working group 3 in the reflections on the future of GANIL (GANIL 2025). For the low energy beams, a change of the inflector of the CIME cyclotron could be the solution to obtain lower energies, down to 1 MeV/n. Lower energies ($E < 1$ MeV/n) require the building of a new accelerator. For the high energy beams, an EBIS charge breeder located before CIME could be used to increase the charge state of the beam ions up to $Q/M=0.3$, and to accelerate all of them up to 25 MeV/n. The purification of the beam is another important issue and ideas were proposed.

- Many ideas were discussed in the meeting "Future directions in physics of nuclei at low energies" at Trento (May 2014). I proposed a compilation of many ideas for the future, these are summarized in the following tables.

Acknowledgements I would like to thank all my colleagues, former students and collaborators for their continued support. I also thank GANIL, the organisations CEA, IN2P3-CNRS, the Region Calvados - Normandie, the European Union for their financial supports (Ph. D. thesis fundings, support for the experiments). I would particularly like to thank my colleagues of the different collaborations (LEA NuAG with Czech Republic, IFIN-HH Romania, Vinca Institute Serbia) and from Orsay.

| Science Case Related Questions / experimental constraints | Key reactions | Experimental Methods | Required Beams Intensities and energies | Required Facilities |
|--|--|---|---|--|
| Hydrostatic Burnings <ul style="list-style-type: none"> • Chemical evolution of the Galaxy/ origin of the elements • Number of neutron stars and black holes in the Galaxy | $^{12}\text{C}(\alpha,\gamma)^{16}\text{O}$, $^{14}\text{C}(\alpha,\gamma)^{18}\text{O}$, $^{18}\text{O}(\alpha,\gamma)^{22}\text{Ne}$, $^{22}\text{Ne}(\alpha,\gamma)^{26}\text{Mg}$ $^{12}\text{C}+\text{}^{12}\text{C}$ $^{12}\text{C}+\text{}^{16}\text{O}$ $^{16}\text{O}+\text{}^{16}\text{O}$ | Direct measurements (normal and inverse kinematics) (probably a few indirect measurements) | <ul style="list-style-type: none"> • Stable beams • Intensity ~ 500 μAe • E 0-1 A MeV • The energy must be provided by a linear accelerator, because direct measurements need accurate energies fast setting • Direct measurements needs long periods of beam time • Low gamma background | LUNA LUNA MV ERNA @ CIRCE |
| Explosive Burning Classical novae X-ray bursts <ul style="list-style-type: none"> • Chemical evolution of the Galaxy • Isotopic anomalies in Presolar grains • Understanding the luminosity profile. | $^{18}\text{F}(\text{p},\alpha)^{15}\text{O}$ $^{30}\text{P}(\text{p},\gamma)^{31}\text{S}$ $^{25}\text{Al}(\text{p},\gamma)^{26}\text{Si}$ $^{15}\text{O}(\alpha,\gamma)^{19}\text{Ne}$ $^{14}\text{O}(\alpha,\text{p})^{17}\text{F}$ $^{18}\text{Ne}(\alpha,\text{p})^{21}\text{Na}$ $^{17,18}\text{F}(\text{p},\gamma)^{18}\text{Ne}$ $^{22}\text{Na}(\text{p},\gamma)^{23}\text{Mg}$ $^{30}\text{P}(\alpha,\text{p})^{33}\text{S}$ $^{30}\text{S}(\alpha,\text{p})^{33}\text{Cl}$ $^{27}\text{Mg}(\alpha,\text{p})^{26}\text{Al}$, $^{26}\text{Si}(\alpha,\text{p})^{29}\text{P}$, $^{30}\text{S}(\alpha,\text{p})^{33}\text{Cl}$, $^{34}\text{Ar}(\alpha,\text{p})^{37}\text{K}...$ | Direct measurements (in inverse kinematics) | <ul style="list-style-type: none"> • Radioactive light neutron deficient ions beams $^{17,18}\text{F}$, ^{30}P, ^{25}Al, ^{15}O, ^{14}O, ^{18}Ne, ^{22}Na, ^{30}S ... • High purity RIB • Intensity > 10^5 pps • $0.5 < E \text{ (AMeV)} < 1.5$ • No need for very accurate beam energy • Direct measurements needs long periods of beam time (1 week to 1 month) | <ul style="list-style-type: none"> • Recoil Mass Separator Like DRAGON, ERNA, ARES, Notre Dame $^{15}\text{O}(\alpha,\gamma)^{19}\text{Ne}$, $\theta_{\text{recoil}} < \pm 16$ mrad $^{18}\text{F}(\text{p},\gamma)^{19}\text{Ne}$, $\theta_{\text{recoil}} < \pm 16$ mrad $^{25}\text{Al}(\text{p},\gamma)^{26}\text{Si}$, $\theta_{\text{recoil}} < \pm 30$ mrad |

| Science Case Related Questions / constraints | Examples of key reactions | Experimental Methods | Required Beams Intensities and energies | Required Facilities |
|--|------------------------------|--|--|---------------------|
| Explosive Burning Classical novae X-ray bursts | | Indirect measurements <ul style="list-style-type: none"> Resonant elastic scattering $^4\text{He}(^{13}\text{O},^4\text{He})^{12}\text{O}$ Transfer reactions $d(^{18}\text{F},n)^{17}\text{Ne}^*(\alpha)^{12}\text{O}$ $^3\text{He}(^{30}\text{P},d)^{27}\text{S}$ Inelastic scattering / break-up reaction $\text{H}(^{18}\text{Ne},p)^{17}\text{Ne}^*(p)^{16}\text{F}$ $\text{H}(^{31}\text{S},2p)^{29}\text{P}$ Trojan Horse Method $^7\text{Li}(^{14}\text{O},p)^{17}\text{F}d$ $^7\text{Li}(^{30}\text{P},p)^{23}\text{S}d$ $^7\text{Li}(^{28}\text{S},p)^{27}\text{Cl}d$ | Resonant elastic scattering <ul style="list-style-type: none"> Radioactive light neutron deficient ions beams Intensities $> 10^7$ pps Good purity of the beam ($> 99\%$) $E \sim 3$ A MeV 1 week of beam time All areas are ok | |
| | | | Transfer reactions <ul style="list-style-type: none"> Radioactive light neutron deficient ions beams Intensities $> 10^7$ pps High purity of the beam ($> 99\%$) $E \sim 10$ A MeV 1 week of beam time | |
| | | | Break-up reactions <ul style="list-style-type: none"> Radioactive light neutron deficient ions beams Intensities $> 10^7$ pps High purity of the beam ($> 99\%$) $E \sim 10$ A MeV 1 week of beam time | |
| | | | Trojan Horse Method <ul style="list-style-type: none"> Radioactive light neutron deficient ions beams Intensities $> 10^7$ pps High purity of the beam ($> 99\%$) $E < 2$ A MeV 1 week of beam time | |

| Science Case Related Questions / constraints | Examples of key reactions | Experimental Methods | Required Beams Intensities and energies | Required Facilities |
|--|---|---|---|--|
| Explosive Burning Supernovae • Origin of the p nuclei? | Measurement of radiative alpha capture cross sections. Ex: $^{78}\text{Kr}(\alpha,\gamma)^{82}\text{Sr}$ in order to improve the existing global semi-microscopic alpha particle optical model potentials that are used in Hauser-Feshbach calculations | Direct measurement Direct and inverse kinematics | <ul style="list-style-type: none"> Stable and Radioactive Ions Beams $A=80-140$ and $A=170-200$ mass regions Minimum beam intensity = 10^9 pps Pure beam $1 < E$ (A MeV) < 3.5 A MeV | <ul style="list-style-type: none"> A FULIS kind separator Ionization chamber to identify low energy ions |
| Explosive Burning Supernovae • R-process, origin of the heavier nuclei? abundances | Example: $^{132}\text{Sn}(n,\gamma)^{133}\text{Sn}$ | Direct measurement Collisions between a neutron beam and RIB | <ul style="list-style-type: none"> RIB intensity $> 10^{10}$ pps Neutron beam intensity $> 10^{10}$ pps Collimated and monochromatic neutron beam | |
| Explosive Burning Supernovae • R-process, origin of the heavier nuclei? abundances | $d(^{132}\text{Sn},p)^{133}\text{Sn}$ $d(^{130}\text{Cd},p)^{131}\text{Cd}$ or (d,t) reactions Cd and below, n-rich Sn | <ul style="list-style-type: none"> High resolution (d,p) and (d,t) transfer reactions can be used with secondary radioactive beams for determining the energies and spectroscopic factors of occupied and valence states at the shell closures. The (d,p) serves also for simulating (n,gamma) capture rates. Measure of masses Determine lifetimes of g.s. or isomeric states (which can be mainly populated at high T in | <ul style="list-style-type: none"> Radioactive nuclei in the regions close to $N = 50$ and $N = 82$ $E \sim 8$ A MeV Intensity $> 10^7$ pps Few per seconds. | |

| | | | | |
|---|---|---|--|--|
| | | <ul style="list-style-type: none"> supernovae). Beta-delayed neutron emission Pn, and search of unbound neutron states that can contribute to the inverse capture process. Extrapolations of the evolution of the N=82 shell closure and the location of the vg7/2 to lighter elements. This letter shell plays a decisive role for the beta-decays (vg7/2->πg9/2). | >10pps | <ul style="list-style-type: none"> Neutron counter for Pn values, Neutron spectroscopy to search for resonances |
| <p><u>Big Bang Nucleosynthesis</u></p> <p>The ⁷Li primordial abundance</p> | Not in the field of Nuclear Physics | | | |
| <p><u>Neutron stars</u></p> | <ul style="list-style-type: none"> - Collective Excitations - Pairing properties - Density dependence of the symmetry energy - Compressed nuclei. | <ul style="list-style-type: none"> Mass measurement Spin-dipole, soft-dipole modes, ISGQR to measure the neutron skin. GMR in neutron rich nuclei.(ex. ¹³²Sn(α,α')) Gamow-Teller / IAS in charge-exchange reactions. Charge radius measurements. Two neutron transfer. Fusion-evaporation and multi-fragmentation. | <ul style="list-style-type: none"> Neutron-rich nuclei Systematic study of isotopic chains For transfer reactions, energy beam > 10 MeV and < 20 MeV. Post accelerator up to approx. 200 MeV | |

Bibliography

- [1] *Perspectives of nuclear physics in europe*. <http://www.nupecc.org/pub/lrp10/> (2010). 2
- [2] F. de Oliveira, V. Tatischeff and et al. *Prospective irfu in2p3*. <http://journeesprospective.in2p3-irfu.fr/> (2012). 2
- [3] P. Ade, N. Aghanim, C. Armitage-Caplan, M. Arnaud, M. Ashdown, F. Atrio-Barandela, J. Aumont, C. Baccigalupi, A. J. Banday, R. Barreiro et al. *Planck 2013 results. xvi. cosmological parameters*. *Astronomy & Astrophysics* 571, A16 (2014). 2
- [4] A. Coc, P. Delbourgo-Salvador, F. De Oliveira, P. Aguer, S. Barhoumi, G. Bogaert, J. Kiener, A. Lefebvre and J. Thibaud. *The Astrophysical Journal* 402, 62 (1993). 2
- [5] M. Assié and F. de Oliveira Santos. *Russbach Nuclear Astrophysics school 2009* . 2
- [6] F. Hammache, A. Coc, N. De Sereville, I. Stefan, P. Roussel, S. Ancelin, M. Assié, L. Audouin, D. Beaumel, S. Franchoo et al. *Physical Review C* 88, 062802 (2013). 2
- [7] *P. Ujic*. Ph.D. Thesis, Université de Caen, 2011 . 3, 9, 22
- [8] P. Ujic and F. de Oliveira Santos. *Russbach Nuclear Astrophysics school 2011* . 3
- [9] H. Benhabiles-Mezhoud, J. Kiener, J.-P. Thibaud, V. Tatischeff, I. Deloncle, A. Coc, J. Duprat, C. Hamadache, A. Lefebvre-Schuhl, J.-C. Dalouzy et al. *Physical Review C* 83, 024603 (2011). 4
- [10] C. E. Rolfs and W. S. Rodney. *Cauldrons in the cosmos: Nuclear astrophysics* (University of Chicago press, 1988). 5, 6, 13
- [11] P. Descouvemont. *Theoretical models for nuclear astrophysics* (Nova Science Publishers, 2004). 6, 7
- [12] A. Sauerwein, H.-W. Becker, H. Dombrowski, M. Elvers, J. Endres, U. Giesen, J. Hasper, A. Hennig, L. Netterdon, T. Rauscher et al. *Physical Review C* 84, 045808 (2011). 6
- [13] M. Guttormsen, M. Aiche, F. B. Garrote, L. Bernstein, D. Bleuel, Y. Byun, Q. Ducasse, T. Eriksen, F. Giacoppo, A. Görngen et al. *Experimental level densities of atomic nuclei*. *The European Physical Journal A* 51, 1 (2015). 7
- [14] C. A. Bertulani. *Nuclei in the Cosmos* (World Scientific, 2014). 7, 13
- [15] W. Hauser and H. Feshbach. *The inelastic scattering of neutrons*. *Physical review* 87, 366 (1952). 8
- [16] G. Michaud and W. A. Fowler. *Thermonuclear-reaction rates at high temperature*. *Physical Review C* 2, 2041 (1970). 9
- [17] T. Rauscher, F.-K. Thielemann and K.-L. Kratz. *Phys. Rev. C* 56, 1613 (1997). 9

- [18] E. Huttel, W. Arnold, H. Baumgart and G. Clausnitzer. Nuclear Instruments and Methods in Physics Research Section B: Beam Interactions with Materials and Atoms 12, 193 (1985). 13
- [19] H. Assenbaum, K. Langanke and C. Rolfs. Zeitschrift für Physik A Atomic Nuclei 327, 461 (1987). 13, 14
- [20] K. Langanke, T. Shoppa, C. Barnes and C. Rolfs. Physics Letters B 369, 211 (1996). 14
- [21] C. Spitaleri, C. Bertulani, L. Fortunato and A. Vitturi. Physics Letters B 755, 275 (2016). 14, 23
- [22] F. Raiola, P. Migliardi, L. Gang, C. Bonomo, G. Gyürky, R. Bonetti, C. Broggin, N. Christensen, P. Corvisiero, J. Cruz et al. Physics Letters B 547, 193 (2002). 14, 22
- [23] F. Raiola, L. Gang, C. Bonomo, G. Gyürky, M. Aliotta, H. Becker, R. Bonetti, C. Broggin, P. Corvisiero, A. D'Onofrio et al. The European Physical Journal A-Hadrons and Nuclei 19, 283 (2004). 14
- [24] K. Kettner, H. Becker, F. Strieder and C. Rolfs. Journal of Physics G: Nuclear and Particle Physics 32, 489 (2006). 15, 16, 19, 23
- [25] M. E. Rose. Physical Review 49, 727 (1936). 15
- [26] N. Gove and M. Martin. *Log-f tables for beta decay*. Atomic Data and Nuclear Data Tables 10, 205 (1971). 15
- [27] B. Wang, S. Yan, B. Limata, F. Raiola, M. Aliotta, H. Becker, J. Cruz, N. De Cesare, A. D'Onofrio, Z. Fülöp et al. *Change of the 7be electron capture half-life in metallic environments*. The European Physical Journal A-Hadrons and Nuclei 28, 375 (2006). 15, 22
- [28] B. Limata, F. Raiola, B. Wang, S. Yan, H. Becker, A. D'Onofrio, L. Gialanella, V. Roca, C. Rolfs, M. Romano et al. The European Physical Journal A-Hadrons and Nuclei 28, 251 (2006). 15, 22
- [29] G. Stoppini. *Coulomb screening in superconducting pdh*. Il Nuovo Cimento D 13, 1181 (1991). 16
- [30] *Private communication* . 16
- [31] G. Audi, O. Bersillon, J. Blachot and A. Wapstra. *The nubase evaluation of nuclear and decay properties*. Nuclear Physics A 729, 3 (2003). 16, 21, 85, 87
- [32] S. Triambak, P. Finlay, C. Sumithrarachchi, G. Hackman, G. Ball, P. Garrett, C. Svensson, D. Cross, A. Garnsworthy, R. Kshetri et al. Physical review letters 109, 042301 (2012). 16, 17, 21
- [33] *Online data service, ensdf database*. <http://www.nndc.bnl.gov/ensdf/> . 16
- [34] *Nndc online service*. <http://www.nndc.bnl.gov/logft/> . 16
- [35] J. Simpson, F. Azaiez, G. De France, J. Fouan, J. Gerl, R. Julin, W. Korten, P. Nolan, B. Nyako, G. Sletten et al. *The exogam array: a radioactive beam gamma-ray spectrometer*. Acta Physica Hungarica, New Series, Heavy Ion Physics 11, 159 (2000). 17

- [36] H. Neumüller, M. Lehmann, G. Ischenko, S. Klaumünzer and H. Adrian. *Enhancement of the superconducting critical temperature t_c of niobium by radiation damage*. Physics Letters A 62, 446 (1977). 19
- [37] W. H. Press. *Numerical recipes 3rd edition: The art of scientific computing* (Cambridge university press, 2007). 20
- [38] P. Ujić, F. de Oliveira Santos, M. Lewitowicz, N. Achouri, M. Assié, B. Bastin, C. Borcea, R. Borcea, A. Buta, A. Coc et al. Physical review letters 110, 032501 (2013). 22
- [39] *Faster: Faster: Fast acquisition system for nuclear research*. <http://faster.in2p3.fr/index.php/about-faster> . 23
- [40] E. Lamour. Accreditation to supervise research, Université Pierre et Marie Curie (2012). 23
- [41] E. Anders and N. Grevesse. *Abundances of the elements: Meteoritic and solar*. Geochimica et Cosmochimica acta 53, 197 (1989). 25
- [42] C. Abia, A. Recio-Blanco, P. De Laverny, S. Cristallo, I. Dominguez and O. Straniero. The Astrophysical Journal 694, 971 (2009). 25
- [43] A. Jorissen, V. Smith and D. Lambert. Astronomy and Astrophysics 261, 164 (1992). 25
- [44] A. Renda, Y. Fenner, B. K. Gibson, A. I. Karakas, J. C. Lattanzio, S. Campbell, A. Chieffi, K. Cunha and V. V. Smith. *On the origin of fluorine in the milky way*. Monthly Notices of the Royal Astronomical Society 354, 575 (2004). 25
- [45] H. Jönsson, N. Ryde, G. Harper, M. Richter and K. Hinkle. *Fluorine in the solar neighborhood: Is it all produced in asymptotic giant branch stars?* The Astrophysical Journal Letters 789, L41 (2014). 25
- [46] G. R. Caughlan and W. A. Fowler. *Thermonuclear reaction rates v. Atomic Data and Nuclear Data Tables* 40, 283 (1988). 26, 27, 60, 61, 65, 67
- [47] F. de Oliveira Santos. Ph.D. thesis, Ph.D. thesis. Universite de Paris XI Orsay (1995). 29
- [48] M. Macfarlane and S. Pieper. Argonne National Laboratory, ANL-76-1 I, Internal report . 29
- [49] P. Kunz. U. Colorado, 30/jun/1982 version . 29
- [50] M. Mermaz. 1967, Universit6 de Paris, CEA-R3078 internal report, unpublished. . 29
- [51] P. Descouvemont . 31
- [52] F. de Oliveira Santos. Ph.D. Thesis, Université de Paris-Sud, 1995 . 32, 33
- [53] F. De Oliveira, A. Coc, P. Aguer, C. Angulo, G. Bogaert, J. Kiener, A. Lefebvre, V. Tatischeff, J.-P. Thibaud, S. Fortier et al. Nuclear Physics A 597, 231 (1996). 32, 33
- [54] J. MacDonald. The Astrophysical Journal 267, 732 (1983). 33

- [55] F. De Oliveira, A. Coc, P. Aguer, G. Bogaert, J. Kiener, A. Lefebvre, V. Tatischeff, J.-P. Thibaud, S. Fortier, J. Maison et al. *Physical Review C* 55, 3149 (1997). [33](#), [34](#), [61](#), [89](#), [96](#)
- [56] S. Wilmes, P. Mohr, U. Atzrott, V. Kölle, G. Staudt, A. Mayer and J. W. Hammer. *Phys. Rev. C* 52, R2823 (1995). [33](#)
- [57] S. Wilmes, V. Wilmes, G. Staudt, P. Mohr and J. Hammer. *Physical Review C* 66, 065802 (2002). [34](#)
- [58] H. Fortune and A. Lacaze. *Physical Review C* 67, 064305 (2003). [34](#)
- [59] C. Ugalde, B. DiGiovine, D. Henderson, R. Holt, K. Rehm, A. Sonnenschein, A. Robinson, R. Raut, G. Rusev and A. Tonchev. *Physics Letters B* 719, 74 (2013). [34](#)
- [60] The White Book of ELI Nuclear Physics, Bucharest Magurele, Romania. . [34](#)
- [61] A. Di Leva, G. Imbriani, C. Abia, S. Cristallo, N. De Cesare, I. Dominguez, A. D'Onofrio, L. Gialanella, M. Romano, M. Romoli et al. In *Nuclei in the Cosmos (NIC XII)* (2012), volume 1, p. 161. [34](#)
- [62] D. Bardayan. *Journal of Physics G: Nuclear and Particle Physics* 43, 043001 (2016). [35](#)
- [63] S. Giron and F. t. Hammache. *Journal of Physics G: Nuclear and Particle Physics* 43, 043001 (2016). [35](#)
- [64] J. José, M. Hernanz and C. Iliadis. *Nucl. Phys. A* 777, 550 (2006). [37](#)
- [65] J. Gomez-Gomar *et al.* *MNRAS* 296, 913 (1998). [37](#)
- [66] F.-L. Collaboration et al. *Science* 345, 554 (2014). [37](#)
- [67] M. Hernanz. *Bull. Astr. Soc. India* 40, 377 (2012). [39](#)
- [68] A. C. *et al.* *Astron. Astrophys.* 357, 561 (2000). [38](#)
- [69] R. Coszach *et al.* *Phys. Lett. B* 353, 184 (1995). [38](#)
- [70] S. Utku and J. R. *et al.* *Phys. Rev. C* 57, 2731 (1998). [38](#), [44](#)
- [71] J. S. Graulich *et al.* *Phys. Rev. C* 63, 011302 (2001). [38](#)
- [72] D. W. Bardayan *et al.* *Destruction of ^{18}f via $^{18}F(p, \alpha)^{15}o$ burning throught the $e_{c.m.} = 665kev$ resonance.* *Phys. Rev. C* 63, 065802 (2001). [38](#), [44](#), [46](#)
- [73] D. W. Bardayan *et al.* *Strength of the $^{18}f(p, \alpha)^{15}o$ resonance at $e_{CM} = 330kev$.* *Phys. Rev. Lett.* 89, 262501 (2002). [38](#)
- [74] D. Visser *et al.* *Phys. Rev. C* 69, 048801 (2004). [38](#)
- [75] N. de Séréville *et al.* *Nuclei in the Cosmos-IX*, June 25–30, CERN, Geneva. p. 005 (2006). [38](#)
- [76] Y. Xu and F. e. de Oliveira Santos. Article in preparation . [38](#), [40](#)

- [77] C. Nesaraja and N. S. *et al.* Phys. Rev. C 75, 5809 (2007). [38](#), [46](#)
- [78] M. Antony, A. Pape and J. Britz. Atomic Data and Nuclear Data Tables 66, 1 (1997). [41](#)
- [79] M. Dufour and P. Descouvemont. Nucl. Phys. A 785, 381 (2007). [41](#), [46](#), [47](#), [52](#)
- [80] S. Feynman, Leighton. *Le cours de physique de feynman - mécanique quantique* (1986). [41](#)
- [81] A.J.Ferguson (North-Holland, 1965). [42](#), [44](#), [45](#)
- [82] D. Overway *et al.* Nucl. Phys. A 366, 299 (1981). [42](#)
- [83] J. Hardy *et al.* Phys. Rev. 183, 854 (1969). [44](#)
- [84] D. Haynes, K. Kemper and N. Fletcher. Phys. Rev. C 5, 5 (1972). [44](#)
- [85] J. G. Pronko, R. G. Hirko and D. C. Slater. Phys. Rev. C 7, 1382 (1973). [45](#)
- [86] T. Otsubo and I. A. *et al.* Nucl. Phys. A 259, 452 (1976). [45](#)
- [87] M. J.-C. DALOUZY. Ph.D. thesis, Université de Caen/Basse Normandie (2009). [47](#)
- [88] J. Dalouzy, L. Achouri, M. Aliotta, C. Angulo, H. Benhabiles, C. Borcea, R. Borcea, P. Bourgault, A. Buta, A. Coc *et al.* Physical review letters 102, 162503 (2009). [47](#), [49](#)
- [89] A. S. J. Murphy, A. Laird, C. Angulo, L. Buchmann, T. Davinson, P. Descouvemont, S. Fox, J. José, R. Lewis, C. Ruiz *et al.* Physical Review C 79, 058801 (2009). [47](#), [49](#)
- [90] D. Mountford, A. S. J. Murphy, N. Achouri, C. Angulo, J. Brown, T. Davinson, F. de Oliveira Santos, N. De Séréville, P. Descouvemont, O. Kamalou *et al.* Physical Review C 85, 022801 (2012). [49](#)
- [91] F. Ph.D. thesis Boulay. Ph.D. thesis, Université de Caen/Basse Normandie (2015). [51](#), [52](#)
- [92] R. Azuma, E. Uberseder, E. Simpson, C. Brune, H. Costantini, R. De Boer, J. Görres, M. Heil, P. LeBlanc, C. Ugalde *et al.* Physical Review C 81, 045805 (2010). [52](#), [97](#)
- [93] A. L. Sallaska, C. Wrede, A. García, D. W. Storm, T. A. D. Brown, C. Ruiz, K. A. Snover, D. F. Ottewell, L. Buchmann, C. Vockenhuber, D. A. Hutcheon and J. A. Caggiano. Phys. Rev. Lett. 105, 152501 (2010). [55](#)
- [94] A. L. Sallaska, C. Wrede, A. García, D. W. Storm, T. A. D. Brown, C. Ruiz, K. A. Snover, D. F. Ottewell, L. Buchmann, C. Vockenhuber, D. A. Hutcheon, J. A. Caggiano and J. José. Phys. Rev. C 83, 034611 (2011). [55](#)
- [95] V. Tatischeff, M. Tavani, P. von Ballmoos, L. Hanlon, U. Oberlack, A. Aboudan, A. Argan, D. Bernard, A. Brogna, A. Bulgarelli *et al.* In *SPIE Astronomical Telescopes+ Instrumentation* (International Society for Optics and Photonics, 2016), pp. 99052L–99052L. [56](#)
- [96] J. Grindlay, H. Gursky, H. Schnopper, D. Parsignault, J. Heise, A. Brinkman and J. Schrijver. The Astrophysical Journal 205, L127 (1976). [57](#)

- [97] D. K. Galloway, M. P. Muno, J. M. Hartman, D. Psaltis and D. Chakrabarty. The Astrophysical Journal Supplement Series 179, 360 (2008). 57
- [98] S. Woosley, A. Heger, A. Cumming, R. Hoffman, J. Pruet, T. Rauscher, J. Fisker, H. Schatz, B. Brown and M. Wiescher. The Astrophysical Journal Supplement Series 151, 75 (2004). 57
- [99] J. L. Fisker, H. Schatz and F.-K. Thielemann. The Astrophysical Journal Supplement Series 174, 261 (2008). 58, 64, 68
- [100] M. Wiescher, G. Berg, M. Couder, J. Fisker, Y. Fujita, J. Görres, M. Harakeh, K. Hatanaka, A. Matic, W. Tan et al. Progress in Particle and Nuclear Physics 59, 51 (2007). 58
- [101] P. Magnus, M. Smith, A. Howard, P. Parker and A. E. Champagne. Nuclear Physics A 506, 332 (1990). 59, 60
- [102] T. Sakuda and F. Nemoto. Progress of Theoretical Physics 62, 1606 (1979). 60
- [103] K. Langanke, M. Wiescher, W. Fowler and J. Gorres. The Astrophysical Journal 301, 629 (1986). 59, 60
- [104] J. L. Fisker, J. Görres, M. Wiescher and B. Davids. The Astrophysical Journal 650, 332 (2006). 60
- [105] W. Tan, J. Fisker, J. Görres, M. Couder and M. Wiescher. Physical review letters 98, 242503 (2007). 60
- [106] H. T. Fortune, A. Lacaze and R. Sherr. Physical Review C 82, 034312 (2010). 61
- [107] K. Ikeda, N. Takigawa and H. Horiuchi. Progress of Theoretical Physics Supplement 68, 464 (1968). 64, 100, 104
- [108] J. Okołowicz, M. Płoszajczak and W. Nazarewicz. Progress of Theoretical Physics Supplement 196, 230 (2012). 65, 100
- [109] H. Bethe and C. Critchfield. Phys. Rev. 54, 248 (1938). 65, 67
- [110] C. Angulo, M. Arnould, M. Rayet, P. Descouvemont, D. Baye, C. Leclercq-Willain, A. Coc, S. Barhoumi, P. Aguer, C. Rolfs et al. Nuclear Physics A 656, 3 (1999). 65
- [111] K. Brown, M. Butler and D. Guenther. arXiv preprint nucl-th/0207008 (2002). 65
- [112] M. A. Bernstein, W. Friedman and W. Lynch. Physical Review C 29, 132 (1984). 66
- [113] J. Görres, M. Wiescher and F.-K. Thielemann. Physical Review C 51, 392 (1995). 68, 74, 75, 83
- [114] K. Nomoto, F.-K. Thielemann and S. Miyaji. Astronomy and Astrophysics 149, 239 (1985). 68
- [115] R. Charity. The European Physical Journal Plus 131, 1 (2016). 69
- [116] W. Mittig and P. Roussel-Chomaz. *Results and techniques of measurements with inverse kinematics*. Nuclear Physics A 693, 495 (2001). 70

- [117] C. Angulo, G. Tabacaru, M. Couder, M. Gaelens, P. Leleux, A. Ninane, F. Vanderbist, T. Davinson, P. J. Woods, J. Schweitzer et al. *Physical Review C* 67, 014308 (2003). 71, 72
- [118] E. Warburton and B. Brown. *Physical Review C* 46, 923 (1992). 72
- [119] D. R. Tilley *et al.* *Energy levels of light nuclei a=18-19*. *Nucl. Phys. A* 595, 1 (1995). 72
- [120] C. Rolfs and W. Rodney. *Cauldrons in the Cosmos* (The University of Chicago Press, 1988). 76, 87
- [121] F. de Oliveira Santos, P. Himpe, M. Lewitowicz, I. Stefan, N. Smirnova, N. Achouri, J. Angélique, C. Angulo, L. Axelsson, D. Baiborodin et al. *The European Physical Journal A-Hadrons and Nuclei* 24, 237 (2005). 77
- [122] Y. Jaganathen, N. Michel and M. Płoszajczak. *Physical Review C* 89, 034624 (2014). 77
- [123] L. Grigorenko and M. V. Zhukov. *Physical Review C* 72, 015803 (2005). 78
- [124] L. Grigorenko. *Physics of Particles and Nuclei* 40, 674 (2009). 78
- [125] I. Mukha, K. Sümmerer, L. Acosta, M. Alvarez, E. Casarejos, A. Chatillon, D. Cortina-Gil, J. Espino, A. Fomichev, J. Garcia-Ramos et al. *Physical review letters* 99, 182501 (2007). 78
- [126] I. Mukha, L. Grigorenko, K. Sümmerer, L. Acosta, M. Alvarez, E. Casarejos, A. Chatillon, D. Cortina-Gil, J. Espino, A. Fomichev et al. *Physical Review C* 77, 061303 (2008). 78
- [127] L. Grigorenko, I. Mukha and M. Zhukov. *Nuclear Physics A* 713, 372 (2003). 78, 81, 82
- [128] B. A. Brown, A. Etchegoyen and W. D. M. Rae. *MSU-NSCL Report* 524 (1986). 78
- [129] A. P. Zuker. *Physical Review Letters* 23, 983 (1969). 78
- [130] <http://www.nndc.bnl.gov/chart/>. 78, 79
- [131] H. T. Fortune and R. Sherr. *Physical Review C* 76, 014313 (2007). 79
- [132] H. Fortune and R. Sherr. *Physical Review C* 83, 057301 (2011). 79
- [133] T. Zerguerras, B. Blank, Y. Blumenfeld, T. Suomijärvi, D. Beaumel, B. Brown, M. Chartier, M. Fallot, J. Giovinazzo, C. Jouanne et al. *The European Physical Journal A-Hadrons and Nuclei* 20, 389 (2004). 79
- [134] V. Goldberg, V. Dukhanov, A. Pakhomov, G. Rogatchev, I. Serikov, V. Timofeev and M. Brenner. *Phys. At. Nucl* 60, 1186 (1997). 79
- [135] A. N. Ostrowski and S. C. et. *Nucl. Instr. and Meth. A* 480, 448 (2002). 79
- [136] C. Stodel et al. *Proceeding World Scientific EXON, Peterhof, Russia* 60, 180 (2004). 79, 97
- [137] E. Berthoumieux, B. Berthier, C. Moreau, J. Gallien and A. Raoux. *Nuclear Instruments and Methods in Physics Research Section B: Beam Interactions with Materials and Atoms* 136, 55 (1998). 81, 85

- [138] L. Grigorenko and M. V. Zhukov. *Physical Review C* 76, 014009 (2007). 82
- [139] M. Assie, F. de Oliveira Santos, T. Davinson, F. De Grancey, L. Achouri, J. Alcántara-Núñez, T. Al Kalanee, J.-C. Angélique, C. Borcea, R. Borcea et al. *Physics Letters B* 712, 198 (2012). 83
- [140] R. Wallace and S. Woosley. *The Astrophysical Journal Supplement Series* 45, 389 (1981). 83
- [141] M. Wiescher, H. Schatz and A. E. Champagne. *PHILOSOPHICAL TRANSACTIONS-ROYAL SOCIETY OF LONDON SERIES A MATHEMATICAL PHYSICAL AND ENGINEERING SCIENCES* pp. 2105–2136 (1998). 83
- [142] H. Schatz, A. Aprahamian, V. Barnard, L. Bildsten, A. Cumming, M. Ouellette, T. Rauscher, F.-K. Thielemann and M. Wiescher. *Physical Review Letters* 86, 3471 (2001). 83
- [143] N. Michel, W. Nazarewicz, M. Płoszajczak and T. Vertse. *Journal of Physics G: Nuclear and Particle Physics* 36, 013101 (2008). 83
- [144] N. Michel, W. Nazarewicz and M. Płoszajczak. *Nuclear Physics A* 794, 29 (2007). 83
- [145] J. Dobaczewski, N. Michel and W. Nazarewicz. *Prog. Part. Nucl. Phys* 59, 432 (2007). 83
- [146] C. Forssén, G. Hagen, M. Hjorth-Jensen, W. Nazarewicz and J. Rotureau. *Physica Scripta* 2013, 014022 (2013). 83
- [147] H. Herndl, J. Görres, M. Wiescher, B. Brown and L. Van Wormer. *Physical Review C* 52, 1078 (1995). 84
- [148] J. B. Ehrman. *Physical Review* 81, 412 (1951). 84
- [149] R. Thomas. *Physical Review* 88, 1109 (1952). 84
- [150] K. Ogawa, H. Nakada, S. Hino and R. Motegi. *Physics Letters B* 464, 157 (1999). 84, 94
- [151] P. Bertrand, F. Daudin, M. Di Giacomo, B. Ducoudret and M. Duval. In *17th International Conference on Cyclotrons and their Applications* (2004), pp. 1–3. 84
- [152] R. Anne, D. Bazin, A. Mueller, J. Jacmart and M. Langevin. *Nuclear Instruments and Methods in Physics Research Section A: Accelerators, Spectrometers, Detectors and Associated Equipment* 257, 215 (1987). 84
- [153] F. Guo, J. Powell, D. Lee, D. Leitner, M. McMahan, D. Moltz, J. O’Neil, K. Perajarvi, L. Phair, C. Ramsey et al. *Physical Review C* 72, 034312 (2005). 85, 91
- [154] V. Goldberg, G. Chubarian, G. Tabacaru, L. Trache, R. Tribble, A. Aprahamian, G. Rogachev, B. Skorodumov and X. Tang. *Physical Review C* 69, 031302 (2004). 85
- [155] D. Lee, K. Peräjärvi, J. Powell, J. O’Neil, D. Moltz, V. Goldberg and J. Cerny. *Physical Review C* 76, 024314 (2007). 85

- [156] H. Fujita, G. Berg, Y. Fujita, J. Rapaport, T. Adachi, N. Botha, H. Fujimura, K. Fujita, K. Hara, K. Hatanaka et al. *Physical Review C* 79, 024314 (2009). 85
- [157] B. Guo, Z. Li, Y. Li, J. Su, D. Pang, S. Yan, Z. Wu, E. Li, X. Bai, X. Du et al. *Physical Review C* 89, 012801 (2014). 85, 91
- [158] D. W. Bardayan, P. O'Malley, J. C. Blackmon, K. Chae, K. Chipps, J. Cizewski, R. Hatarik, K. Jones, R. Kozub, C. Matei et al. *Physical Review C* 78, 052801 (2008). 85
- [159] F. Ajzenberg-Selove. *Nuclear Physics A* 413, 1 (1984). 86
- [160] A. Messiah (1958). 88
- [161] D. Tilley, H. Weller and C. Cheves. *Nuclear Physics A* 564, 1 (1993). 88, 91
- [162] J. Goss, P. Jolivet, C. Browne, S. Darden, H. Weller and R. Blue. *Physical Review C* 12, 1730 (1975). 91
- [163] A. Lepailleur, O. Sorlin, L. Caceres, B. Bastin, C. Borcea, R. Borcea, B. Brown, L. Gaudefroy, S. Grévy, G. Grinyer et al. *Physical review letters* 110, 082502 (2013). 91
- [164] K. L. Heyde. In *The Nuclear Shell Model* (Springer, 1994), pp. 58–154. 92
- [165] M. Pfützner, M. Karny, L. Grigorenko and K. Riisager. *Reviews of Modern Physics* 84, 567 (2012). 94
- [166] A. I. Baz', Y. B. Zel'dovich and A. M. Perelomov . 95
- [167] C. Rothe, S. Hintschich and A. Monkman. *Physical review letters* 96, 163601 (2006). 95
- [168] I. Stefan (Ph.D. Thesis Université de Caen, 2006). 95
- [169] I. Stefan, F. de Oliveira Santos, O. Sorlin, T. Davinson, M. Lewitowicz, G. Dumitru, J. Angélique, M. Angélique, E. Berthoumieux, C. Borcea et al. *Physical Review C* 90, 014307 (2014). 95
- [170] V. Datar, S. Kumar, D. Chakrabarty, V. Nanal, E. Mirgule, A. Mitra and H. Oza. *Physical review letters* 94, 122502 (2005). 95
- [171] V. Datar, D. Chakrabarty, S. Kumar, V. Nanal, S. Pastore, R. Wiringa, S. Behera, A. Chatterjee, D. Jenkins, C. Lister et al. *Physical review letters* 111, 062502 (2013). 95
- [172] H. T. Fortune. *Physical Review C* 83, 024311 (2011). 96, 97
- [173] S. Truong and H. Fortune. *Physical Review C* 28, 977 (1983). 96, 99
- [174] F. Cappuzzello, C. Rea, A. Bonaccorso, M. Bondi, D. Carbone, M. Cavallaro, A. Cunsolo, A. Foti, S. Orrigo, M. R. D. Rodrigues et al. *Physics Letters B* 711, 347 (2012). 96, 99
- [175] L. Canton, G. Pisent, J. Svenne, K. Amos and S. Karataglidis. *Physical review letters* 96, 072502 (2006). 96, 97
- [176] H. T. Fortune and R. Sherr. *Physical review letters* 99, 089201 (2007). 96, 97

- [177] L. Canton, G. Pisent, J. Svenne, K. Amos and S. Karataglidis. *Physical Review Letters* 99, 089202 (2007). 96
- [178] A. Le, J. Oliveira, D. Galante, G. Amadio, R. Lichtentha, H. Bohlen, A. Ostrowski, A. Blazevic, C. Borcea, V. Guimara et al. *Nuclear Physics A* 734, 331 (2004). 96
- [179] I. Mukha, N. Timofeyuk, K. Sümmerer, L. Acosta, M. Alvarez, E. Casarejos, A. Chatillon, D. Cortina-Gil, J. Espino, A. Fomichev et al. *Physical Review C* 79, 061301 (2009). 96
- [180] L. Grigorenko, R. Johnson, I. Mukha, I. Thompson and M. Zhukov. *Physical review letters* 85, 22 (2000). 99
- [181] L. Grigorenko, T. Golubkova and M. Zhukov. *Physical Review C* 91, 024325 (2015). 99
- [182] F. de Grancey. Ph.D. thesis, Ph.D. thesis Université de Caen/Basse Normandie (2009). 99
- [183] F. De Grancey, A. Mercenne, F. de Oliveira Santos, T. Davinson, O. Sorlin, J. Angélique, M. Assié, E. Berthoumieux, R. Borcea, A. Buta et al. *Physics Letters B* 758, 26 (2016). 99
- [184] D. Millener, J. Olness, E. Warburton and S. Hanna. *Physical Review C* 28, 497 (1983). 100
- [185] C. Broggini, D. Bemmerer, A. Guglielmetti and R. Menegazzo. *Annual Review of Nuclear and Particle Science* p. 60 (2010). 102
- [186] N. Achouri, F. de Oliveira Santos, M. Lewitowicz, B. Blank, J. Äystö, G. Canchel, S. Czajkowski, P. Dendooven, A. Emsallem, J. Giovinazzo et al. *The European Physical Journal A-Hadrons and Nuclei* 27, 287 (2006). 104
- [187] Lynda Achouri (Ph. D Thesis. Université de Caen, 2001). 104
- [188] A. Pichard, J. Mrazek, M. Assié, M. Hass, M. Honusek, G. Lhersonneau, F. de Oliveira Santos, M.-G. Saint-Laurent and E. Šimečková. *The European Physical Journal A* 47, 1 (2011). 104
- [189] D. Bardayan, K. Chipps, S. Ahn, J. Blackmon, U. Greife, K. Jones, A. Kontos, R. Kozub, L. Linhardt, B. Manning et al. *Physics Procedia* 66, 451 (2015). 104
- [190] H. Fortune and R. Sherr. *Physical Review C* 72, 024319 (2005).
- [191] D. Baye, P. Descouvemont and F. Leo. *Physical Review C* 72, 024309 (2005).
- [192] A. Mukhamedzhanov, B. Irgaziev, V. Goldberg, Y. V. Orlov and I. Qazi. *Physical Review C* 81, 054314 (2010).
- [193] H. T. Fortune. *Physical Review C* 74, 054310 (2006).
- [194] A. Lepine-Szily, J. Oliveira, D. Galante, G. Amadio, V. Vanin, R. Lichtenthäler, V. Guimaraes, G. Lima, H. Bohlen, A. Ostrowski et al. *Nuclear Physics A* 722, C512 (2003).
- [195] W. Peters, T. Baumann, D. Bazin, B. Brown, R. Clement, N. Frank, P. Heckman, B. Luther, F. Nunes, J. Seitz et al. *Physical Review C* 68, 034607 (2003).

- [196] W. Benenson, E. Kashy, A. Ledebuhr, R. Pardo, R. Robertson and L. Robinson. *Physical Review C* 17, 1939 (1978).
- [197] G. KeKelis, M. Zisman, D. Scott, R. Jahn, D. Vieira, J. Cerny and F. Ajzenberg-Selove. *Physical Review C* 17, 1929 (1978).
- [198] F. Ajzenberg-Selove. *Nucl. Phys. A* 523, 1 (1991).
- [199] C. A. *et al.* *Nucl. Phys. A* 656, 3 (1999).
- [200] M. S. Anthony and A. P. *et al.* *At. Dat. and Nucl. Dat. Tables* 66, 1 (1997).
- [201] S. Goriely, M. Arnould and K. Takahashi. *Phys. Rep.* 450, 97 (2007).
- [202] M. Arnould and F. B. *et al.* *Nucl. Inst. Meth. B* 40/41, 498 (1989).
- [203] M. Asplund, N. Grevesse and A. Sauval. *Nucl. Phys. A* 777, 1 (2006).
- [204] G. Azuelos and J. Kitching. *Phys. Rev. C* 12, 563 (1975).
- [205] D. W. Bardayan and J. B. *et al.* *Search for astrophysically important ^{19}Ne levels with a thick-target $^{18}\text{F}(p,p)^{18}\text{F}$ measurement.* *Phys. Rev. C* 70, 015804 (2004).
- [206] D. W. Bardayan, R. Kozub and M. Smith. *^{19}F α widths and the $^{18}\text{F}+p$ reaction rates.* *Phys. Rev. C* 71, 18801 (2005).
- [207] L. B. *et al.* *Nucl. Instrum. Methods Phys. Res. A* 276, 509 (1989).
- [208] H. Bingham and H. F. *et al.* *Phys. Rev. L* 26, 1448 (1971).
- [209] H. Bingham and H. F. *et al.* *Phys. Rev. C* 7, 60 (1973).
- [210] W. F. G. Burbidge, M. Burbidge and F. Hoyle. *Synthesis of elements in stars.* *Rev. Mod. Phys.* 29, 547 (1957).
- [211] A. E. Champagne and M. Wiescher. *Annu. Rev. Nucl. Part. Sci.* 42, 39 (1992).
- [212] J. Carlson and D. R. *et al.* *Phys. Rev. C* 44, 619 (1991).
- [213] E. Church and J. Kraushaar. *The geometrical correction in angular correlation measurements.* *Phys. Rev.* 88, 419 (1952).
- [214] A. Coc and E. V.-F. *et al.* *Updated big bang nucleosynthesis compared with wmap observations and the abundance of light elements.* *Ap.J.* 600, 544 (2004).
- [215] A. Coc and N. J. N. *et al.* *Coupled variations of fundamental couplings and primordial nucleosynthesis.* *Phys. Rev. D* 76, 023511 (2007).
- [216] T. Davinson *et al.* *Nucl. Instr. and Meth. A* 454, 350 (2000).
- [217] B. Fields and S. Sarkar. *Rev. Part. Phys.* (2006).

- [218] S. Frankel. Phys. Rev. 83, 673 (1951).
- [219] J. Garrett, R. Middleton and H. Fortune. Phys. Rev. C 2, 1243 (1970).
- [220] M. Gelin. Ph.D. thesis, Universite de Caen (2007).
- [221] P. M. t. A. Gobbi. Phys. Rev. Lett. 26, 396 (1971).
- [222] D. Goosman and K. J. *et al.* Phys. Rev. C 4, 1800 (1971).
- [223] S. Goriely. Ph.D. thesis, Universite libre de Bruxelles (1989).
- [224] J. S. Graulich and S. C. *et al.* Nucl. Phys. A 688, 138 (2001).
- [225] M. Greene and E. Nelson. Phys. Rev. 4, 1068 (1967).
- [226] M. H. *et al.* Astrophys. J. 526, 97 (1999).
- [227] J. Kiener. Phys. Rev. C 58, 2174 (1998).
- [228] J. Kuehner. Phys. Rev. 125, 1650 (1962).
- [229] A. Lane and R. Thomas. *R-matrix theory of nuclear reactions*. Rev. Mod. Phys. 30, 257 (1958).
- [230] E. Leblanc and N. C. *et al.* *High-energy resolution alpha spectrometry using cryogenic detectors*. Appl. Rad. and Iso. 64, 1281 (2006).
- [231] L. Martz and S. *et al.* Phys. Rev. C 20, 1340 (1979).
- [232] C. Moss and C. D. *et al.* Phys. Rev. C 5, 1122 (1972).
- [233] F. de Oliveira Santos and P. H. *et al.* The Eur. Phys. Jour. A 24, 237 (2005).
- [234] A. D. Panagiotou and H. E. Gove. Nucl. Phys. A 196, 145 (1972).
- [235] R. W. W. A. A. Penzias. Ap. J. 142, 419 (1965).
- [236] J. G. Pronko and R. A. Lindgren. Nucl. Instr. and Meth. 98, 445 (1972).
- [237] M. P. t. K.E. Rehm. Phys. Rev. C 53, 1950 (1996).
- [238] M. Rose. *The analysis of angular correlation and angular distribution data*. Phys. Rev. 91, 610 (1953).
- [239] N. de Sereville and A. C. *et al.* Phys. Rev. C 67, 052801 (2003).
- [240] N. de Sereville and A. C. *et al.* Nucl. Phys. A 718, 259 (2003).
- [241] N. de Séréville *et al.* Nucl. Phys. A 758, 745 (2005).
- [242] N. Shu and D. W. B. *et al.* Chin. Phys. Lett. 20, 1470 (2003).
- [243] G. Steigman. *Primordial nucleosynthesis : Sucess and challenges*. Mod. Phys. E 15, 1 (2006).

- [244] R. B. Firestone. *Table of Isotopes* (Virginia S. Shirley, 1996).
- [245] D. F. Torgerson and K. W. *et al.* β^+ Decay of ^{20}Na . *Phys. Rev. C* 8, 161 (1973).
- [246] G. Vancraeynest and P. D. *et al.* *Phys. Rev. C* 57, 2711 (1998).
- [247] <http://ipnweb.in2p3.fr/tandem-alto/tandem/machine/source/source.html>.
- [248] http://www-dapnia.cea.fr/Phocea/Vie_des_labos/Ast/ast_technique.php?id_ast=446.
- [249] <http://www.nndc.bnl.gov/chart/getdataset.jsp?nucleus=19F&unc=nds>.
- [250] <http://groups.nscl.msu.edu/lise>.
- [251] <http://www.talys.eu/home/>.
- [252] D. Wilkinson and D. A. *et al.* *Nucl. Phys. A* 166, 661 (1971).
- [253] W.-M. Yao and C. A. *et al.* *Review of particle physics*. *Journal of Physics G* 33, 1+ (2006).
- [254] (2009).
- [255] L. Axelsson, M. J. G. Borge, S. Fayans, V. Z. Goldberg, S. Grévy, D. Guillemaud-Mueller, B. Jonson, K. M. Källman, T. Lönnroth, M. Lewitowicz, P. Manngård, K. Markenroth, I. Martel, A. C. Mueller, I. Mukha, T. Nilsson, G. Nyman, N. A. Orr, K. Riisager, G. V. Rogatchev, M. G. Saint-Laurent, I. N. Serikov, O. Sorlin, O. Tengblad, F. Wenander, J. S. Winfield and R. Wolski. *Phys. Rev. C* 54, R1511 (1996).
- [256] A. Lane. *Reduced widths of individual nuclear energy levels*. *Reviews of Modern Physics* 32, 519 (1960).
- [257] R. RIEDIGER, P. PETITJEAN and J. MUCKET. *Evolution of the Lyman-alpha forest from high to low redshift*. *Astronomy and astrophysics* 329, 30 (1998).
- [258] A. Coc, E. Vangioni-Flam, P. Descouvemont, A. Adahchour and C. Angulo. *Updated big bang nucleosynthesis compared with wilkinson microwave anisotropy probe observations and the abundance of light elements*. *The Astrophysical Journal* 600, 544 (2004).
- [259] F. Spite and M. Spite. *A&A* 115, 357 (1982).
- [260] J. Bardeen, L. N. Cooper and J. R. Schrieffer. *Theory of superconductivity*. *Phys. Rev.* 108, 1175 (1957).
- [261] J. Chadwick. *Possible existence of a neutron*. *Nature* 129, 312 (1932).

